Dipartimento di Fisica
Università degli Studi di Genova

Advanced Fluorescence Correlation Spectroscopy for The Study of Nuclear Dynamics

Thesis submitted in partial fulfillment of the requirements for the title of Doctor of Philosophy

Melody Di Bona

XXXI ciclo

Scuola di Dottorato in Fisica

Università degli Studi di Genova

Tutor: Alberto Diaspro

Supervisor: Luca Lanzanò

Contents

Abstract

Chromatin is a macromolecule mainly composed by DNA and histones. Chromatin not only has the function of compacting the DNA in order to make it fit into the nucleus, but also plays an active role in the regulation of all biological processes using DNA as template in eukaryotes, such as transcription, DNA replication and DNA repair. The architectural organization of chromatin can play an important role in gene expression by regulating the diffusion of molecules via binding interactions and molecular crowding. In this respect, understanding how variations of chromatin architecture affect nuclear dynamics is of fundamental importance.

Among the techniques that are able to probe the nuclear interior, fluorescence microscopy is sensitive, specific and does not require strong manipulation of the sample, allowing also measurements to be performed in living samples. But not all the fluorescence microscopy techniques have the adequate temporal resolution to follow the dynamics of the nuclear environment. Fluorescence Correlation Spectroscopy (FCS) is able to probe chromatin accessibility and molecular crowding in live cells by measuring fast diffusion of molecules in the range between microseconds and milliseconds. In particular, single point FCS (spFCS) has a high temporal resolution but lacks spatial information. Conversely, spatially-resolved methods, like scanning FCS, have in general limited temporal resolution.

The aim of this thesis is to overcome these limitations through the Intensity Sorted FCS technique. This technique is able to probe fast molecular diffusion in nuclear environment distinguishing between different regions of the space at a high temporal resolution. This achievement is due to the idea of dividing a whole FCS measurement, performed through a slow scan of the beams, into short temporal segment: each segment is analyzed and for each one an ACF is calculated. Then the ACFs are sorted into two populations basing on the intensity of a reference trace, that specifically distinguish the two nuclear regions probed: for each set of ACFs corresponding to a region, the average ACF is calculated. In this way it is possible to retrieve statistically robust information about diffusion in two distinct nuclear regions in the same measurement.

The method was successfully implemented on a custom setup, and applied in studying diffusion of untagged monomeric GFP in regions of different chromatin compaction, namely euchromatin and heterochromatin/perinucleolar heterochromatin, in normal cells or following treatments knowing to affect chromatin compaction, showing its ability to highlight differences in diffusion of a small inert probe despite the high intercellular variability. The technique was also used to study the diffusion of proteins known to interact with chromatin, like for instance, transcription factors.

Intensity Sorted FCS was also extended to commercial setups, and was implemented on a commercial Laser Scanning Microscope, in a line scan FCS configuration: the basic concept of dividing the measurement into segments and sorting them basing on a reference intensity is maintained, while the temporal resolution was lower. This technique was applied in the study of the Estrogen Receptor mobility under different hormonal treatments, in a project in collaboration with the Baylor College of Medicine in Houston.

Finally, Intensity Sorted FCS was coupled with super-resolution. Among the super-resolution techniques, STimulated Emission Deplession is applicable to laser scanning microscopes: to overcome the limitations it presents in its coupling with FCS, the additional lifetime information is exploited. The novel SPLIT technique, being able to tune the excitation volume in a post-processing way in the same measurement, and to intrinsically eliminate the fluorescence background coming from the out-of-focus planes, was used in addition to FLCS in order to perform three-dimensional diffusion studies in living cells, at sub-diffraction spatial scales. The coupling of the STED-FLCS technique to the Intensity Sorted FCS method allows to perform super-resolved dynamic measurements in different nuclear compartments, obtaining different diffusion laws associated to each nuclear compartment in a single measurement.

The introduction of this method, and the possibility to couple it with super-resolution, opens new ways into the exploration of the nuclear environment, at interesting spatial scales (chromatin fibers being of a size ranging from tens to a hundred nanometers), and could thus provide important lacking information about nuclear environment that can help better understand the important crosstalk between structure and function in the nucleus.

1. Introduction to FCS

In this chapter, the basics of fluorescence are introduced and, after a summary about fluorescence microscopy, in particular fluorescence dynamics techniques, the concept of Fluorescence Correlation Spectroscopy is explained, together with related techniques based on the analysis of fluctuations.

1.1 Fluorescence

Fluorescence is a process involving light emission by a molecule brought to an excited electronic state. The electronic states of a molecule can be represented by the Jablonski diagram (1) (Fig. 1.1.1): when an electron is excited by light absorption, it jumps on a higher electronic level at the singlet state. After a fast internal conversion, that involves vibrionic relaxation and brings the electron to the first excited singlet state (S_1), the electron can return to the singlet ground state either by emitting a photon (**fluorescence**, **spontaneous emission** with a rate k_f) or non-radiatevely (rate k_n). There are several examples of non-radiative processes: for instance, with very low probability, the electron can be transferred to a triplet state (**intersystem crossing**), from which it decays in a slower way (quantum-mechanically forbidden transition), emitting a photon (**phosphorescence** k_p). Another way in which the energy can be dissipated is the internal collision between particles, namely **quenching**, the rate of which strongly depends on the concentration of the particles (k_q). In general, k_n is the total rate which includes all the possible non-radiative processes (2).

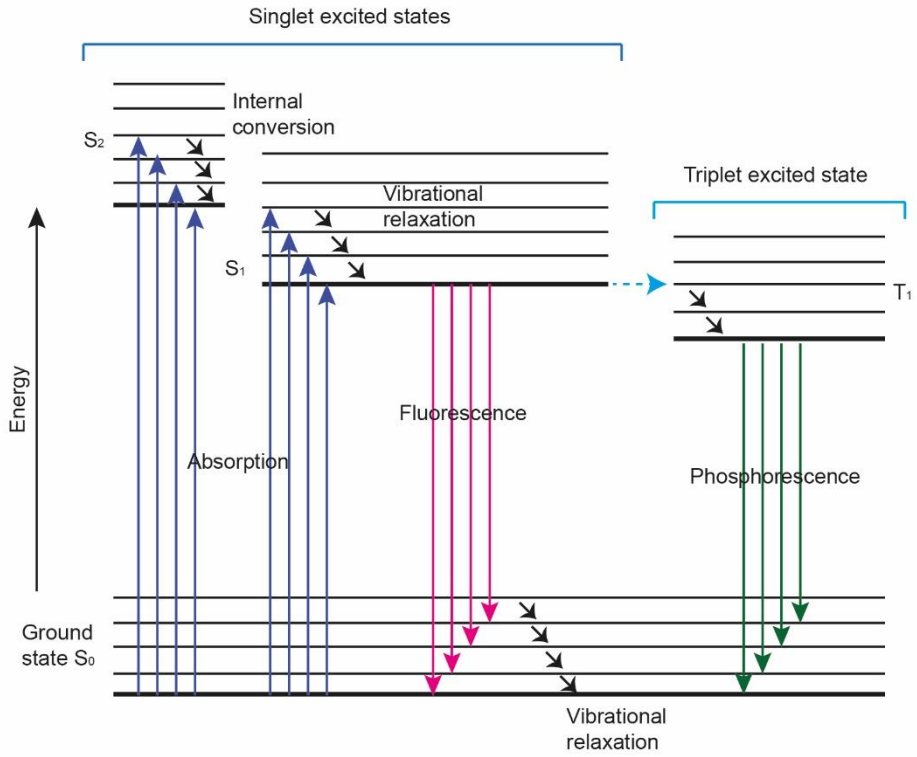

Fig. 1.1.1 Jablonski diagram. The Jablonski diagram illustrates the electronic states of a molecule and the transitions between them. The states are arranged vertically by energy and grouped horizontally by spin multiplicity. The vibrational ground states of each electronic state are indicated with thick lines, the higher vibrational states with thinner lines. Radiative transitions involve the absorption, if the transition occurs to a higher energy level, or the emission, in the reverse case, of a photon and are indicated by straight arrows. Non-radiative transitions arise through several different mechanisms: vibrational relaxation (the relaxation of the excited state to its lowest vibrational level), internal conversion (when a vibrational state of an electronically excited state can couple to a vibrational state of a lower electronic state), or intersystem crossing (a transition to a state with a different spin multiplicity), which can give rise to phosphorescence.

The fraction of the excited electrons that decay emitting fluorescence is called **quantum yield** (3), and is given by:

$$\varphi = \frac{k_f}{k_f + k_n} \qquad \textbf{Eq. 1}$$

The quantum yield, often described as the number of emitted photons relative to the number of absorbed photons, represents the efficiency of the fluorescence process. The quantum yield is always less than 1, because of the losses in energy due to internal conversion: this process is much faster (about 10^{-12}s) than fluorescence (about 10^{-8}s), so a fraction of energy is dissipated by the system in order to reach thermal equilibrium. This phenomenon is called **Stokes shift**, and accounts also for the higher wavelength of the emitted photon in respect to the absorbed one.

Another important fluorescence property is the **fluorescence lifetime** (4)(τ), that is the average time the molecule stays in its excited state before emitting a photon. If a population of fluorophores is excited at time t=0, the lifetime is the time it takes for the number of excited molecules to decay to 1/e of the original population, according to the formula:

$$\frac{n(t)}{n(0)} = e^{-\frac{t}{\tau}} \quad . \qquad \textbf{Eq. 2}$$

Generally, the fluorescence lifetime has values in the order of nanoseconds, and it is typical of each fluorophore, greatly influenced by the environment and insensitive to the concentration of the fluorophores. Thanks to these important features, it is possible, using Fluorescence Lifetime Imaging Microscopy (5), to retrieve information about the environment of a fluorophore, to distinguish between two fluorophores emitting in the same spectral range, and to monitor, for example, intracellular changes in viscosity or pH.

Every molecule that, once excited, returns to the ground state emitting a photon without intersystem crossing, is a **fluorophore**. Fluorescence is in general typical of aromatic molecules (an exception is given by the group of lanthanides, in which the fluorescence occurs from excitation of the electrons in the f orbitals, shielded from the solvent by more populated orbitals around them): a well characterized fluorophore is **quinine**, that lead also to the development of the first spectrofluorometer at NIH in the ‘50s.

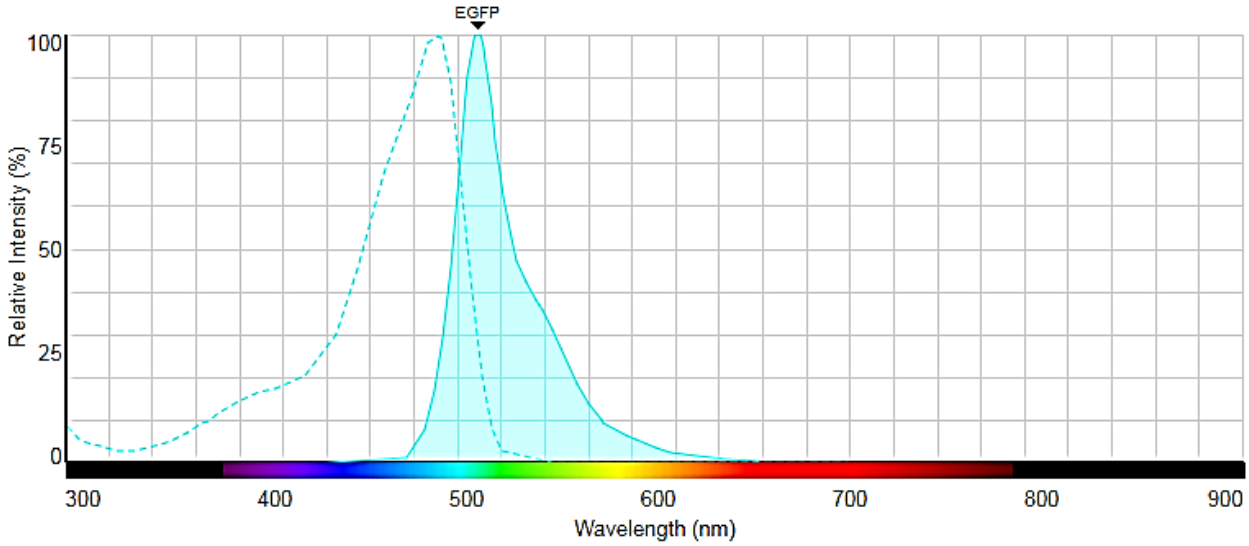

Fig. 1.1.2 Absorption and emission spectra of EGFP. A typical fluorescence spectrum of the green fluorescence protein. It is possible to see the peaks in absorption at about 490nm, and in excitation at about 510nm. The spectra was generated using the ThermoFisher Scientific online tool SpectraViewer.

Fluorescence emission is generally presented as **emission spectra**, which are the plot of the fluorescence intensity versus the wavelength. The fluorescence emission peaks are the probability a fluorophore, if excited, would emit a photon at that wavelength. The difference between the most probable emission wavelength and the most probable absorption wavelength is known as **Stokes shift**. The peaks, which represents the discrete vibrionic levels of the molecule, broaden and merge in a continuous spectrum for fluorophores used for biological application, due to the fact that both the use and the characterization of these fluorophores usually occur at room temperature (Fig. 1.1.2). An important feature of emission is that it is independent of the excitation wavelength (2).

1.2 Fluorescence microscopy

The phenomenon of fluorescence has been greatly exploited in optical microscopy. Optical microscopy (or light microscopy) is a branch of microscopy which uses visible light and optical components (lenses and mirrors) to convey and magnify images of small samples.

The visible spectrum is the portion of the electromagnetic spectrum visible to the human eye with wavelengths from about 390 to 700 nm, but also infrared or ultra-violet lights are often used in optical microscopy techniques.

Optical components may range from the afore-mentioned lenses and mirrors, to optical filters, polarizing elements, coatings, prisms. In addition to that, sources of light consisting in halogen lamps, LEDs or lasers and optomechanical elements, like piezo scanning stages and galvanometric mirrors, are usually necessary (2).

Historically, light microscopy is the oldest form of microscopy: the optical microscope was probably invented at the beginning of the 17th century. In 1595 Zacharias Jansen (1580–1638) created an instrument based on two lenses (with the second lens further magnifying the image produced by the first) able of magnifications up to 9 times (Fig. 1.2.1 a). In 1623, Galileo Galilei published the development of a "telescope" customized to see the objects very near, later refined in order to have three bi-convex lenses, being able to magnify about 30 times (Fig. 1.2.1 b). Subsequently, Robert Hooke (1635–1703) further improved the microscope, adding features as a stage to hold the specimen, an illuminator, and coarse and fine focus controls. The most significant improvements in light microscopy were achieved in the nineteenth century, when business partners Carl Zeiss (1816–1888) and Ernst Abbe (1840–1905) added the substage condenser and developed superior lenses (thanks to the Abbe sine condition) that greatly reduced chromatic and spherical aberration, while permitting vastly improved resolution and higher magnification.

Fig. 1.2.1 The first microscopes. Reconstructions of Jansen's (a) and Galilei's (b) microscopes.

The simplest among all the optical microscopy illumination techniques is represented by bright-field microscopy. The sample is illuminated by a transmitted white light and contrast between the observed structures is caused by differences in light absorbance. The main drawback of this technique is the low contrast with most biological samples, resulting slightly more useful only for samples which have an intrinsic color. In addition to that, all the structures of the sample are observed super-imposed at the same time, without specificity, and different structures characterized by similar absorbance values will result the same in the final image (6).

Several methods have been developed in order to improve the contrast, for example dark field microscopy, where the unscattered light is not collected by the objective, or the phase contrast microscopy (7) (for which Frits Zernike was awarded with the 1953 Nobel Prize in Physics), which exploits the phase-shift of the light when crossing a specimen. Another useful technique is the histochemical staining of the specimen, using substances that recognize specific biological structures and absorb a defined wavelength of light, first introduced by Camillo Golgi and Ramon y Cajal (Fig. 1.2.2), awarded with the 1906 Nobel Prize for Physiology or Medicine.

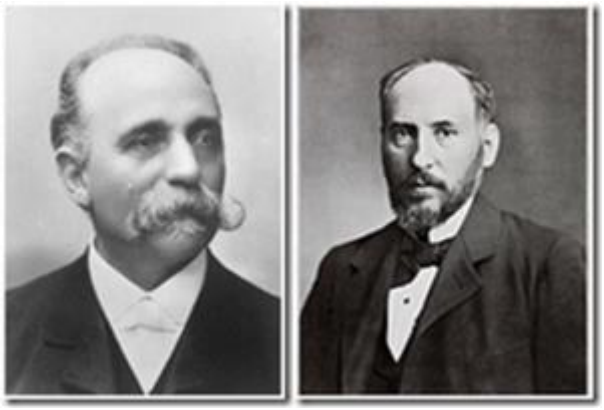

Fig. 1.2.2 Golgi and Cajal. Camillo Golgi (on the left) and Ramon y Cajal (on the right) were both awarded with the Nobel Prize in 1906 for their staining techniques, which allowed the observation of fine structures in the brain.

However, today the most popular contrasting technique is fluorescence, which requires the use of fluorophores as structure-specific markers in order to visualize only the structure of interest against a dark background. There are many fluorescent molecules that bind a biological molecule of interest, like the DNA-binding dyes, as ethidium bromide, which intercalates between the DNA bases; alternatively, it is possible to perform an immunofluorescence staining that exploits the highly specific binding of a labelled antibody to its antigen. In addition, there are several fluorescent proteins that can be genetically fused to a protein of interest, thus allowing the direct visualization of a target molecule inside living cells (8).

The exploitation of the process of fluorescence in optical microscopy thus allows for high-specificity and high-contrast of the images. Nonetheless, the use of fluorophores has some drawbacks that other light contrast techniques do not have, like **photobleaching** and **phototoxicity**. In addition, other effects can degrade the image quality, as for example the out-of-focus fluorescence: since the fluorophores are present in the whole cell volume, but only one

plane is in focus at a given time, the fluorescence derived from the other planes adds up, creating a blurred background that lowers the contrast of the resulting image (2).

To overcome this limitation, confocal microscopy was developed (9), providing the microscope with an optical section capability. In fact, the name confocal derives from the insertion in the detection optical path of a pinhole at a given distance (10), that rejects the fluorescence coming from the out-of-focus planes (Fig. 1.2.3). In this way, only the fluorescence emitted from the fluorophores in the plane in focus will be detected. Anyway, this improvement in axial resolution comes at the cost of a drop in signal intensity: the detector must be a very sensitive one, generally a photomultiplier tube (PMT) or an avalanche photodiode (APD), which transform the photons detected into an electrical signal processed by a computer.

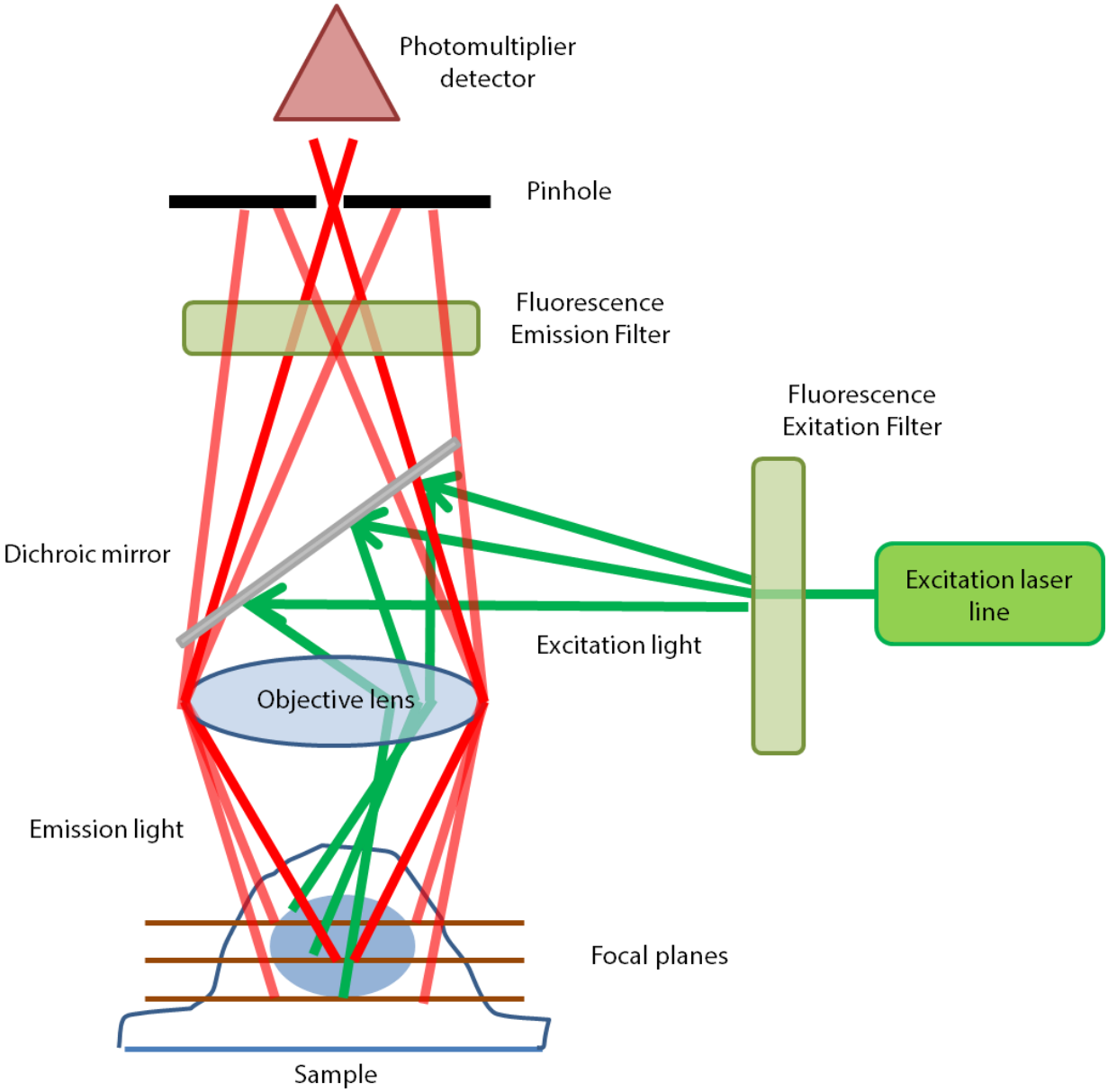

Fig. 1.2.3 Confocal optical setup. The schematic shows a typical confocal optical setup: Green light coming from the laser goes to a dichroic mirror which reflects it through the objective lens to the sample. The fluorescence light (red) goes back following the same path but this time passes through the dichroic and goes to the detector while passing through the pinhole. Note the light coming from the in-focus plane (deep red) goes right through the pinhole, while the light coming from out-of-focus planes (light red) is blocked.

The excitation light source is usually a monochromatic laser beam focused into a point of the sample. This is scanned across the sample point by point generally through galvo mirrors. The minimum extension of the excitation spot can be calculated, and is restricted by the diffraction of light, through the so-called Abbe's diffraction limit (11) :

$$d = \frac{\lambda}{2NA} = \frac{\lambda}{2 \cdot n \sin \vartheta} \qquad \textbf{Eq. 3}$$

Hence, the minimum distance at which two structures must be located for being resolved (i.e. visualized like two separate entities) d, is proportional to the excitation wavelength λ, and the numerical aperture NA, equal to the refractive index of the immersion medium n, times the sine of the semiangle of aperture ϑ, namely half of the angle at which the light coming from the sample is collected by the objective.

The distribution of the light into the spot is usually parametrized as a 3D Gaussian function, with x-y full width at half maximum (FWHM) corresponding to the Abbe's limit, while along the z axis it is usually set as ~3 times the lateral resolution. The diffraction limited spot is referred to as the Point Spread Function (PSF), characteristic of each microscope objective with a defined wavelength of excitation: the image is thus the convolution of the fluorophore real spatial distribution with the PSF (Fig. 1.2.4).

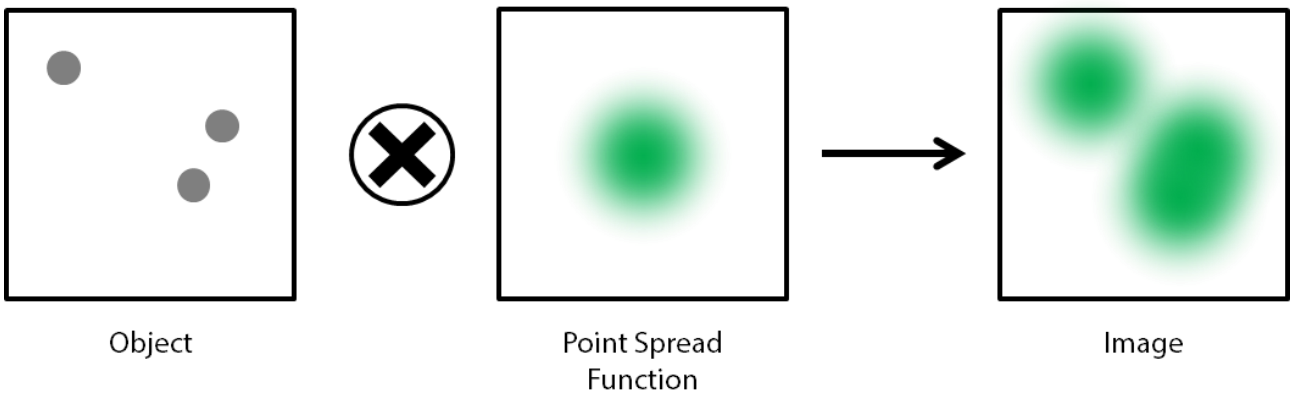

Fig. 1.2.4 Convolution. The schematic shows how the image obtained by a microscope is the convolution of the real fluorophore distribution with the PSF typical of that microscope.

A microscopy image is structurally very useful, but it gives information about a single moment in time. Time lapse fluorescence microscopy, which is the sequential acquisition of stack of images, allows studying cellular dynamics, but is generally limited to relatively slow processes. It is of great importance to study also the dynamics of cellular processes at a molecular level. In this case, the study of the molecular diffusion inside the cell, requires a high temporal resolution (in the order of the milliseconds, generally). In this view, several microscopy techniques have been developed that allow dynamic measurements with an adequate temporal resolution.

1.3 Fluorescence dynamics techniques

The implementation of fluorescence microscopy opened the way to the development of different techniques that can probe the dynamics of molecules in solution or inside a cell. These dynamic methods can be divided into three classes (Fig. 1.3.1): the **perturbation methods**, which rely on local photo-induced bleaching (or photo-activation) of fluorescence and the recording of the spatial distribution of the fluorescence signal over time; the **correlation methods**, which are based on the study of the spontaneous fluorescence fluctuations derived from the passage of fluorescent probes through a small detection volume; the **Single Particle Tracking methods**, which follow the motion of single fluorescent molecules directly over time.

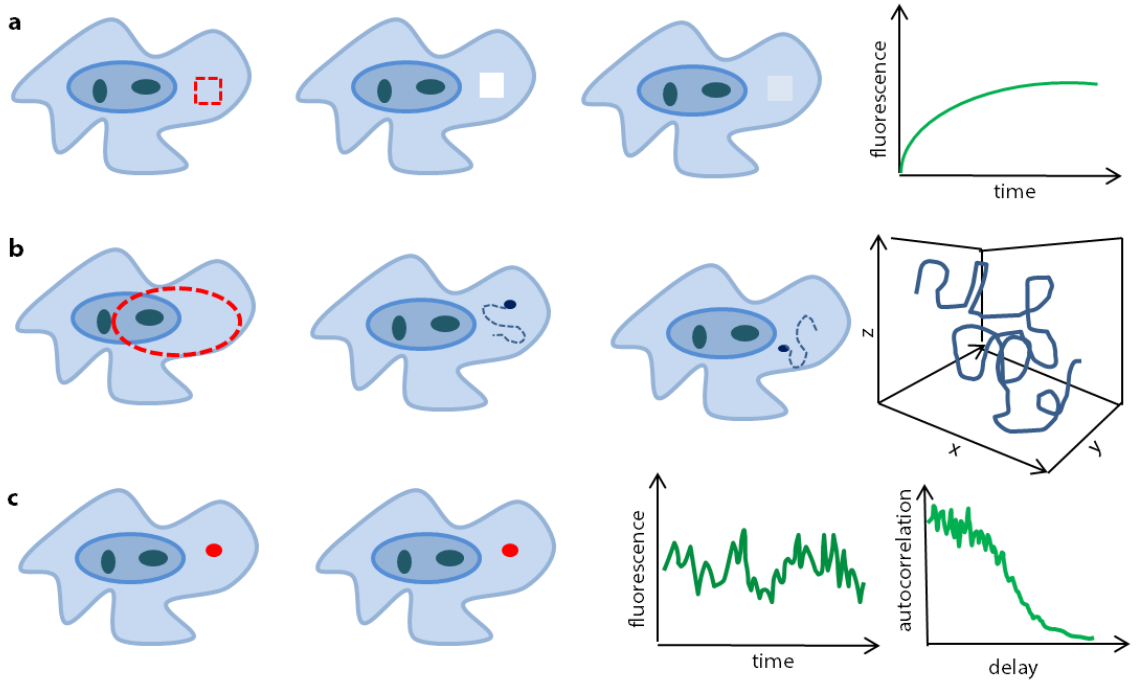

Fig. 1.3.1 Fluorescence dynamic methods. Schematic representation of the three categories of the fluorescence dynamic methods. In perturbation methods, an area is bleached and the variation in the fluorescence is recorded over time (a). In Single Particle Tracking methods, an area of the cell is imaged (dashed circle), and in this area, a single fluorescent molecule is followed in its path, giving a three-dimensional trajectory as output (b). In correlation methods, the fluorescence fluctuations are recorded in a point, and their autocorrelation function gives as an output, the auto correlation curve (c).

Among the perturbation methods, **Fluorescence Recovery After Photobleaching**, or FRAP, **Fluorescence Loss in Photobleaching**, or FLIP, and **Continuous Photobleaching**, or CP, are the most used (Fig. 1.3.2).

In FRAP, a small region of interest of the cell is bleached with high laser power, and the fluorescence recovery is measured: the redistribution of fluorescent molecules inside the bleached region up to an equilibrium state is directly proportional to the velocity of the probes. Traditionally, FRAP measurements are done in an imaging modality, which is limited by the acquisition speed of the microscope used, usually at least a few tens of milliseconds per image. This limitation can be overcame by point FRAP, which uses the small observation volume of a confocal microscope to record pre- and post-bleach intensities of fluorescence, allowing a temporal resolution below the millisecond range (12).

In a typical FLIP experiment, two regions have to be defined: a region of interest (ROI) where the fluorescence will be recorded during the experiment, and a bleaching area, usually near the ROI. This area will be bleached several times during the measurement, and the fluorescence intensity decrease in the ROI is recorded over time. The loss in fluorescence is due to the mobile fraction of the protein labelled: incomplete loss of fluorescence means that there are proteins that are bound and do not move to the bleached region. This technique is used, for instance, for the study of the exchange rates between organelles (13).

On the other hand, in CP, the decrease of the fluorescence intensity in a defined region of interest is recorded as a function of time under continuous illumination, until an equilibrium is reached. The output of the experiment is a decay signal of the fluorescence that usually shows a biphasic behavior: a fast initial decay due to the bleaching of an immobilized or slowly moving probe, and a slower asymptotic decay deriving from the bleaching of the fast mobile fraction of the probe, reaching an equilibrium with the freely moving probe coming from outside the investigated volume (14).

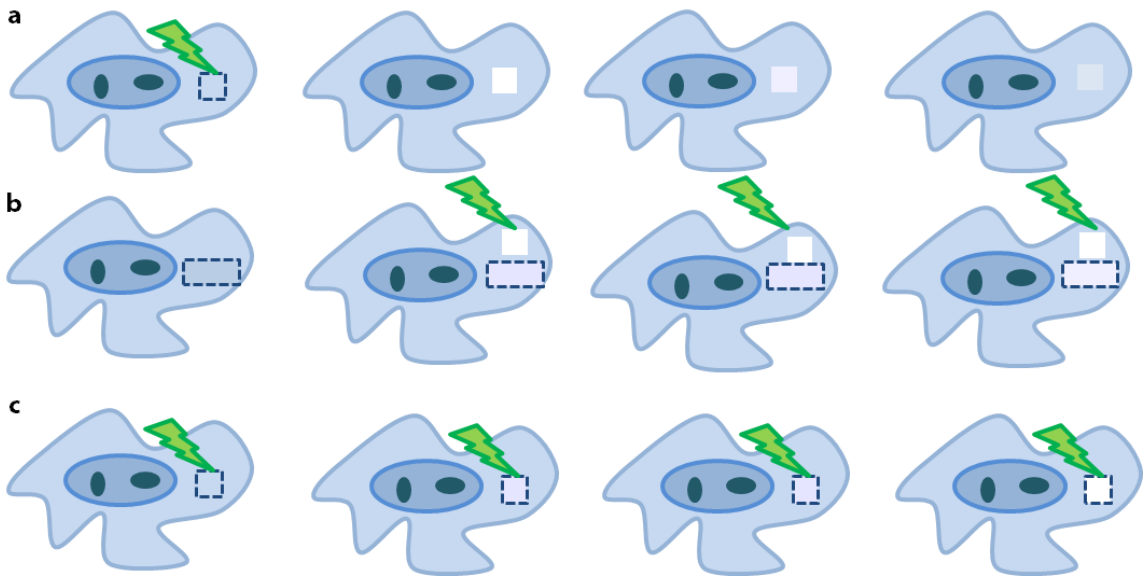

Fig. 1.3.2 Perturbation methods. Schematic representation of the perturbation methods. In FRAP, a ROI is bleached and the recovery of fluorescence intensity is recorded over time (a). In FLIP technique, an area is bleached over time, while the fluorescence intensity decay is recorded in a near ROI (b). In CP, the fluorescence intensity diminution is recorded in a ROI continuously illuminated (c).

All the techniques mentioned above are based on photobleaching, which requires high laser intensities on the cell. To prevent the photodamage of the living sample, others techniques can be used instead.

For instance, SPT techniques (15) are useful tools to investigate protein dynamics with nanometer spatial resolution and sub-second temporal precision. A series of images at a given time interval are acquired, and then processed in order to find the entities of interest (generally, proteins genetically labeled with fluorescent proteins). The center of the light spot produced by the fluorescent molecule can be localized with up to 10nm precision, yielding the coordinates of each fluorescent molecule in each image frame: this information is used to reconstruct the particle trajectory and, for example, to calculate the Mean Square Displacement (MSD) of the particle. The MSD can also be used to characterize the protein motion, for example to highlight anomalous diffusion. Since SPT is based on the acquisition of a series of image, the temporal resolution of this technique is generally limited to the image acquisition speed of the camera. It generally works very well for studying motion in 2D whilst its application to study 3D motion is more challenging. Elegant methods have been proposed to overcome this limitation, for instance a faster technique based on the scanning of the excitation spot around the particle, named orbital tracking (16–18).

Anyway, even if the principal drawbacks of SPT techniques have been successfully overcome in the last years, this methodology is still applicable only if few particles are labelled in the field of view and is not suitable to study the 3D diffusion of fluorescent molecules at a higher concentration.

1.4 Fluorescence Correlation Spectroscopy

Fluorescence Correlation Spectroscopy (FCS) is a technique widely used in the study of cellular protein dynamics, since it uses low laser intensities, and it does not suffer from the constrain of having only a few particles labelled in the sample, although possessing the sensitivity of a single particle method.

At the time of its introduction in 1972 by Magde, Elson and Webb (19), FCS was a technique very hard to implement, suffering from poor signal quality and large ensemble number. The introduction of the confocal microscope paved the way for FCS to become a routinely used technique (20, 21). In fact, a confocal optical setup has the great advantage of confining the detection volume to the sub-femtoliter range, reducing thus the amount of fluorescent particles analyzed at the same time. In addition, the introduction of very sensitive detectors enhances the quality of the signal recorded.

Basically, the fluctuations in the fluorescent intensity $F(t)$ arising from the passage of the fluorescent probes through the illuminated volume are recorded by usually an Avalanche Photodiode Detector (APD). These raw data are then processed to calculate the fluorescence intensity $F(t)$. On this, the auto-correlation curve is computed, using the following Auto Correlation Function (ACF) formula:

$$G(\tau) = \frac{\langle \delta F(t) \cdot \delta F(t+\tau) \rangle}{\langle F(t) \rangle^2} = \frac{\langle F(t) \cdot F(t+\tau) \rangle}{\langle F(t) \rangle^2} - 1 \qquad \textbf{Eq. 4}$$

where $F(t)$ is the intensity fluorescence at time t, $\langle F(t) \rangle = \left(\frac{1}{T}\right) \int_0^T F(t) dt$ is the time average of the signal, $\delta F(t) = F(t) - \langle F(t) \rangle$ are the fluctuations around the mean value $\langle F(t) \rangle$, and τ is the **correlation time** (Fig. 1.4.1). The resulting autocorrelation curve is a measure of the self-similarity of the signal, so its width is linked to the average residence time of the molecules inside the observation volume.

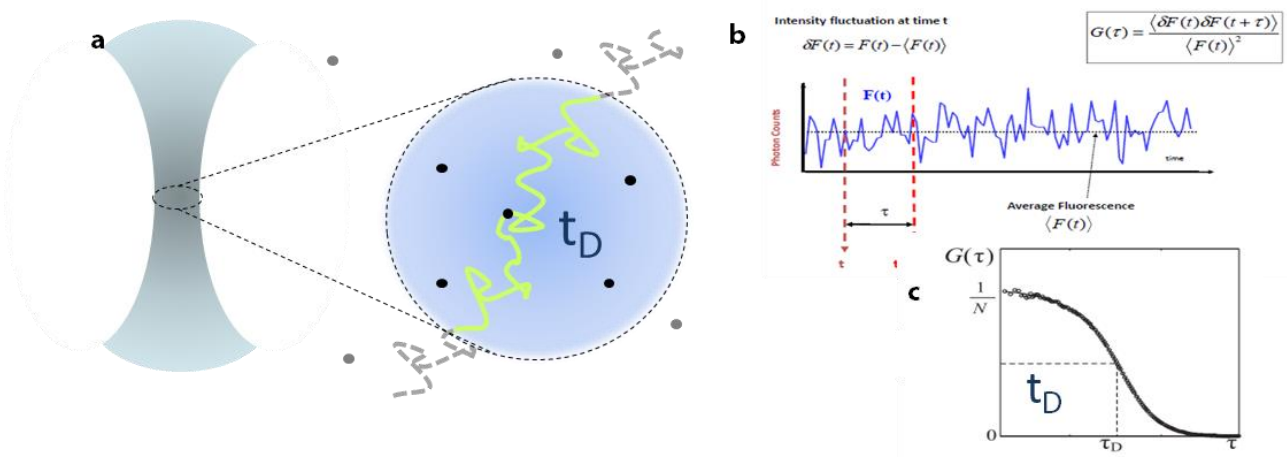

Fig. 1.4.1 Fluorescence Correlation Spectroscopy. In FCS, the laser light creates an observation volume, inside which the fluorescent particles move entering and exiting the illumination spot. The fluorescence fluctuation arising from the passage of the fluorescent probes through the observation volume are recorded (b), and analyzed by an autocorrelation function to obtain an autocorrelation curve (c), whose amplitude and width are related to the average number of particles presented in the illumination spot and the diffusion coefficient of the fluorescent molecules, respectively.

By fitting the curve with a theoretical model that best describes the motion of the particles in exam and the shape of the detection volume, it is possible to retrieve many useful information. For instance, in the case of **Brownian diffusion** and a Gaussian shape of the PSF:

$$G(t) = \frac{\gamma}{N}\left(1+\frac{t}{t_D}\right)^{-1}\left(1+\frac{t}{K^2 t_D}\right)^{-\frac{1}{2}} + G_\infty , \qquad \textbf{Eq. 5}$$

where $K = \frac{z_0}{w_0}$ is the ratio between the axial and the longitudinal extension of the PSF, N is the average number of molecules, γ is a shape factor related to the distribution of light in the detection volume (e.g. $\gamma = 0.3535$ for a Gaussian PSF), and G_∞ is the limiting factor for $t \to \infty$, usually equal to 0. Since $G(0) = \frac{\gamma}{N}$ if $G_\infty = 0$, the height of the ACF is inversely proportional to the number of molecules present in the detection volume. In addition, the characteristic correlation time t_D can be linked to the **diffusion coefficient** D by:

$$t_D = \frac{w_0^2}{4D} . \qquad \textbf{Eq. 6}$$

It is thus clear that from an FCS measurement it is possible to retrieve crucial information about the motion of the particles in the detection volume, from the time dependence of $G(t)$, and about their concentration and brightness, from the thermodynamic property $G(0)$ (22).

However, the interpretation of the correlation curve it is not always clear. For instance, the good theoretical model must be applied in order to avoid errors in the estimation of the diffusion coefficient. This can be clear to a trained eye from the shape of the curve, but sometimes it is hard, even for an expert, to determine which fit will give the best results. In addition, as it appears clearly in the equation (**Eq. 5**), the measurement strongly depends on the shape and size of the illumination spot. It is thus necessary a **volume calibration**. Anyway, the size of the volume not only depends on the setup, but is influenced by different factors that is often hard to identify and quantify. For instance, optical aberrations due to the coverslip varying thickness, the refractive index mismatch or astigmatism can easily led to even 50% error in diffusion coefficient estimation (23). Another important issue is the uncorrelated background light, which leads to an overestimation of the concentration due to a decrease in the curve amplitude. Also photobleaching can affect both the amplitude and the shape of the correlation curve, and depletion of fluorophores and consequently decaying intensities over time lead to deformed curves, as well as the presence in the observation volume of particularly bright aggregates. In addition, FCS has a high temporal resolution, but fundamentally lacks of spatial information. In order to overcome this limitation, several strategies have been developed during the years, creating a wide range of fluorescence correlation spectroscopy-based techniques.

1.5 FCS-based techniques

In the section above, basics of confocal single-point FCS were introduced. In respect to the SPT techniques, a classical FCS experiment does not allow to have information about the type of motion the particle is experiencing. In order to address this question, a new FCS-based technique, namely **spot-variation FCS** (24), has been described. In this kind of measurement, the detection volume size is varied, for example enlarging or reducing the pinhole size of a classical confocal microscope. The resulting different diffusion coefficient calculated for each volume are then plotted as the diffusion time against the squared observation volume size (**diffusion law**): the linear fit of these data provides information, through its intercept, about the motion of the molecule (for example, the diffusion is Brownian if the intercept is in the zero point of the graph). Another method through which is possible to retrieve a diffusion law is by moving the observation volume in the z-axis (**z-scan FCS**) (25). This method is based on the characteristic shape of a

two-photon excitation observation volume: this illumination scheme (26) offers various advantages, such as the reduction of the out-of-focus fluorescence, allowing a more precise shaping of the observation volume, and the reduction of photobleaching and then of phototoxicity. In addition, this illumination allows measurements to be performed also in turbid media (27).

Anyway, all these techniques still lack of spatial information, and have their disadvantages to study slow protein motion or interactions that occur at distances greater than the excitation beam waist. The introduction of the spatial dimension leads to several advantages, such as the parallelization of detection, which in turn decreases the acquisition time, and the elimination of the need of volume calibration. The simplest technique that introduces the space in the measurement is **dual-focus FCS** (28), in which two confocal spots are positioned at a defined distance, typically of hundreds of nanometers. In this way, not only the two auto-correlation curves can be retrieved, but also the cross-correlation between the two foci, which describes the probability that a molecule, present in the first detection volume at time t, is in the second detection volume at time $t+\tau$. This technique is very accurate in measuring diffusion times, and can also be applied to quantify the molecular flow.

On the other hand, in **Image Correlation Spectroscopy** (ICS), entire images are acquired, and for example in the Temporal ICS (**TICS**) each pixel acts as a single detection volume, allowing massively parallelization of the measurements. ICS is usually implemented on laser scanning microscopes, but the temporal resolution is limited by the mechanical scanning of the beams, so this technique can be used only for the study of very slow dynamics (29). An advantage can be gained if the illumination is in wide-field mode, like in **Total Internal Refraction-FCS** (TIR-FCS) (30), or using a **light-sheet illumination** microscope (31), where the limitation is given by the acquisition speed of the camera, instead of the speed of the scanning system.

The introduction of ICS and the use of images allows not only the analysis of temporal fluctuations, but also of the spatial ones, using spatial correlations in the image (32). It is possible to gain further temporal resolution if the time delay between image parts is included into the analysis, as it happen in **Raster Image Correlation Spectroscopy** (RICS) (33), which can study both very fast and slow dynamics. It is worth to note that, if some heterogeneity is present into the image, it can be hidden by the averaging process. However, it is also possible to analyze sub-regions of the image, and then obtain the correlation of the fluctuation locally, using this information to construct, for example, diffusion or flow maps (34). Finally, a good compromise between temporal resolution and parallelization can be obtain by **scanning FCS**, tipically used

for the study of intermediate diffusion, such as in membranes, in both the **line scanning** (35) and **circular scanning** (36, 37) configurations.

In conclusion, FCS-based techniques are a powerful tool for the study of dynamic, especially in the interior of a living cell, and can be efficiently implemented on different optical setups, allowing the study of different temporal ranges in different points in space, giving also interesting information about the fluorescent particles concentration, and brightness (that can also be used to study chemical reactions, or molecular complexes formation).

2. Nuclear organization and mobility studied by FCS

In this second chapter, the organization of the eukaryotic cell nucleus will be introduced, as an interesting biological application. Then, a brief summary about the importance of the nuclear dynamics and the techniques recently used for studying it, will be given, along with the issues that this type of measurements could encounter.

2.1 Chromatin organization in the eukaryotic cell nucleus

The nucleus is a cellular organelle typical of eukaryotic, probably derived from a symbiotic event occurred between an Archea and a bacterial cell (38). It accomplishes many fundamental functions in the cell physiology, among them it also has a structural and organizational role (39). The most important role for the nucleus is the storage of genetic information: inside it in fact the genomic DNA, which contains the largest part of the cell genes, is strictly packed by specific proteins named histones. The association of 147 bp of DNA with an histone octamer with a pair of each of the core histones H2A, H2B, H3 and H4, is called a nucleosome (a disc-shaped complex of around 11nm in diameter), the fundamental unit of chromatin together with the linker histone H1 (40). This macromolecular complex has not only the fundamental function of storing and preserving the genome information during each cell cycle, but also plays important roles in the survival of the cell since it regulates the DNA replication, and in this way, the production of the right proteins for each particular type of cell. In fact, it has been shown that chromatin structure has a role in the regulation of gene expression (41). Consequently, chromatin plays crucial roles in lineage commitment, senescence, differentiation and tumorigenesis (42–44). Recent studies show that chromatin, not only affects some cellular processes itself, but also creates a nanoenvironment that greatly influences the biochemical and biophysical reactions occurring in the nucleus (45, 46). Interestingly, it seems that chromatin, and then the subnuclear compartments, are self-organizing (47), and that physical processes, like phase separation (48), are the driving force of subnuclear compartments formation, like the more compacted **heterochromatin** (called in this way in opposition to the less dense chromatin, called **euchromatin**), but also of several nuclear processes (49, 50).

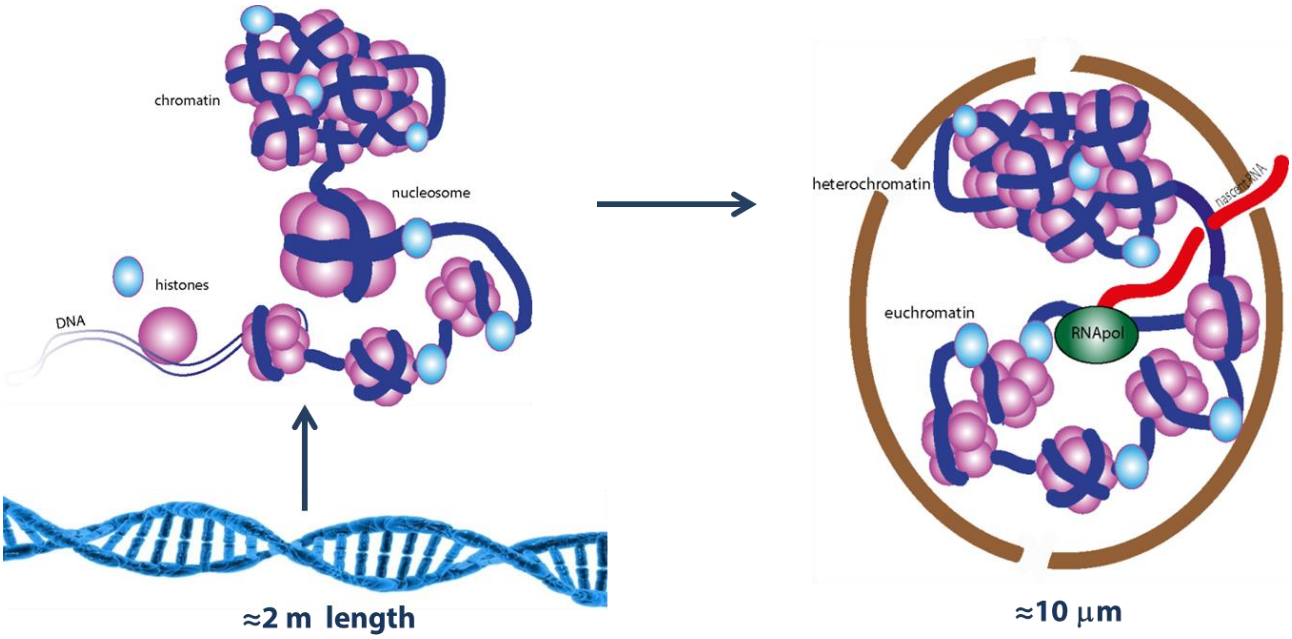

Fig. 2.1.1 Chromatin organization in the nucleus. Schematic representation of chromatin formation and its organization into the eukaryotic cell nucleus. The DNA is highly compacted and packed by histone proteins in order to form the nucleosomes, which are in turn less or more compacted in order to form the euchromatin and the heterochromatin compartment, respectively. As it is shown in the figure, transcription can occur only in the euchromatin compartment, where the nucleosomes leave a free DNA space to the polymerase to attach and process the DNA.

Anyway, it is worthy to note that the genome organization and structure are highly dynamic themselves, as the whole nuclear environment (51). It has been reported that nucleosomes move at a velocity of 1.2 nm/ms, and the same temporal scale is shown by chromatin fibers movement, while the overall chromatin reorganization occur in large regions (1-5 μm) in several seconds. In addition, processes like DNA transcription and replication require the coordination in time and space of multiple macromolecular complexes so that they can timely assemble over an accessible DNA responsive element. Moreover, early experiments clearly established that transcription factors and other nuclear proteins interactions were more dynamic than expected, showing relatively rapid diffusion, ranging from 0.1 to 10 $\mu m^2/s$ (52, 53). Thus, it remains fundamentally important to determine how proteins move within different regions of the nucleus that are comprised of markedly-heterogeneous chromatin density, and maintain their ability to reach and bind to their target sequences.

2.2 FCS in the nucleus

Since the great importance that dynamics have in nuclear organization and functionality, it is fundamental the study of the nuclear environment from both a structural and a dynamic point of view. This can be accomplished by using fluorescence microscopy methods, that are suitable to be used in live cells, are more specific than other methods, like electron microscopy, and have a single cell sensitivity, differently from molecular biology or biochemical methods. Anyway, as stressed before, not all the microscopy techniques possess the high temporal resolution needed for studying fast dynamics: for this reason, more and more studies have relied on dynamic microscopy techniques in order to study the motion of molecules in the nucleus (54, 55).

For instance, a great effort has been done in order to characterize the formation of sub-chromatin domains, and dynamic methods such as FRAP, FLIP and FCS have helped in this important task (48, 56, 57). In addition, Heterochromatin Protein 1-alpha has been shown to be a key regulator of genome organization, and its dynamic has been greatly studied (31, 48, 58–60). FCS has been widely used to study the dynamics of molecules interacting with chromatin, such as transcription factors (61–63), or the polymerases themselves (64). Several other studies have tried to infer something about nuclear organization and chromatin compaction by the study of the motion of inert probes (Fig. 2.2.1) (65–69). In fact, it is possible to retrieve information about nuclear organization even with an inert probe: the motion is free from binding sites, but it is influenced by the environment in term of obstacles to free diffusion and chromatin compactness, apart from molecular crowding. It is also worthy to note that these features can influence the motion of particles in a way that is proportional to the size of the probe used.

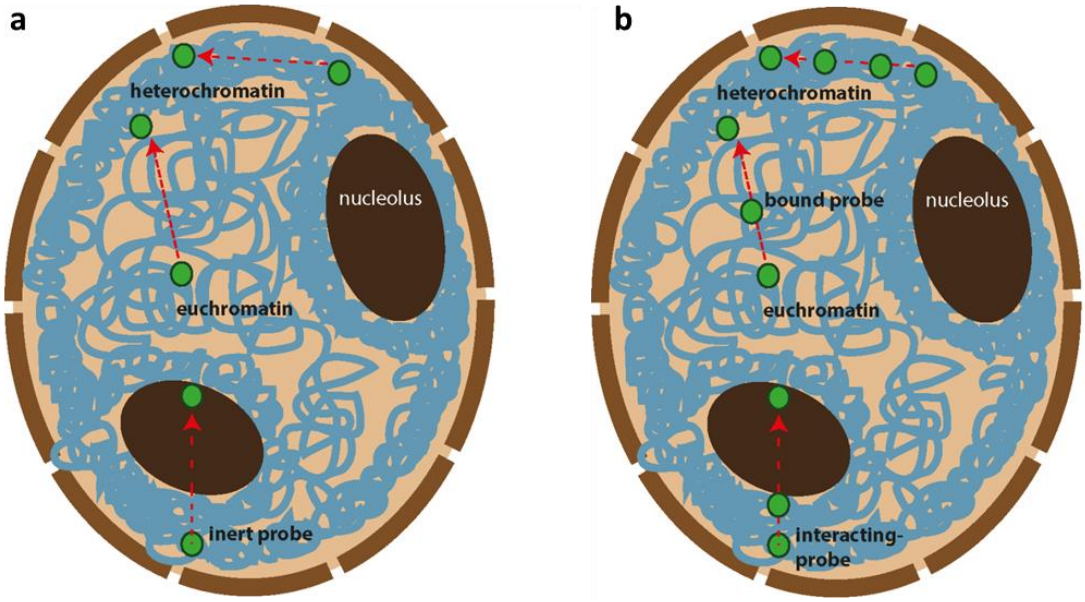

Fig. 2.2.1 Probes for nuclear dynamic measurements. Schematic representation of the difference between inert (a) or interacting (b) probes in the study of nuclear environment.

It is important, as said before, to introduce also a spatial reference into the measurements: since the nuclear environment is highly heterogeneous, probing this heterogeneity by studying potential changes into the surrounding dynamics is a fundamental task. In order to achieve this goal, several strategies have been used that allow the construction of diffusion maps into the nucleus. For example, maps of nuclear diffusion coefficients have been obtained by sequential acquisition of single-point FCS (66), using light sheet illumination (31, 64), or by parallel acquisition of FCS data at multiple observation volumes (63, 70). Recently, a diffusion map in the nucleus of living HeLa cells expressing untagged GFP has been obtained using Local-RICS (34), highlighting differences in diffusion inside a very compact and small environment as the nucleolus.

2.3 Issues

All the FCS methods presented above were successful in studying the dynamics of molecules in the nucleus, even if the environment is crowded and hard to inspect.

Anyway, there are still several issues to be taken into account. For instance, nuclear heterogeneity has different spatial scales, and in some cases the spatial resolution offered by a conventional diffraction limited optical setup is too poor to gain information at the nanoscale organization level. In fact, several chromatin structures seems to have dimension ranging from the tens of nanometers range to less than 150nm (71, 72).

In addition, all the spatially-resolved FCS methods reported above will only provide an accurate description of the mobility properties in different nuclear regions if these regions are immobile during FCS data acquisition.

In the following sections, a novel method that tries to overcome these limitations will be presented.

3. Intensity sorted FCS

In this chapter, a novel method based on an extension of scanning fluorescence correlation spectroscopy (FCS) is presented. Here the data are sorted and analyzed in short time segments: the sorting of segments is based on a fluorescence intensity threshold in the same or a different reference channel. The implementation of this technique on a custom optical setup is explained in section 3.2, while section 3.4 shows the results obtained by the application of the method in the nucleus of living cells, using both inert and interacting probes. In the end, the results and possibly future works are discussed.

3.1 The idea

As shown in the previous chapter, measurements of FCS in specific regions of the nucleus can be hard to perform, especially due to the fact that the nucleus itself is a very dynamic environment, and the structures in exam can move significantly during the acquisition time of a FCS measurement. A significant advantage can be gained if the different chromatin regions are identified with the help of a reference marker (73). For instance, the intensity of a fluorescent protein can be used to identify specific sub-nuclear regions or, simply, the intensity of a DNA marker (e.g. Hoechst) can be used to identify regions of different chromatin density (74). In this case, the reference intensity can be used as a bona fide marker to assign, during data analysis, each single-point FCS measurement to a specific chromatin region. In this respect, the acquisition of a brief FCS measurement is fundamental to ensure that the probed region does not move significantly during each measurement. On the other hand, the poor statistics resulting from a short FCS acquisition must be compensated by averaging over many FCS measurements assigned to the same chromatin region.

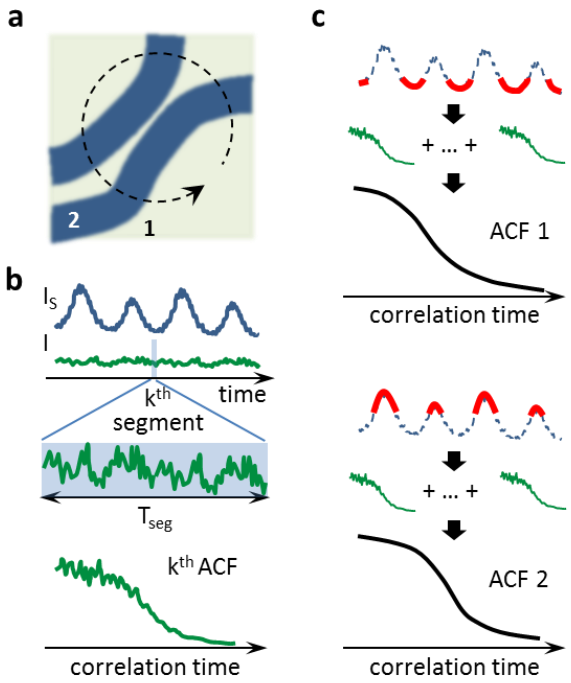

Fig. 3.1.1. Schematic implementation of the method. The excitation spot is scanned in a circular line across the specimen (a) and the fluorescence from one or more channels is continuously recorded (b). The whole measurement is divided into short segments of duration T_{seg} and for each segment the corresponding ACF is calculated (b). The ACFs are then sorted into two or more populations, based upon the value of the reference intensity I_s, and for each population the average ACF is calculated (c).

This idea is implemented by performing a "slow" scanning of the excitation beams across the nucleus. The fluctuation analysis is performed by dividing the whole acquisition into a large number of short temporal segments and considering each segment like an independent FCS measurement, tagged with an intensity value of the reference marker. The ACFs calculated from these short segments are first sorted into two or more populations, corresponding to specific chromatin regions, and then averaged. As a result, this intensity-sorted FCS approach yields, for each measurement, an ACF associated to each chromatin region (Fig. 3.1.1). In addition, since each measurement is acquired from a single cell, it is possible to measure the dynamic properties of different compartments cell-by-cell, thus avoiding the intracellular mobility differences being distorted due to the intercellular variability.

3.2 Technique implementation

The schematic implementation of the method is depicted in Fig. 3.1.1. The excitation volume of a confocal microscope is slowly scanned along a circular line across the specimen (Fig. 3.1.1 a),

similarly to what is done in orbital scanning (16, 37), while the fluorescence intensity from one or more spectral channels is continuously recorded at high temporal resolution (Fig. 3.1.1 b). This slow circular scan acquisition mode should not be confused with the afore-mentioned circular scanning FCS technique (36). Here, the slow scan is a strategy to continuously acquire single-point FCS data at consecutive locations along the scanned path. The whole intensity trace I recorded in one channel is divided into short temporal sequences, or segments, of duration T_{seg} (much shorter than the line scan time) and from each segment a short-sequence (ss) ACF is calculated (Fig. 3.1.1 b). Then the ssACFs are sorted based on the value of intensity I_s associated to each segment (Fig. 3.1.1 c). The intensity I_s used for sorting the ACFs can be the intensity recorded in the same or in another channel. For instance, if the orbit is scanned across two distinct regions (Fig. 3.1.1 a), detectable by a difference in the intensity I_s (Fig. 3.1.1 b), one can obtain an ACF associated to each region by averaging only the ssACFs corresponding to segments whose intensity is below or above a given threshold, respectively (Fig. 3.1.1 c).

The duration T_{seg} of the segments must be short enough to resolve intensity variations in the sorting intensity channel I_s but long enough to properly sample fluorescence intensity fluctuations and prevent deformation of the ACFs. In order to estimate a reasonable lower limit for T_{seg} we simulated molecules undergoing Brownian motion with diffusion coefficient D through a Gaussian observation volume of lateral waist w and axial waist $w_z>>w$. We divided the resulting intensity trace in segments of duration T_{seg}, then the ssACF was calculated and averaged over all segments. The extent of deformation of the ACF depends on the ratio between T_{seg} and the characteristic width of the fluctuations, $t_D=w^2/4D$ (Fig. 3.2.1 a). The deformations of the undersampled ACF were quantified by fitting each ACF to the following function:

$$G^{ss}(t) = G^{ss}(0)\left(1+\frac{t}{t_D^{ss}}\right)^{-1} + b^{ss} \qquad \textbf{(Eq. 7)}$$

And comparing the fitting parameters with those of the ACF calculated with an infinite sampling time:

$$G(t) = G(0)\left(1+\frac{t}{t_D}\right)^{-1} + b \qquad \textbf{(Eq. 8)}$$

Where b is set to 0. For shorter values of T_{seg} the ACF are characterized by shorter values of t_D^s, negative values of b^s, and slightly larger values of the amplitude $G^s(0)$. We can consider $T_{seg} \sim 10^2 t_D$ as a lower limit for the duration of the short-sequence. In fact, for $T_{seg} > 10^2 t_D$, the more meaningful parameters t_D and G(0) deviate by less than 5%, in keeping with the rule of thumb that the acquisition time of FCS data has to be at least two orders of magnitude longer than the characteristic correlation time (75).

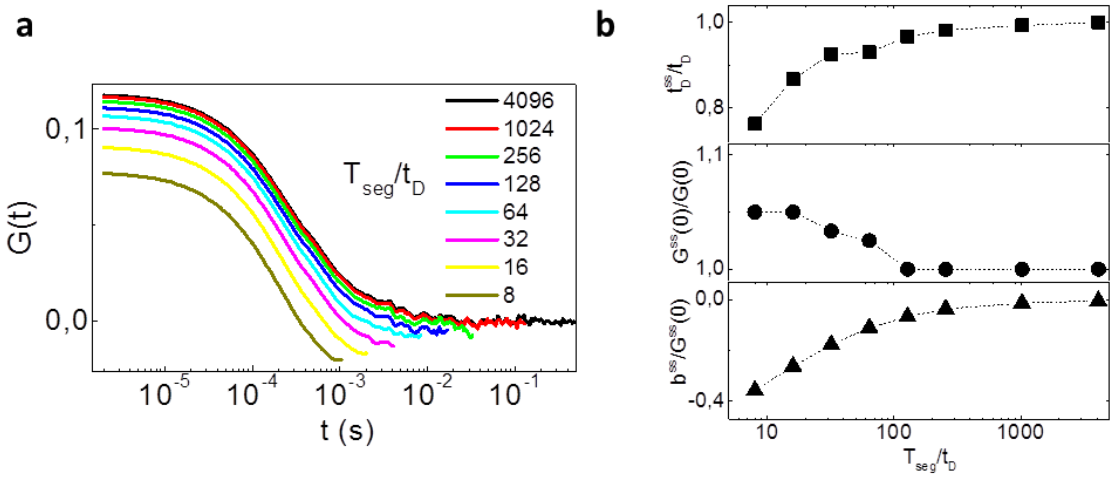

Fig. 3.2.1 Simulations on the effect of the segment length variation. Short-sequence (ss)ACFs calculated from simulated data for different values of T_{seg}/t_D. (a) Deviation of the fitting parameters (Eq.7) of the ssACF for different values of T_{seg}/t_D (b).

Another point to take into account is how slow must we scan in order to ignore the correlations due to the motion of the beam. The complete ACF function that describes a model of free diffusion in circular scanning FCS is given by (76):

$$G(t) = G(0)\left(1+\frac{t}{t_D}\right)^{-1} \exp\left(-\frac{\frac{4R^2}{w_0^2}\sin^2\left(\frac{vt}{2R}\right)}{1+\frac{t}{t_D}}\right) \qquad \textbf{(Eq. 9)}$$

Where R is the radius of the orbit and v is the scanning speed, given by $v=2\pi R/T$, where T is the period of the orbit. In our case, since we sample many segments along the orbit, is $t<T_{seg}<<T$, so we can rewrite **Eq. 9** as:

$$G(t) = G(0)\left(1+\frac{t}{t_D}\right)^{-1}\exp\left(-\frac{\frac{v^2t^2}{w_0^{\,2}}}{1+\frac{t}{t_D}}\right) \qquad \textbf{(Eq. 10)}$$

We can ignore the correlations due to the motion of the scanner whenever $v^2t^2/w_0^2 \ll 1+t/t_D$, namely when $v^2 \ll w_0^2/t^2+w_0^2/(t_D t)$. This condition is certainly satisfied if $v \ll w_0/T_{seg}$ and $v^2 \ll w_0^2/(t_D T_{seg})$. Assuming $T_{seg}=10^2 t_D$, the latter condition can also be written as $v \ll 0.4D/w_0$. For instance, for $D \approx 20\mu m^2/s$ and $w_0 \approx 200nm$, $v \ll 40\mu m/s$. For an orbit diameter of $\approx 3\mu m$ this corresponds to a scanning frequency $f \ll 4Hz$.

3.3 Materials and Methods

3.3.1 Optical Setup

The measurements were performed on a custom microscope, obtained from modification of a previous setup (77). The excitation at 485nm was provided by a pulsed laser line (LDH-D-C-485, 80MHz, PicoQuant, Berlin, DE), while the excitation at 407nm was provided by a continuous-wave (CW) diode laser (Cube 1069413/AQ407nm/50mW, Coherent, Santa Clara, CA, US). The laser power was measured at the objective back aperture. The beams were combined and co-aligned using different laser beam dichroic mirrors, then deflected by two galvanometric scanning mirrors (6215HM40B, CTI, Cambridge Technologies, Bedford, MA, US) and directed toward the 1.40 NA 100x objective (HCX PL APO 100/1.40/0.70 Oil, Leica Microsystems, Wetzlar, DE) by the same set of scan and tube lenses as the ones used in a commercial scanning microscope (Leica TCS SP5, Leica Microsystems, Wetzlar, DE). The fluorescence light was collected by the same objective lens, de-scanned, passed through the laser beam dichroic mirrors, then separated by a fluorescence beam splitter in two channels (detection bands 525/50 nm and 445/45nm) before being focused (focal length 60 mm, AC254-060-AML, Thorlabs, Newton, NJ, US) into fiber pigtailed single-photon avalanche diodes (PDM Series, Micro Photon Devices, Bolzano, Italy). All imaging operations were automated and managed by the software ImSpector (Max Planck Innovation, Munchen, DE) with the exception of circular scanning, managed by the software SimFCS. For FCS measurements, photons were detected by a time-correlated-single-photon-counting (TCSPC) card (SPC-830,

Becker & Hickl, Berlin, DE), synchronized with the reference signal provided by the pulsed diode laser.

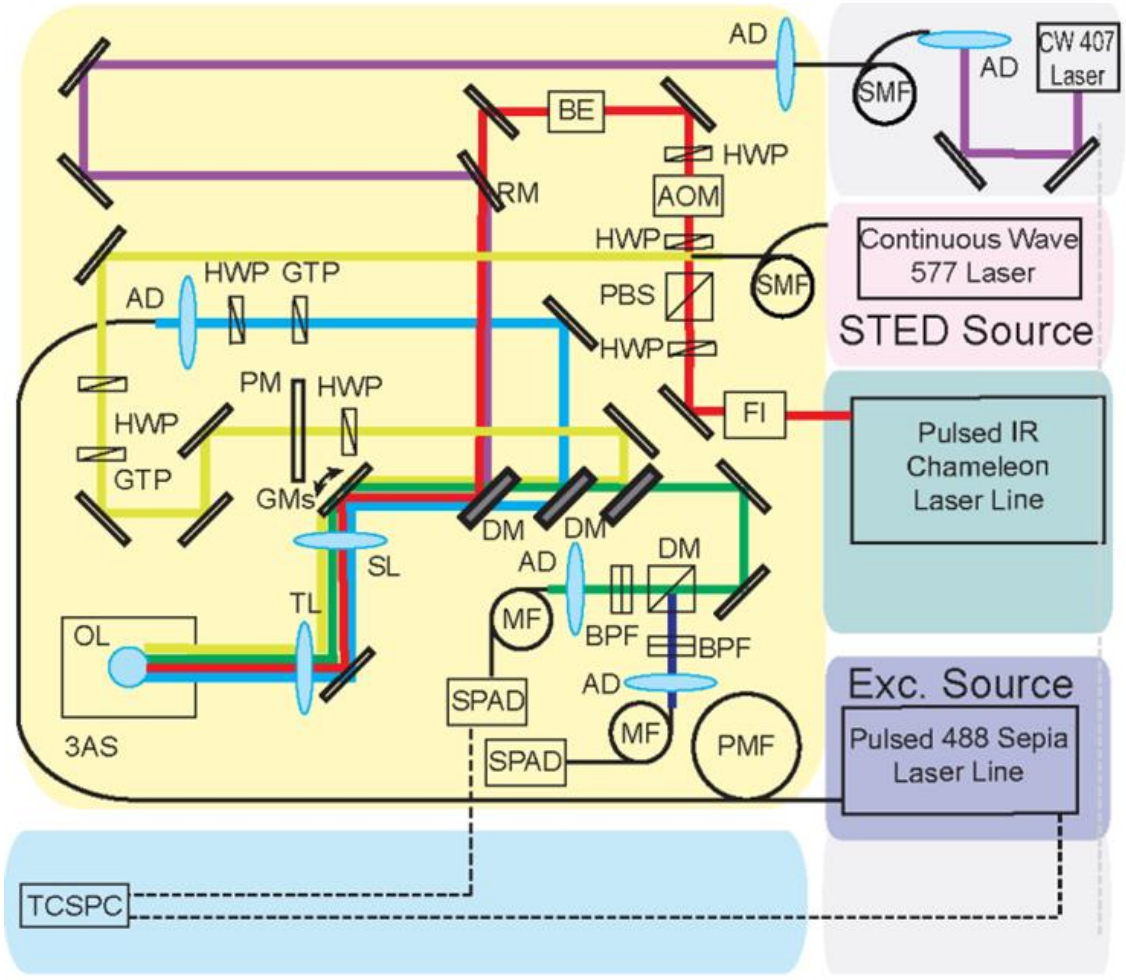

Fig. 3.3.1 Experimental setup. 3AS: three Axis Stage; AD: Achromatic Dichroic; AOM: Acoustic Optical Modulator; BE: Beam Expander; BPF: Band Pass Filter; DM: Dichroic Mirror; FI: Faraday Insulator; GMs: Galvo Mirrors; GTP: Glan-Thompson Polarizer; HWP: Half Wave Plate; MF: Multi-mode Fiber; OL: Objective Lens; PBS: Polarized Beam Splitter; PMF: Photo Multiplier Fiber; RM: Removable Mirror; SL: Scanning Lens; SMF: Single Mode Fiber; SPAD: Single Photon Avalanche Photodiode Detector; TCSPC: Time Correlated Single Photon Counter; TL: Tube Lens. The excitation is provided by a 488nm laser line, that is focused on the sample passing through the objective. Both the STED (577nm continuous wave laser), and the 405nm laser lines were co-aligned in order to be superimposed on the specimen. The fluorescence emitted is split in detection, in order to separate the fluorescence deriving from the Hoechst 33342 (445nm) and from the Green Fluorescence Protein (525nm).

3.3.2 Cell Culture

A stable HeLa cell line expressing the protein AcGFP1 was used for all the untagged-GFP experiments. For the p53 and HP1alfa experiments, a HeLa wild-type (WT) cell line was used for transfection. The cells were cultured in DMEM supplemented by 10% Fetal Bovine Serum, 2mM glutamine, 100U penicillin and 0.1mg/ml streptomycin (Sigma Aldrich, Saint-Louis, MI, US). For the estrogen receptor-α (ER) experiments a stable HeLa cell line with a hundred-copy integration of the estrogen-responsive unit of the prolactin gene (Sharp et al., 2006), which stably expresses a GFP-tagged version of ER (GFP-ERα:PRL-HeLa cell line), was used (78). The GFP-ERα:PRL-HeLa cell line (Sheila) was grown in high-glucose DMEM without phenol red supplemented with 5% charcoal dextran stripped Tet(-)FBS, 200ug/ml Hygromycin B and 0.8 ug/ml Blasticidin S (Thermo Fisher Scientific, Waltham, MA, US) and 1 nM Z-4-Hydroxytamoxifen (Sigma Aldrich, Saint-Louis, MI, US). The day before the experiment, freshly split cells were plated on 8-well chamber (glass bottom, thickness 170±5 μm) (Ibidi, Planegg, DE) and grown overnight.

3.3.3 Treatments

HP1alfa-GFP (AddGene #17652) and p53-GFP plasmid (kindly provided by D. Mazza, The European Center for Nanomedicine, Ospedale San Raffaele) transfection was performed using the Effectene Transfection Kit (Qiagen), following manufacturer's instructions. Nuclear staining was performed incubating the cells for 15min at 37°C with a solution of Hoechst 33342 (Thermo Fisher Scientific, Waltham, MA, US; stock solution 20mM) in PBS, at a final concentration of 4μM. The cells were then washed 4 times with PBS 1X. Energy depletion was obtained incubating the cells for 30min at 37°C with DMEM supplemented with 50mM 2-deoxyglucose (2-DG, Sigma) and 10mM sodium azide (Sigma Aldrich, Saint-Louis, MI, US) (79). Cells were then imaged directly in ATP-depletion medium. Treatment with solutions of different osmolarity was performed by addition to the cell of hypo-(190 mOsm) or hyper-osmolar (570 mOsm) solutions for 15min at 37°C (80): the cells were then imaged directly in the incubation solution. The Sheila cells were treated with 10nM 17-β-estradiol (E2, Sigma Aldrich, Saint-Louis, MI, US) diluted in Live Cell Imaging Solution (Thermo Fisher Scientific, Waltham, MA, US) for one hour to trigger the GFP-ER binding to the array, and then imaged directly in the same incubation solution. In all the other cases measurements were performed on cells kept in Live Cell Imaging solution.

3.3.4 Experiments

All the measurements were performed by scanning a circular orbit through the cells nuclei, chosen in such a way to cross the nuclear regions of interest. For measurements on untagged GFP, the parameters were the following: the 488nm laser power was set to 15μW, while the 405nm laser power at 2.5μW; the orbit diameter was set at 3μm, while the scan period was about 16.7s. Each measurement was recorded for 132s. For the ER and HP1-α experiments, the laser powers of the 488nm and 405 nm were set at 5μW and 1μW, respectively; the orbit diameter was 1.5μm, while the scan period was set to about 68 s, and each measurement lasted 264s. For p53-GFP experiments, the orbit diameter was 1.5μm, while the scan period was set to about 68s, and each measurement lasted 264s. The scan position was chosen in order to cross the perinucleolar heterochromatin (visualized by the Hoechst stain), passing through the nucleolus that will be discarded during the analysis.

3.3.5 Data Analysis and Fitting

Calculation of the intensity sorted ACFs was performed in Matlab. Each measurement file was first divided into segments, whose duration was calculated based on the estimated probe mobility: for untagged GFP, the segment duration was set at about 131ms, while for the HP1-α–GFP, p53-GFP and GFP-ER the segment was 1.05sec long. For each segment, an ACF and an intensity value were calculated. The nanosecond temporal information available in the TCSPC file was used to remove the detector afterpulse in the confocal FCS data, using a custom fluorescence lifetime correlation spectroscopy (FLCS) routine (81). ACFs were only calculated for the green channel, as the Hoechst intensity was used only as a reference channel. Intensity sorting was performed by averaging all the ACFs of segments whose intensity was below and/or above specific threshold values. Variations of the intensity trace due to photobleaching were removed by a non-linear detrend prior to sorting. In all the experiments with untagged GFP, the ACFs were fitted using a one-component diffusion model (**Eq.8**). In the experiments with HP1-α–GFP, p53-GFP and GFP-ER, the ACFs were either fitted using a two-component diffusion model:

$$G(t) = G_{slow}(0)\left(1+\frac{t}{t_{D_{slow}}}\right)^{-1} + G_{fast}(0)\left(1+\frac{t}{t_{D_{fast}}}\right)^{-1} \qquad \textbf{(Eq. 11)}$$

or (for the ER-GFP experiments) the diffusion and binding model (Full model) described in (62). For the two-component diffusion model, a global fit was performed for each experiment,

keeping the two values of diffusion coefficients, D_{slow} and D_{fast}, shared between the measurements and instead letting vary the amplitudes corresponding to the fast and slow diffusing components. One- and two-component diffusion fits were performed in Origin. The Full Model fits were performed in Matlab.

3.3.6 Simulations

All the simulations were performed using SimFCS (available at http://www.lfd.uci.edu/).

3.4 Results

3.4.1 Measurement of the GFP diffusion in the nucleolus vs nucleoplasm

As a validation of the method, differences in the diffusion coefficient of GFP in the nucleolus and the nucleoplasm of HeLa cells were first measured. It has been previously shown that even for a small inert probe like GFP, there is a clear difference in the values of the diffusion coefficient measured in the nucleoplasm in respect to the nucleolus (34, 70, 82). In this case, the GFP intensity level was used as a reference marker to distinguish the two nuclear regions. In fact, the nucleolus of a cell expressing GFP appears dimmer than the nucleoplasm due to a different concentration of GFP in the two compartments (Fig. 3.4.1.1 a, b). The intensity trace showed easily-detectable regions of low and high intensity, corresponding to the nucleolus and the nucleoplasm, respectively (Fig. 3.4.1.1 c). By specifically selecting only the short FCS segments corresponding to these low and high intensity regions (Fig. 3.4.1.1 c), the sorted ACFs corresponding to the nucleolus (Fig. 3.4.1.1 e) and the nucleoplasm (Fig. 3.4.1.1 f) were generated. By the fit of the ACF it was possible to retrieved the averaged (n=13 cells) diffusion coefficient of GFP in the nucleolus (11.3 ±4.5 $\mu m^2/s$, mean ± s.d.) and in the nucleoplasm (21 ± 6.2 $\mu m^2/s$) (Fig. 3.4.1.1 g). These values are in keeping with the values reported in literature (34, 70, 82), demonstrating that our analysis method works properly.

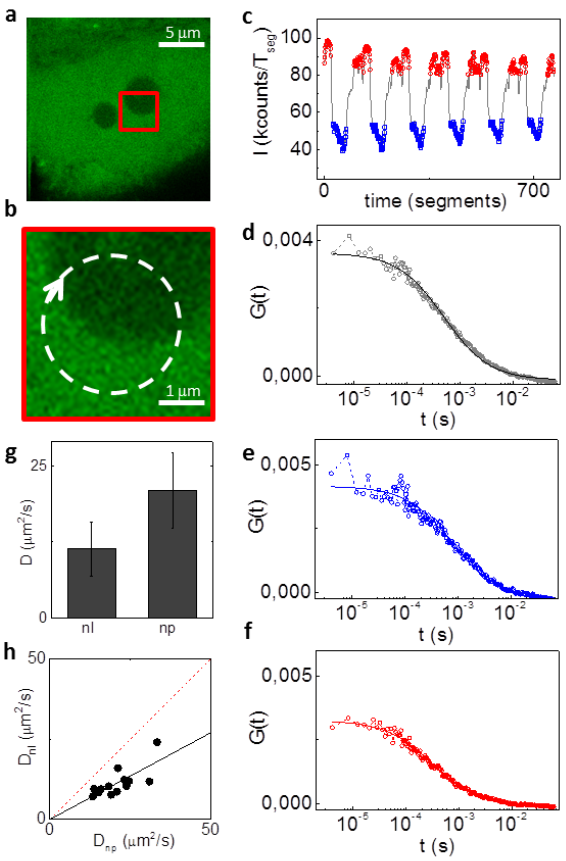

Fig. 3.4.1.1 Measurement of GFP diffusion coefficient in the nucleoplasm and the nucleolus. Each measurement is performed on an individual cell (a), scanning the beams across the nucleolus (b). The GFP intensity trace is used for sorting the ACFs between the nucleolus (in blue) and the nucleoplasm (in red) (c). The total ACF without sorting (d) is compared to the mean ACF calculated from the fluctuations measured in the two regions (e, f). The average diffusion coefficient extracted from the fitting of the ACF of the nucleoplasm is significantly higher (24.3 ± 6.2µm^2/s) than the one shown by GFP in the nucleolus (12.5 ± 2.5µm^2/s) (g). Plot of the ratio between the diffusion coefficients calculated in the two compartments (h), with a linear fit (solid black line, the intercept is fixed to zero) yielding a slope of 0.43. The dashed red line represents the case in which the diffusion coefficients are the same in both the compartments.

Interestingly, there is a high intercellular variability in the measured absolute values of diffusion coefficient (Fig. 3.4.1.1 g, h). However, the ratio between the two values of diffusion coefficient in each cell is quite conserved, as shown by a D_{nl} vs D_{np} scatter plot (Fig. 3.4.1.1 h). The evaluation of this ratio was performed through a linear fit of the data for each independent experiment (Fig. 3.4.1.1 h, Fig. 3.4.1.2): we obtained D_{nl}/D_{np} =0.45 ± 0.02 (mean ± s.d. of the slope values from 5 independent experiments, Fig. 3.4.1.2).

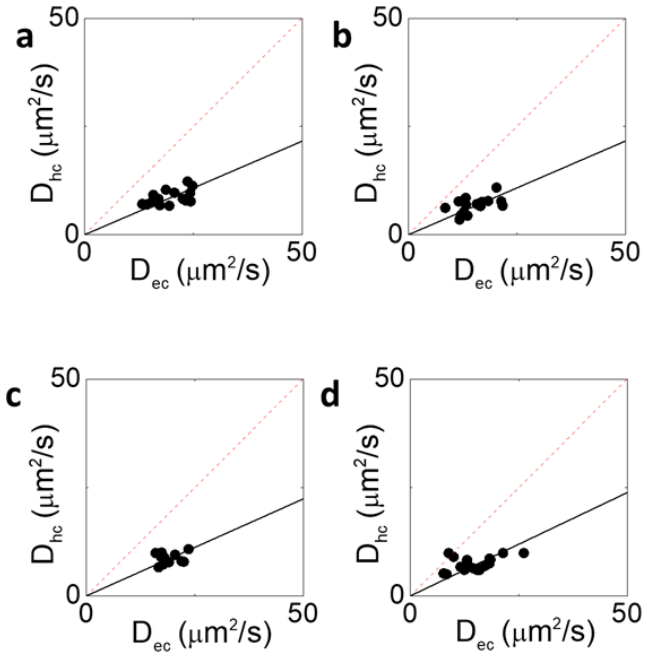

Fig. 3.4.1.2 Results of the additional measurements of untagged GFP diffusion in the nucleoplasm (x-axis) and nucleolus (y-axis). The results indicate the reproducibility of the method, leading to an average slope of 0.45 with a standard deviation of 0.02. (a) Diffusion coefficients calculated on 15 cells with a slope of 0.43. (b) Diffusion coefficients calculated on 15 cells with a slope of 0.43. (c) Diffusion coefficients retrieved from measurements done on 11 cells with a slope of 0.45. (d) Diffusion coefficients calculated on 20 cells, with a slope of 0.48.

These results show, as expected, that the diffusion of GFP is reduced in the nucleolus with respect to the nucleoplasm, due to higher molecular crowding.

3.4.2 Measurement of GFP diffusion in euchromatin vs heterochromatin.

Next, we checked if the technique was able to detect differences of GFP diffusion between regions of high and low chromatin density (hereafter referred to as hetero- and eu-chromatin) using as a reference the intensity of Hoechst-stained DNA (Fig. 3.4.2.1). First, the measurements were performed in the nucleoplasm of HeLa cells, in regions far from the nucleolus (Fig. 3.4.2.1 a, b). In this way, it was possible to use the Hoechst intensity as a quantitative reference for nuclear DNA concentration, defining regions of eu-chromatin (low Hoechst signal) and hetero-chromatin (high Hoechst signal) (Fig. 3.4.2.1 c) and to generate the corresponding ACFs (Fig. 3.4.2.1 d, e).

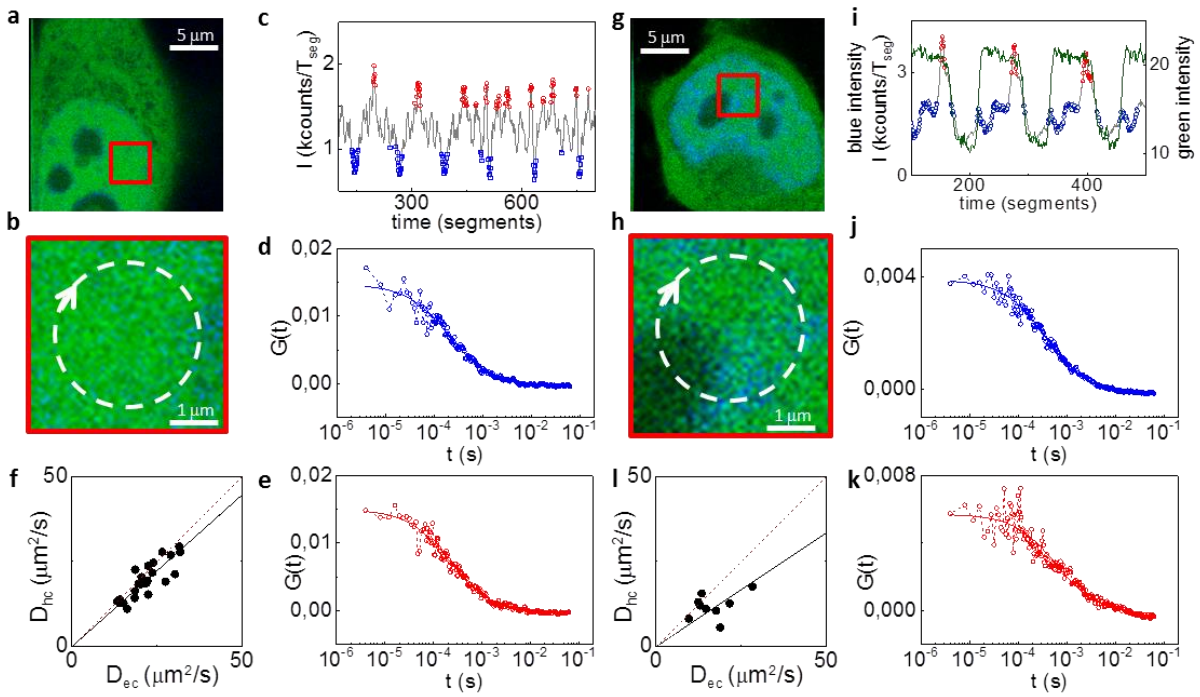

Fig. 3.4.2.1 Measurement of the diffusion coefficient of untagged GFP in eu- vs hetero-chromatin (a-f) and in euchromatin vs perinucleolar heterochromatin (g-k). (a-e) Each measurement is collected from a single nucleus stained with Hoechst (in blue in a, b), far from the nucleolus (b). Basing on the Hoechst intensity trace (c), the FCS segments are sorted into two populations: the heterochromatin, in red, and the euchromatin, in blue. The averaged ACFs are then calculated and a single component fit was performed, giving a value of D_{ec}=31.5µm^2/s for the euchromatin (d) and D_{hc}=29.4µm^2/s for the heterochromatin (e). (f) Scatter plot of the two values of diffusion coefficients D_{hc} and D_{eu} measured on different cells, showing a slightly higher diffusion coefficient in the euchromatin. The solid line is a linear fit through the origin (slope= 0.89). (g-k) When selecting the perinucleolar heterochromatin, the beams are scanned through the periphery of a nucleolus (g,h) and both the GFP (green line) and Hoechst (gray line) intensities are used as references (i). The two average ACFs corresponding to the euchromatin (j) and perinucleolar heterochromatin (k) are calculated and fitted, providing a value of 17.6µm^2/s and 10.6µm^2/s, respectively. When results from the analysis of multiple cells are displayed in a scatter plot (l), a more marked difference between the two values of diffusion coefficient is observed (slope =0.7).

The differences found in the values of the diffusion coefficient of GFP (n=23 cells) between euchromatin (21.8 ± 5.6 µm^2/s) and heterochromatin (19.6 ± 5.4 µm^2/s) were not significant when considering the average of measurements performed on multiple cells. Conversely, in the scatter plot of the two values of diffusion coefficients measured in each cell (Fig. 3.4.2.1 f), the ratio between the diffusion coefficient in hetero- and eu-chromatin was less than 1

(D_{hc}/D_{eu}= 0.87 ± 0.05, mean ± s.d. of the slope values from 5 independent experiments, Fig. 3.4.2.2), despite the high variability between measurements performed on different cells.

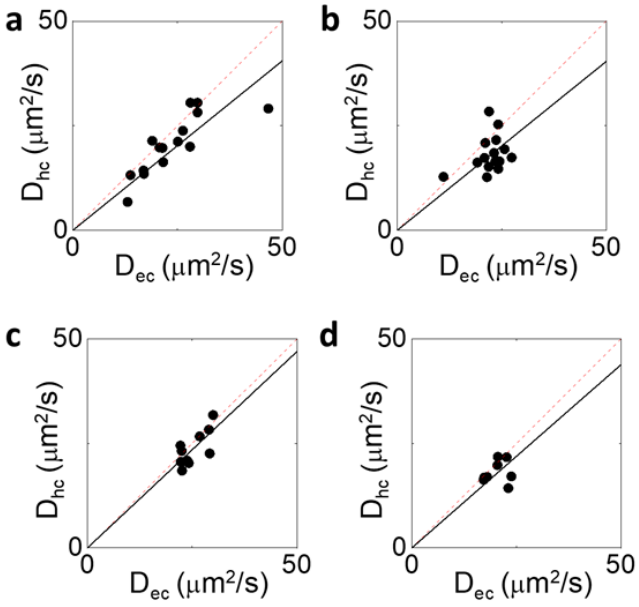

Fig. 3.4.2.2 Results of the additional measurements of untagged GFP diffusion performed on the nucleoplasm of cells marked with Hoechst. For each experiment the diffusion coefficients calculated on heterochromatin (y-axis) and euchromatin (x-axis) are plotted (a) Diffusion coefficients calculated on 16 cells, with a slope of 0.81 (b) Measurements done on 15 cells, with diffusion coefficients linear fit having a slope of 0.81. (c) Diffusion coefficients measured on 10 cells, with a slope of 0.94. (d) Diffusion coefficients retrieved on 8 cells, with a slope of 0.88.

Interestingly, the technique highlighted a greater difference in the case of perinucleolar heterochromatin (Fig. 3.4.2.1 g-k). In this case, the beams were scanned across the perinucleolar heterochromatin (Fig. 3.4.2.1 g-h) and both the GFP and Hoechst intensities were used as references to discard the FCS segments belonging to the nucleolus (low GFP signal), and generate the ACFs corresponding to the perinucleolar heterochromatin (high GFP signal, high Hoechst signal) and the euchromatin (high GFP signal, low Hoechst signal) (Fig. 3.4.2.1 i-k). For the perinucleolar heterochromatin a ratio of D_{hc}/D_{eu}= 0.7 ± 0.07 (mean ± s.d. of the slope values from 4 independent experiments, Fig. 3.4.2.1 l, Fig. 3.4.2.3) was obtained.

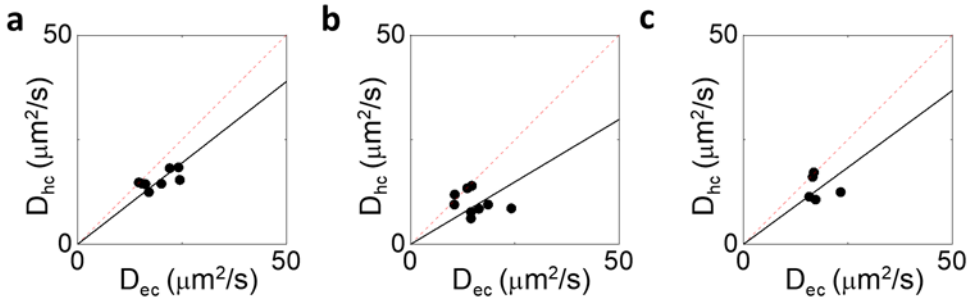

Fig. 3.4.2.3 Results of the additional measurements of untagged GFP diffusion in euchromatin (x-axis) versus perinucleolar heterochromatin (y-axis). (a) Diffusion coefficients calculated on 8 cells, with a slope of 0.78. (b) Measurements done on 9 cells, with the diffusion coefficients linear fit having a slope of 0.6. (c) Diffusion coefficients measured on 5 cells, with a slope of 0.73.

3.4.3 Monitoring the diffusion coefficient of GFP during chromatin compaction changes

In order to test in which extent chromatin compaction affects GFP diffusion in different chromatin regions, the cells were treated with solutions known to induce changes in the compaction of chromatin. Solutions of different osmolarities induced visible changes in nuclei morphology (Fig. 3.4.3.1 a, e, i) that are reflected in a large difference in the diffusion coefficients of GFP measured in different compartments. Indeed, if the cells were treated with a hypo-osmolar solution, the diffusion coefficient of GFP was higher than in controls (D_{eu}=30.1 ± 7.8μm^2/s and D_{hc}=29.6 ± 6.8μm^2/s, mean ± s.d., n = 9 cells); when the cells were subjected to hyper-osmolar treatment, the diffusion coefficients calculated in both eu- and hetero-chromatin were significantly lower (D_{eu}=7.2 ± 2.3μm^2/s and D_{hc}=6.7 ± 2.3μm^2/s, mean ± s.d., n = 10 cells) compared to the controls (D_{eu}= 23.5 ± 8.1μm^2/s and D_{hc}=19.4 ± 6.1μm^2/s, mean ± s.d., n = 10 cells).

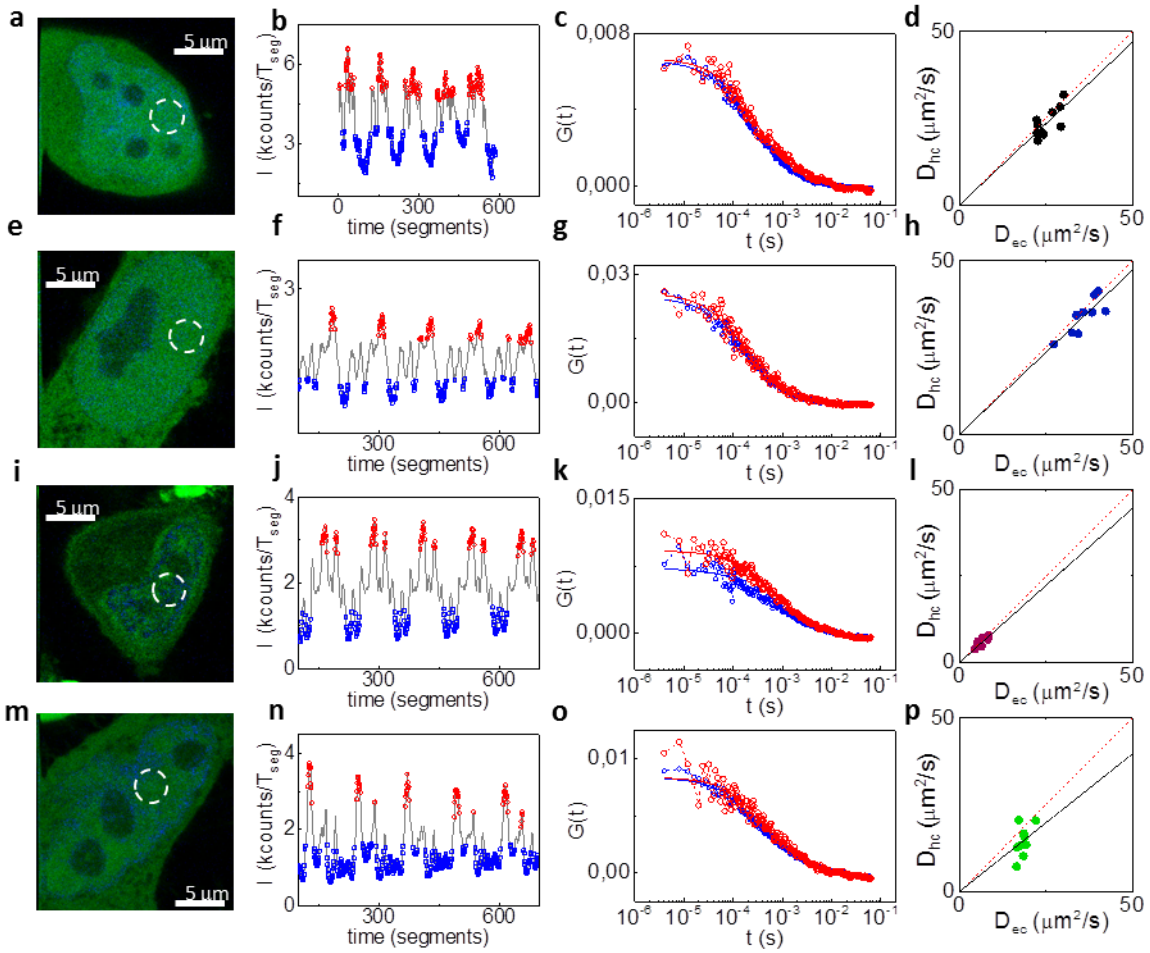

Fig. 3.4.3.1 Measurement of the untagged GFP diffusion coefficient after treatments affecting chromatin compaction state. All the measurements were performed comparing eu-and heterochromatin in the nucleoplasm of HeLa cells. (a-d) Control cells; (e-h) cells treated with a hypo-osmolar solution; (i-l) cells treated with a hyperosmolar solution; (m-p) cells treated with an ATP-depletion solution. The FCS segments are sorted based on the Hoechst intensity (b, f, j, n), to obtain average ACFs for eu- (blue) and hetero- (red) chromatin (c, g, k, o). With respect to the control (d, slope=0.94), the osmotic treatment greatly affects the absolute values of the diffusion coefficients, but not the ratio between them (h, slope=0.95; l, slope=0.89). The ATP-depleted cells show a less marked difference in the absolute values, but a higher difference between the diffusion coefficients calculated in the two compartments (p, slope=0.79).

Interestingly, both the treatments affected only the absolute values of the diffusion coefficients, but not their average ratio D_{hc}/D_{ec}, which was 0.92 ± 0.03 (mean ± s.d. of the slope values from 2 independent experiments, Fig. 3.4.3.2 b) for the hyper-osmolar treatment,

and 0.98 ± 0.03 (mean ± s.d. of the slope values from 2 independent experiments, Fig. 3.4.3.2 a) for the hypo-osmolar one (Fig. 3.4.3.1 h, l), meaning that the treatment has a similar impact on both eu- and hetero-chromatin compartments. Incubation with an ATP depletion solution induced a visible compaction of chromatin with respect to the control (Fig. 3.4.3.1 a, m), which led to a reduction of GFP diffusion coefficients in both eu- and hetero-chromatin (D_{eu}=18.1 ± 4.7μm^2/s and D_{hc}=15 ± 4.9μm^2/s, mean ± s.d., n = 9 cells). In this case, however, the scatter plot of D_{hc} vs D_{ec} (Fig. 3.4.3.1 p) indicates that ATP depletion results in a more prominent slow-down of GFP diffusion in heterochromatin (D_{hc}/D_{eu}= 0.79 ± 0.08, mean ± s.d. of the slope values from 3 independent measurements, Fig. 3.4.3.2 c-e), possibly as a consequence of a larger increase of compaction in hetero- with respect to eu-chromatin.

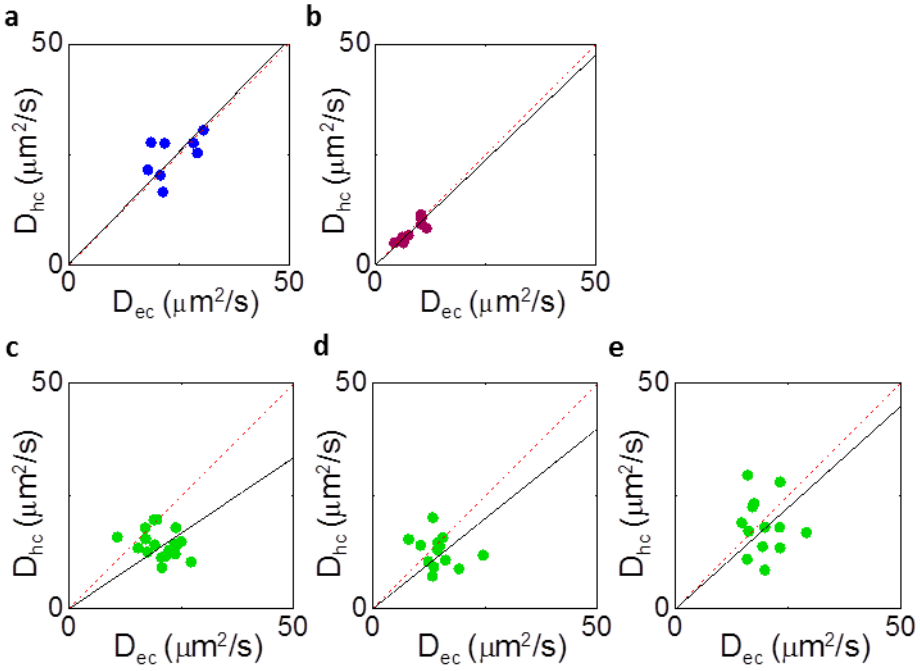

Fig. 3.4.3.2 Results of the additional measurements of untagged GFP diffusion in eu- vs hetero-chromatin after treatments affecting chromatin compaction. The measurements were performed comparing eu- (x- axis) and heterochromatin (y-axis) in the nucleoplasm of HeLa cells. (a) Diffusion coefficients calculated on 8 cells treated with an hypo-osmolar solution, with a slope of 1 (b) Diffusion coefficients measured on 10 cells treated with a hyperosmolar solution, with a slope of 0.95. (c-e) Repetition of measurement of the untagged GFP diffusion coefficient after the ATP-depletion treatments. (c) Diffusion coefficients calculated on 18 cells with a slope of 0.67. (d) Measurement done on 13 cells with diffusion coefficients linear fit having a slope of 0.8. (e) Diffusion coefficients measured on 13 cells with a slope of 0.9.

3.4.4 Mobility of an interacting protein in different chromatin regions

To show the applicability of the method also in using interacting probes, the mobility of three different proteins known to interact with chromatin, i.e. the transcription factor p53, the heterochromatin protein 1 (HP1-α) and the estrogen receptor- α (ER), were studied.

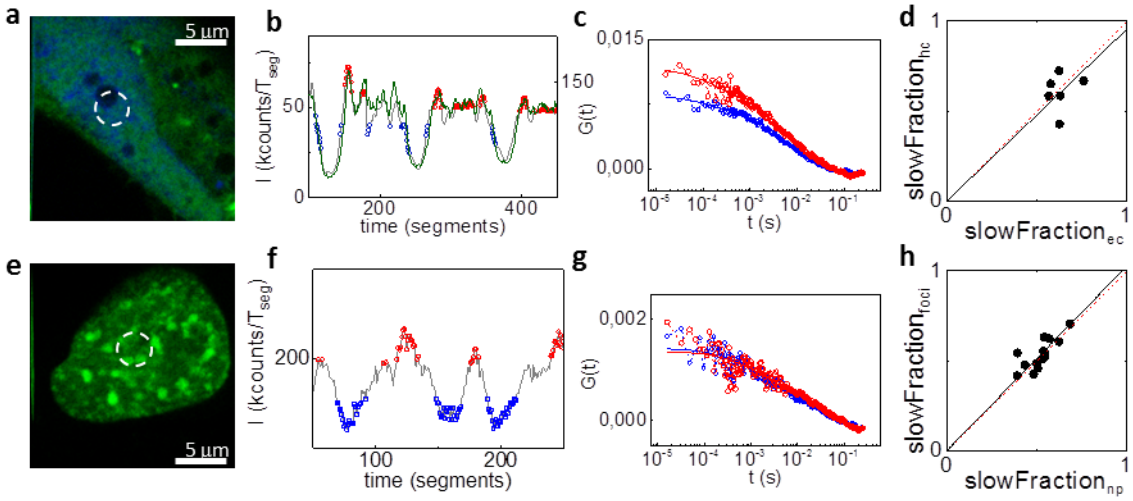

Fig. 3.4.4.1 Measurement of the mobility of interacting proteins in the nucleus: p53 and HP1-α. (a-d) In the case of p53-GFP, the measurements were performed orbiting across the perinucleolar heterochromatin. (b) The intensities of both the Hoechst and the GFP signals are used as a reference for sorting the ACFs corresponding to the perinucleolar heterochromatin (red) and to the euchromatin (blue). (c, d) Analysis with a two-diffusion component model. (c) A global fit performed on the sorted ACFs (red: sorted ACF of the perinucleolar heterochromatin, blue: sorted ACF of the euchromatin) yields a shared value of diffusion coefficients D_{slow}= 0.5µm^2/s for the slow diffusing population and D_{fast}= 8µm^2/s for the fast diffusing one. (d) Scatter plot of the slow fraction calculated in the two probed nuclear regions (slope= 0.96). (e-h) In the case of HP1-α, the measurements were performed orbiting across the HP1-α foci. (f) The intensity of the HP1-α GFP signal is used as a reference for sorting the ACFs corresponding to the foci (red) and to the nucleoplasm (blue). (g) Global fit performed on the sorted ACFs, with a shared value of diffusion coefficients D_{slow}= 0.29µm^2/s for the slow diffusing population and D_{fast}= 6.7µm^2/s for the fast diffusing one. (d) Scatter plot of the slow fraction calculated in the two probed nuclear regions (slope= 1.03).

The diffusion of the well-known transcription factor p53, whose importance is stressed also by its appointment as "the guardian of the genome", was studied in the nucleoplasm and in the perinucleolar heterochromatin (Fig. 3.4.4.1 a-d). The slow fraction (0.5 µm^2/s) seemed to be slightly higher in the heterochromatin, the fitting curve having a slope of SF_{hc}/SF_{np} = 0.91 ±

0.03 (mean ± s.d. of the slope values from 3 independent measurements, Fig. 3.4.4.2 a, b) (Fig. 3.4.4.1 d).

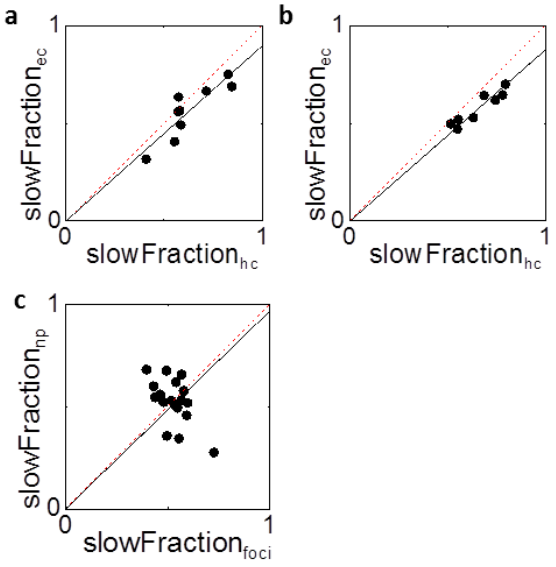

Fig. 3.4.4.2 Results of the additional measurements of interacting proteins diffusion in different nuclear compartments. (a-b) Repetition of measurements done on the mobility of p53 in the perinucleolar heterochromatin (x-axis) and in euchromatin (y-axis). The slow diffusing fraction of protein calculated in the perinucleolar heterochromatin is plotted against the fraction retrieved from the euchromatin. (a) Slow diffusing p53 fraction calculated on 9 cells with a slope of 0.9. The two diffusion coefficients retrieved are 8.63μm^2/s and 0.49 μm^2/s. (b) Slow diffusing p53 fraction calculated on 8 cells with a slope of 0.88. The two diffusion coefficients retrieved are 7.88 μm^2/s and 0.36 μm^2/s. (c) Repetition of measurements done on the mobility of HP1-α inside (x-axis) and outside (y-axis) the typical protein foci. The slow diffusing fraction of protein on the protein foci is plotted against the fraction retrieved from the nucleoplasm. (a) Slow diffusing HP1-α fraction calculated on 19 cells with a slope of 0.97. The two diffusion coefficients retrieved are 25.3μm^2/s and 0.27 μm^2/s.

In the experiments involving HP1-α, an important protein involved in the generation and maintenance of the heterochromatin, the beam was scanned through the protein foci, distinguishable with the same 488nm channel because brighter than the nucleoplasm (Fig. 3.4.4.1 e-h). In this case, the slow diffusive (0.3 μm^2/s) fraction seemed the same in the two compartments probed (SF_{foci}/SF_{np} = 1 ± 0.03, mean ± s.d. of the slope values from 2 independent measurements, Fig. 3.4.4.2 c) (Fig. 3.4.4.1 h)

Finally, the mobility of the estrogen receptor-α (ER), a transcription factor member of the

nuclear receptor super-family and involved in regulation of specific genes in response to hormone binding, was investigated. In particular, the mobility of GFP-ER was tested in the surroundings of an engineered, readily- visible prolactin reporter gene "array" following stimulation with 10nM 17-β-estradiol for 1 hour (Fig. 3.4.4.3 a, b). Using GFP-ER intensity as a reference, the diffusion inside (high GFP-ER signal) and outside (low GFP-ER signal) the array (Fig. 3.4.4.3 c) was measured.

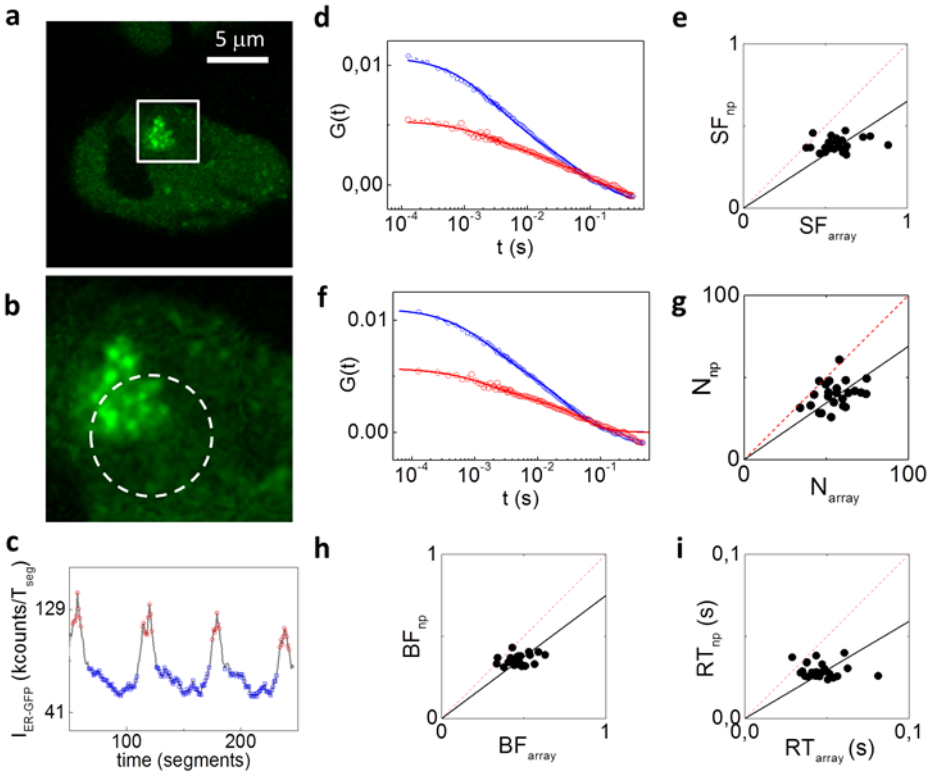

Fig. 3.4.4.3 Measurement of the mobility of the estrogen receptor (ER) inside and outside an engineered prolactin gene array. (a, b) The measurements were performed orbiting across the prolactin gene array. (c) The intensity of the GFP-ER signal is used as a reference for sorting the ACFs corresponding to the array (red) and to the nucleoplasm (blue). (d,e) Analysis with a two diffusion component model. (d) A global fit performed on the sorted ACFs (red: sorted ACF of the array, blue: sorted ACF of the nucleoplasm) yields a shared value of diffusion coefficients D_{slow}=0.07µm^2/s for the slow diffusing population and D_{fast}=2.1µm^2/s for the fast diffusing one. (e) Scatter plot of the slow fraction calculated in the two probed nuclear regions (slope= 0.65). (f-i) Analysis with the Full Model, showing the fitted ACFs (f) and the scatter plots of the number of proteins (g, N_{np}/N_{array} =0.69), the bound fraction (h, BF_{np}/ BF_{array} = 0.75) and the residence time (i, RT_{np}/RT_{array}= 0.59) for the nucleoplasm and for the array.

The intensity-sorted ACFs were fitted using either a two components pure diffusion model or

a Full Model (FM) taking into account diffusion and binding (62). In the first case a slow (D_{slow}=0.07 μm^2/s) and a fast diffusing component (D_{fast}=2.1μm^2/s) were identified, in keeping with previous reports (83). Then the slow fraction (SF), calculated as $SF=G_{0slow}/(G_{0slow}+G_{0fast})$, inside ($SF_{array}$) and outside ($SF_{np}$) the array (Fig. 3.4.4.3 e) was plotted. The result of the fit with the two-component diffusion model (Fig. 3.4.4.3 d), shows that the slow diffusing fraction was significantly higher in the array compared to the nucleoplasm, with a ratio SF_{array}/SF_{np}= 0.73 ± 0.06 (mean ± s.d. of the slope values from 3 independent experiments, Fig. 3.4.4.3 e and Fig. 3.4.4.4). Then the fit was performed again, using the FM model, which is more general and yields several outputs including the number of particles (N), the bound fraction (BF) and the protein residence time (RT) on its binding site (62) (Fig. 3.4.4.3 g-i). Reflecting the increased density of estrogen response elements (EREs) at the engineered transcription locus, the number of ER molecules was higher in the array than in the nucleoplasm (N_{np}/N_{array}=0.67 ± 0.03, mean ± s.d. of 3 independent experiments, Fig. 3.4.4.3 g and Fig. 3.4.4.5 a, d).

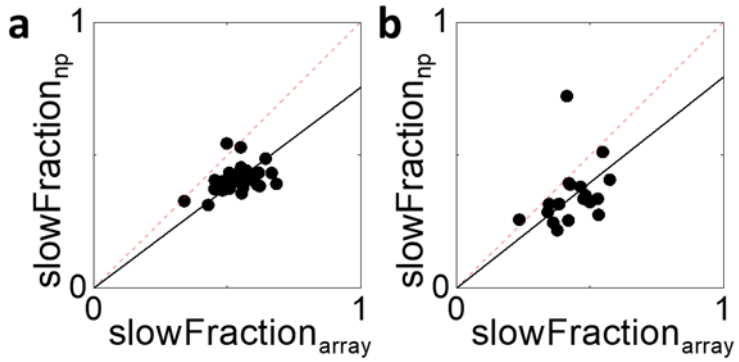

Fig. 3.4.4.4 Repetition of measurements done on the mobility of the Estrogen Receptor inside (x-axis) and outside (y-axis) a nuclear array of prolactin genes, after stimulation with 10nM 17-β-estradiol for 1 hour. The slow diffusing fraction of protein calculated on array is plotted against the fraction retrieved from the nucleoplasm. (a) Slow diffusing ER fraction calculated on 30 cells with a slope of 0.75. The two diffusion coefficients retrieved are 3.1μm^2/s and 0.1 μm^2/s. (b) Slow diffusing ER fraction calculated on 19 cells with a slope of 0.79. The two diffusion coefficients retrieved are 3 μm^2/s and 0.1 μm^2/s.

Also, the fraction of molecules in a bound state was significantly higher on the array (BF_{np}/BF_{array} =0.83 ± 0.07, mean ± s.d. of 3 independent experiments, Fig. 3.4.4.3 h and Fig. 3.4.4.5 c, f). Finally, the average time the ER is found in the bound state was longer on the array (RT_{np}/RT_{array}= 0.65 ± 0.04, mean ± s.d. of 3 independent experiments, Fig. 3.4.4.3 i and Fig. 3.4.4.5 b, e).

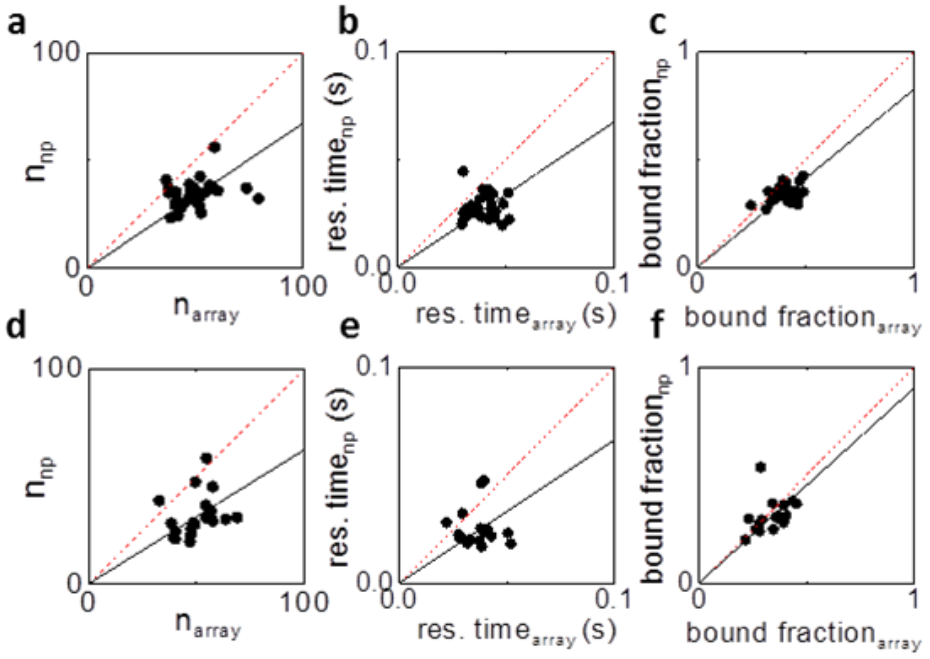

Fig. 3.4.4.5 Repetition of measurements done on the mobility of the Estrogen Receptor inside (x-axis) and outside (y-axis) the array of prolactin genes, fitted by a Full Model. The measurements are performed on 30 (a-c), and 18 cells (d-f) plotting the number of molecules (n) found in the two regions (a, d; slopes 0.68 and 0.63, respectively), the average residence time of the ER on the binding site (b, e; slopes 0.68 and 0.67, respectively) and the fraction of bound protein (c, f; slopes 0.83 and 0.91, respectively).

3.5 Discussion

In this chapter, an extension of the scanning FCS method for measurements in heterogeneous systems like the nucleus was presented. The Intensity Sorted-FCS method is based on slow, orbital-scanning FCS which gives as a result a whole photon trace: this is then split by intensity into segments that are analyzed individually. Here, the changes in intensity (on the main or on some additional channel) reflect the differences in chromatin structure. Then the FCS autocorrelation function (ACF) measured on each segment is bundled with other similar segments and the ACF decay in different regions of the nuclei can be compared with reasonable statistics.

The method was used to probe the diffusion of inert GFP in different nuclear domains. As expected, the diffusion was slowed down in the nucleolus relative to the nucleoplasm, presumably due to higher molecular crowding. It is worth noting that the FCS segments corresponding to the interface between the two regions (Fig. 3.4.1.1 c) were not used in the analysis, as they are expected to show a mixed behavior. However, the capability of measuring mobility of proteins at

the boundary of nuclear domains could be of interest for models of chromatin organization based on phase separation (48). When studying the GFP mobility in hetero- vs eu-chromatin, the slight difference between the diffusion coefficients is more marked when eu-chromatin is compared to perinucleolar heterochromatin. A variation of the mobility of GFP was also appreciable when using treatments that alter chromatin structure. These results indicate that, even for a small inert probe like GFP, chromatin and its compaction states can markedly influence diffusion rates, allowing the possibility of using such small inert probes to study chromatin organization and nuclear rheology in living cells. In fact, the single cell sensitivity of this method facilitates stressing the differences in protein mobility within different chromatin regions, without being affected by the intercellular variability. Indeed, previous FCS studies have been incapable of identifying differences in the mobility of monomeric GFP in nuclear compartments with different chromatin density (66). These results show instead that even the motion of a small inert probe (monomeric GFP) is affected by the higher degree of compaction of the heterochromatin regions. In this respect, a higher accuracy in the presented data may result from several important characteristics of the method. First of all, the high (microsecond) temporal resolution of the ACF ensures a proper sampling, especially if compared to scanning FCS (millisecond temporal resolution). Second, the efficient sorting of the short FCS measurements ensures that fluctuations are averaged only between regions with the same intensity-based fingerprint (for instance, in the case of heterochromatin, these are only the regions identified by the Hoechst peaks), even if these regions are not completely immobile during the whole acquisition. This is conceptually similar to performing FCS on a tracked subcellular region (84–86), although this tracking is performed *a posteriori* on the recorded intensity profile. A similar idea has been exploited in the context of RICS to perform fluctuation analysis on specific organelles (73). Finally, another advantage of this approach is the possibility of obtaining cell-by-cell estimates of the diffusion coefficients for each of the probed nuclear regions. In addition, this method has proven to be useful also in the study of proteins that interacts with chromatin, being able to discriminate between diffusion measured in different nuclear compartments. Although for p53 and HP1-α were not found high differences, the method was indeed capable of distinguish between regions of hetero-chromatin (in the case of p53) or high concentration of fluorescent probes (in the case of HP1- α). In the second case, the ACFs calculated on the foci were strongly deformed by the non-diffusing component (the protein bound at the focus) and by its bleaching during the measurement, which results in a strong biased correlation. The fit was thus biased too, and this can be causal to the failure in detecting differences in the protein motion. A pre-bleaching step before the measurement may allow, in the future, a better estimation of the diffusion coefficients. The same issue was

encountered during ER measurements; thus, the array was pre-bleached in order to avoid the ACF deformation. In this case, the method was able to detect differences in diffusion at an engineered prolactin gene array (e.g., transcription locus), where the number of EREs and receptor proteins is higher than in the nucleoplasm. Interestingly, the use of a different fit (e.g. the Full Model fit), allows to retrieve important information about the binding and the residence time of the proteins on the array versus the other binding sites scattered throughout the nucleoplasm. The results indeed show that not only is more ER targeted to the gene array (e.g., brighter signal), but also a larger fraction of ER is in a bound state – rather than freely diffusing – at the gene array. Although there are thousands of ER binding sites present throughout the nucleus, ERE density within the prolactin gene array recruits and retains the receptor longer than elsewhere in the nucleoplasm.

In summary, this new, statistically robust method can be used to perform accurate mobility measurements, at microsecond temporal resolution, in different compartments without the constraint of having the probed regions nearly immobile during FCS measurements. In addition, intensity sorted FCS is suitable to study the diffusion of small inert probes, but also the interaction of proteins with a slowly moving substrate.

4. Intensity Sorted FCS on a commercial laser scanning microscope

This chapter will describe the implementation of the Intensity Sorted FCS method in a commercial setup. The main advantage of the 'slow' scan implementation described in the previous chapters is that it is possible to analyze the data as they were acquired in a single-point modality (ignoring the motion of the beams), thus keeping a high (microsecond) temporal resolution, which ensures a proper sampling of the ACFs and allows the study of highly dynamic processes. Unfortunately, this mode of acquisition is not available on commercial laser scanning microscopes (LSMs) but requires a customized hardware control. On the other hand, scanning FCS can be implemented in most commercial LSMs by autocorrelating the signal detected at each pixel during a fast line scanning acquisition. The temporal resolution of line scanning FCS is typically limited to the ~ms range. Here, I will show the results obtained on measurements done on interacting proteins, whose average diffusion time is relatively longer than that of untagged GFP, so the high temporal resolution of single-point FCS is not required. The experiments reported in this chapter are done in collaboration with the group of Prof. Michael Mancini at the Baylor College of Medicine, in Houston.

4.1 Technique implementation

In line-scanning FCS, the observation volume is linearly scanned on the sample with line frequency f (Fig. 4.1.1 a). Note that, since the temporal resolution is determined by the line scanning frequency, in this case the characteristic line time T=1/f must be shorter than the average diffusion time, for a proper sampling of the ACF (36, 75). The intensity traces of the line scans are arranged vertically to form a pseudo-image (Fig. 4.1.1 b), in which the horizontal axis indicates the position along the line and the vertical axis represents the time t_i, an integer multiple of the scanning period T. For each position x, an autocorrelation function (ACF) is obtained by correlating the intensity along the temporal axis:

$$G(x,\tau_i) = \frac{\langle \delta F(x,t_i) \times \delta F(x,t_i+\tau_i) \rangle}{\langle F(x,t_i) \rangle^2} \qquad \textbf{Eq. 12}$$

Here $\langle\ \rangle$ denotes the average over all positions x and scans i. x_i is the spatial lag variable and $\tau_i = iT$ is the discrete lag time.

Thus, each column of the pseudo-image is treated as a single-point measurement, and is correlated with the pixels in the same spatial position but in the lines below (correlated in time).

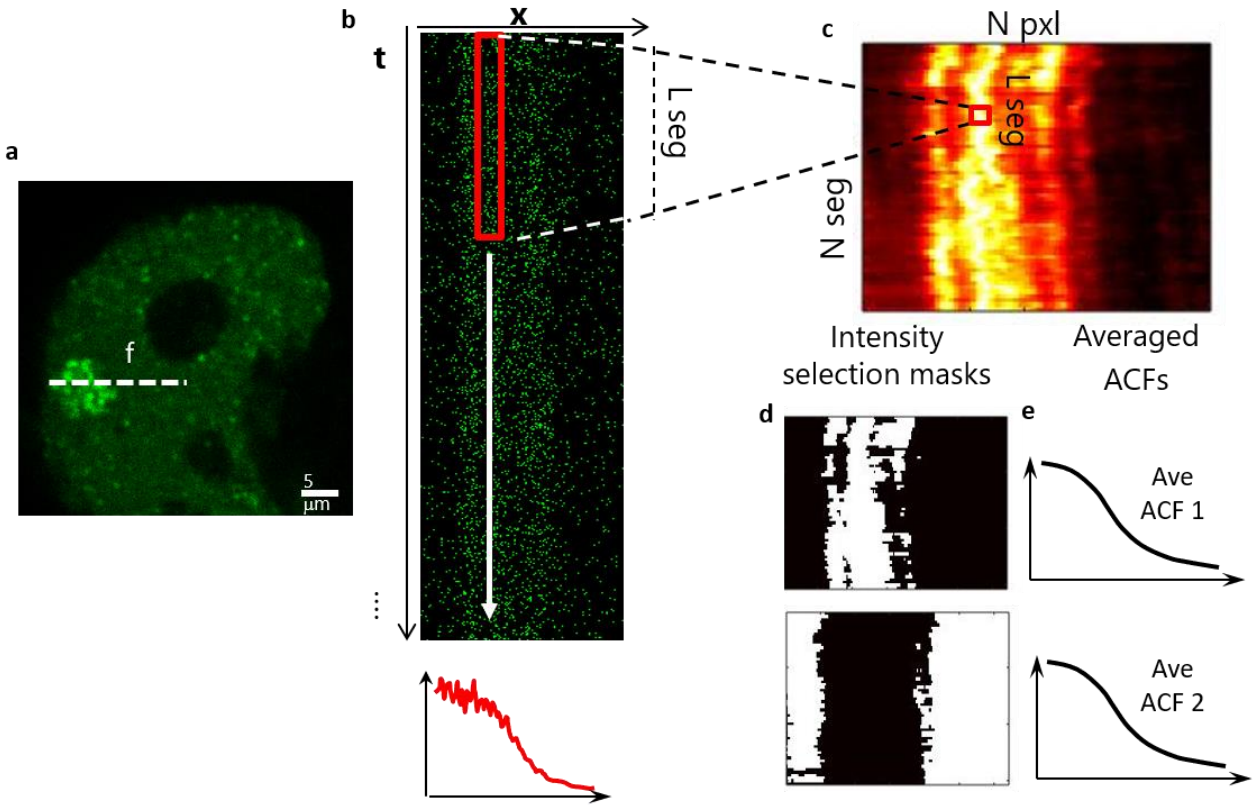

Fig. 4.1.1 Schematic representation of the implementation of the Intensity Sorted-FCS method in a commercial LSM. A line is repeatedly scanned on a sample (a), and each line is arranged vertically depending on the time of the acquisition, to generate a pseudo-image whose dimensions are (x, t) (b). The pseudo-image is divided into N smaller pseudo-images, and inside each pseudo-image, an ACF is generated for each pixel (b). The intensity image is built using the total photon count of each segment, (c). On this image, two selection masks are chosen basing on a low and high user-defined threshold (d), and the ACFs were sorted and averaged basing on these masks (e).

This method thus produces N_{pxl} ACFs, where N_{pxl} is the number of pixel in a line. To perform the intensity sorting, the whole pseudo-image is segmented into N_{seg} smaller pseudo-images of size $N_{pxl} \times L_{seg}$, where $L_{seg}= T_{seg}/T$ (Fig. 4.1.1 b). For each segmented pseudo-image, we calculate N_{pxl} ACFs according to Eq. 12. Thus, the total number of segments ACFs obtained in this case is $N_{pxl} \times N_{seg}$. To efficiently sort the segment ACFs, the total photon counts detected during each segment are represented as an intensity image. This image will thus have a dimension of N_{pxl} on the x-axis and N_{seg} on the y-axis (Fig. 4.1.1 c). On this image, two selection masks are decided (Fig. 4.1.1 d), basing on a user-defined threshold, to define two different chromatin regions (for instance, on the array versus outside the array). Finally, all the segment ACFs in each region are averaged, yielding the two sorted ACFs corresponding to the two regions (Fig.

4.1.1 e). Note that, also in this case, the duration of the segment T_{seg} must be based on the diffusion scale of the proteins studied.

4.2 Materials and Methods

4.2.1 Optical setup

The experiments were performed on a Leica TCS SP5 gated- STED microscope, using a HCX PL APO ×100 100/1.40/0.70 oil immersion objective lens (Leica Microsystems, Mannheim, Germany). A pre-bleaching step was accomplished with a 592 nm STED laser. Excitation was provided by a white laser at 488 nm and fluorescence emission detected at 500–560 nm in a photon counting modality.

4.2.2 Cell culture

The measurement were done on the estrogen receptor-α (ER): a stable HeLa cell line with a hundred-copy integration of the estrogen-responsive unit of the prolactin gene (87), which stably expresses a GFP-tagged version of ER (GFP-ERα:PRL-HeLa cell line), was used (78). The GFP-ERα:PRL-HeLa cell line (Sheila) was grown in high-glucose DMEM without phenol red supplemented with 5% charcoal dextran stripped Tet(-)FBS, 200ug/ml Hygromycin B and 0.8 ug/ml Blasticidin S (Thermo Fisher Scientific, Waltham, MA, US) and 1 nM Z-4-Hydroxytamoxifen (Sigma Aldrich, Saint-Louis, MI, US). The day before the experiment, freshly split cells were plated on 8-well chamber (glass bottom, thickness 170±5 µm) (Ibidi, Planegg, DE) and grown overnight.

4.2.3 Treatments

The Sheila cells were treated with 10nM 17-β-estradiol (E2, Sigma Aldrich, Saint-Louis, MI, US) or with the antagonist ICI 182,780 (ICI) at 10nM concentration, both diluted in Live Cell Imaging Solution (Thermo Fisher Scientific, Waltham, MA, US) for one hour to trigger the GFP-ER binding to the array, and then imaged directly in the same incubation solution.

4.2.4 Experiments

The measurements were performed by scanning a 128 pixel line of 5.12µm through the cells nuclei, chosen in a way to cross the array. The 488nm laser power was set at 1.5µW, while the line time was set to 0.125ms (using the resonant scanner option at the line frequency f=8000Hz). Before the measurement, the array underwent a step of pre-bleaching, using the

maximum available power of 488 and 592nm laser lines, for 1min in an area of 2.5 μm^2. For each measurement, 4 million of lines were collected, and the whole measurement stack was divided into segment with duration T_{seg}= 10s each.

4.2.5 Data Analysis and Fitting

The whole measurement stack was analyzed by a custom Matlab routine and divided into 10s long segments. Intensity sorting was performed by averaging all the ACFs of segments whose intensity (calculated as the sum of the photon counting of the pixels contained in each column of the segment) was below and/or above specific threshold values. The sorted ACFs were fitted using a two-component diffusion model (Eq. 11).

4.3 Results

The diffusion of the ER inside and outside the prolactin engineered gene array (Fig. 4.3.1 a) was measured under E2 treatment with the Intensity Sorted FCS technique in a Line Scan implementation. In this measurement, performed on 10 different cells, the values of D for the slow (D_{slow}=0.03 $\mu m^2/s$) and the fast diffusing component (D_{fast}=1.05 $\mu m^2/s$) were in keeping with the results reported in Section 3.4.4. Basing on the selection masks defined on the Intensity Image (Fig. 4.3.1 b), the ACFs were efficiently sorted into two populations (4.3.1 c) and fitted using a two-component diffusion model. For each cell, the slow fraction (SF), calculated as SF= $G_{0slow}/(G_{0slow}+G_{0fast})$, inside ($SF_{array}$) and outside ($SF_{np}$) the array was plotted (Fig. 4.3.1 d). The results show that the slow diffusing fraction was significantly higher in the array compared to the nucleoplasm, with a slope= 0.69, in keeping with the results obtained with the slow scanning modality (Chapter 3.4.4).

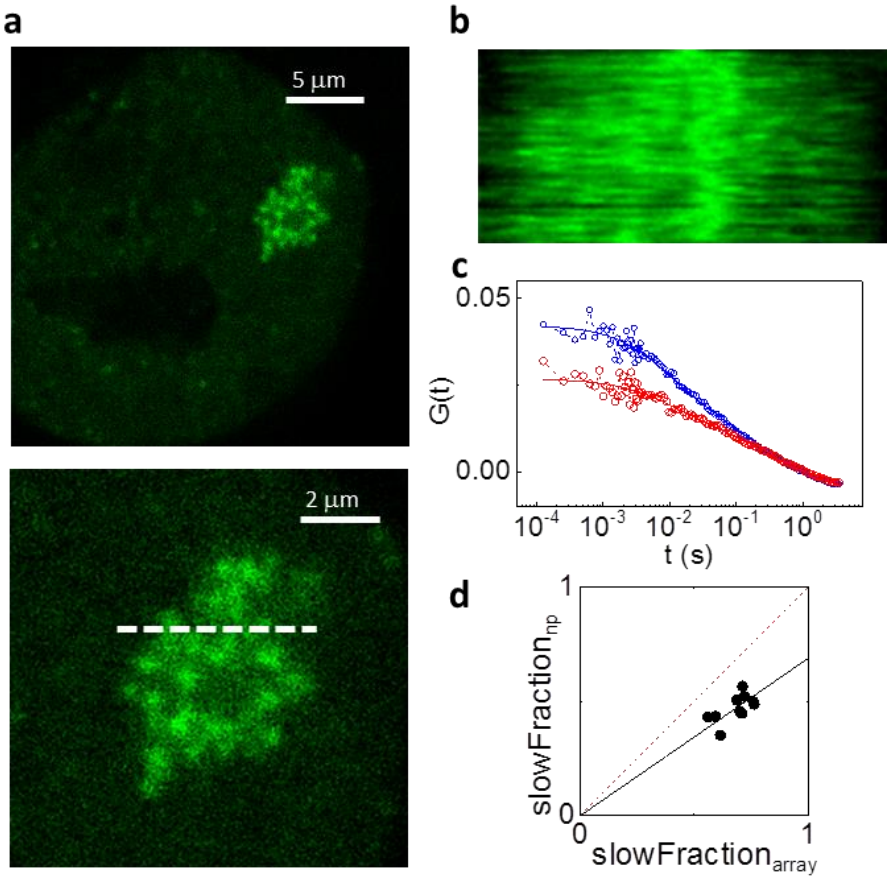

Fig. 4.3.1 Application of the Line Scan Intensity Sorted FCS technique in the measurement of ER diffusion. The diffusion of the ER-GFP was measured inside and outside the prolactin gene array (a). The intensity of the GFP-ER signal is used to create an Intensity Image (b) in which each line corresponds to the maximum projection of a segment of the original measurement. The Intensity Image is then used as a reference for sorting the ACFs corresponding to the array (red) and to the nucleoplasm (blue). (c) Analysis with the two-diffusion component model: a global fit performed on the sorted ACFs (red: sorted ACF of the array, blue: sorted ACF of the nucleoplasm) yields a shared value of diffusion coefficients D_{slow}=0.03 µm²/s for the slow diffusing population and D_{fast}=1.05 µm²/s for the fast diffusing one. (d) Scatter plot of the slow fraction calculated in the two probed nuclear regions (slope = 0.69).

Then, the technique was used to investigate how the treatment with a different hormone, namely ICI, affects the diffusion of the ER. In this experiment, a set of 10 measurements performed on cells treated with E2 is used as a control and compared to the diffusion coefficients and the relatively slow fractions measured on 10 different cells treated with ICI (Fig. 4.3.2). The control measurements showed values of D for the slow (D_{slow}=0.04 µm²/s) and the fast diffusing component (D_{fast}=1.11 µm²/s) in keeping with the other results obtained with E2 treatment. In

addition, also the plot of the SF showed similar results (SF_{array}/SF_{np}= 0.7 ± 0.01, mean ± s.d. of the slope values from 2 independent experiments, Fig.4.3.2 d and Fig. 4.3.3 a).

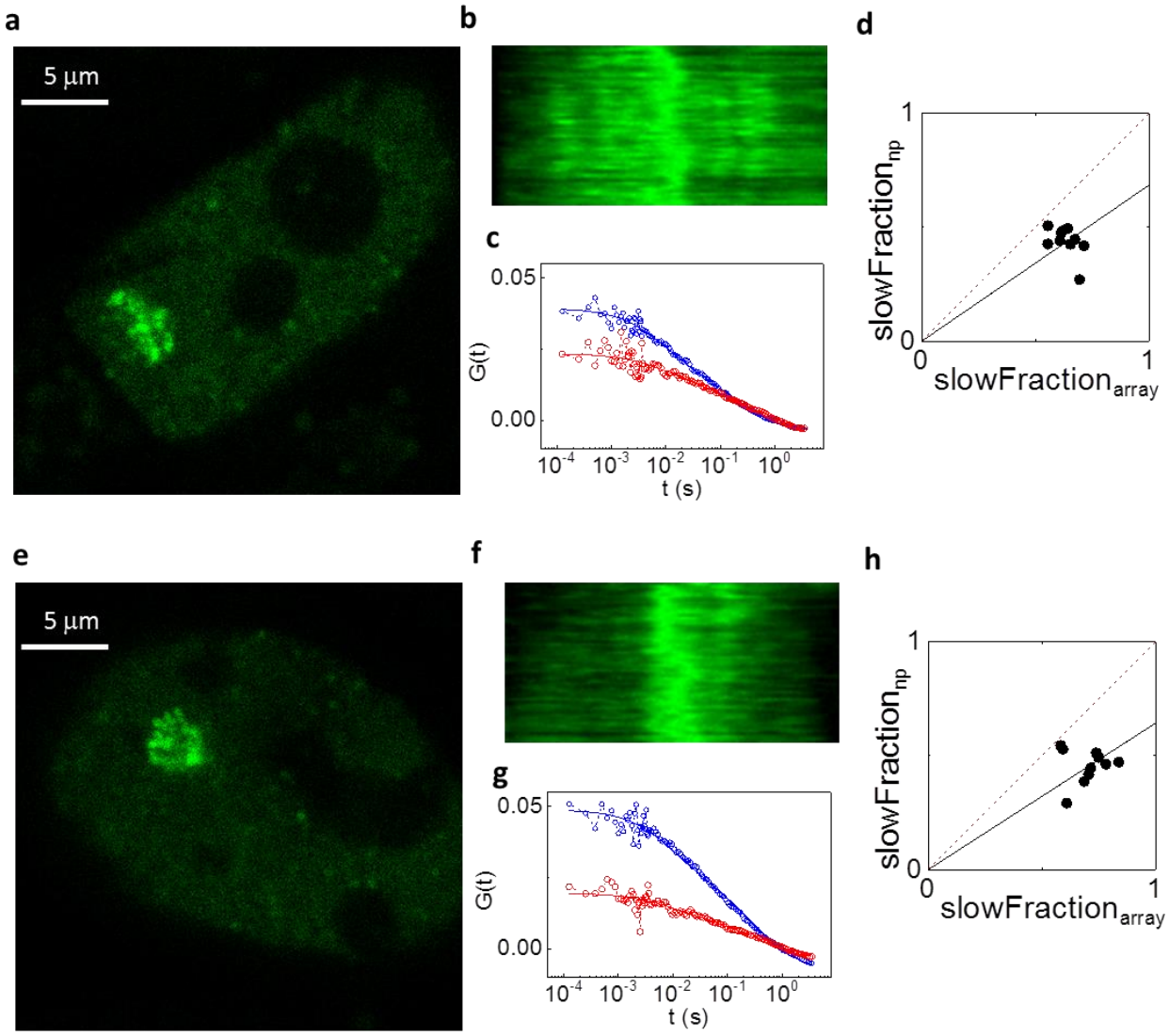

Fig. 4.3.2 Measurement of E2 diffusion coefficient in different nuclear compartments with different hormonal treatments. The diffusion of the ER-GFP inside and outside the prolactin gene array was measured under treatment with E2 (a) or ICI (e). The Intensity Image (b, f) are used as a reference for sorting the ACFs corresponding to the array (red) and to the nucleoplasm (blue). Analysis with the two-diffusion component model: a global fit performed on the sorted ACFs (red: sorted ACF of the array, blue: sorted ACF of the nucleoplasm) yields a shared value of diffusion coefficients D_{slow}=0.04 µm²/s and D_{fast}=1.11 µm²/s for the controls (c) and D_{slow}=0.03 µm²/s and D_{fast}=1.07 µm²/s for the cells treated with ICI (g). The scatter plot of the slow fraction calculated in the two probed nuclear regions seems to show the same fit value for the ICI treatment (h) (slope= 0.64), than for the controls (d) (slope= 0.69).

When the cells were treated with ICI (4.3.2 e), the global fit performed on the sorted ACFs with the two-component diffusion model (4.3.2 g) gave diffusion coefficients similar to those obtained in the controls (D_{slow}=0.03 μm^2/s and D_{fast}=1.07 μm^2/s). The plot of the slow fraction calculated in the two regions showed a ratio SF_{array}/SF_{np}= 0.7 ± 0.06 (mean ± s.d. of the slope values from 2 independent experiments, Fig.4.3.2 h and Fig. 4.3.3 b): the value of the slope is the same for cells treated with E2 and ICI. More experiments are needed in order to augment the statistics and get a more informative result.

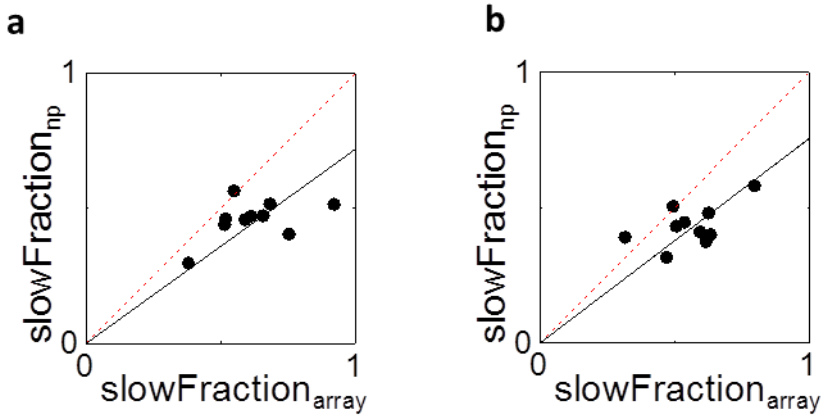

Fig. 4.3.3 Repetition of measurements done on the mobility of the Estrogen Receptor inside (x-axis) and outside (y-axis) the array of prolactin genes, upon treatment with E2 and ICI. The measurements are performed on 10 cells plotting the slow fraction calculated in both the array and the nucleoplasm. The cells were treated with E2 (a, slope 0.72), and the two diffusion coefficients retrieved are 1.21 μm^2/s and 0.04 μm^2/s., and with ICI (b, slope 0.76), with diffusion coefficients of 1.03 μm^2/s and 0.05 μm^2/s.

4.4 Discussion

In this chapter, an extension of the Intensity Sorted FCS method for commercial setups was presented. This Intensity Sorted FCS method is based on a classical Line Scanning FCS experiment, with some post-processing modifications. In fact, the whole intensity carpet resulting from a Scanning FCS measurement is segmented into N_{seg} smaller pseudo images of dimensions $N_{pxl} \times L_{seg}$, and for each smaller pseudo-image an ACF for each pixel is calculated. Then the ACFs were sorted basing on user-defined Intensity Masks, calculated on an Intensity Image in which each pixel corresponds to the sum of all the photon counts detected during one segment. This method maintains the important characteristics of the slow-scan implementation of Intensity Sorted FCS, such as the single-cell sensitivity, the statistical robustness and the ability to probe

different nuclear region without the constrain of having them immobile during the measurement. One notable difference is the lower temporal resolution (in this case, using the Resonant Scanner option with a frequency of 8000Hz, limited to 0.125ms): although in the study of interacting proteins, such as the ER, the temporal resolution needed is substantially lower (with a diffusion coefficient ranging between ≈ 0.01 and ≈ 3 $\mu m^2/s$), the Line Scanning method wouldn't probably be effective in measuring variation in small inert probes diffusion.

Application of the Intensity Sorted FCS approach to scanning FCS data acquired on a commercial laser-scanning microscope, was able to quantify mobility in different nuclear regions based on an intensity reference, as shown by the study of the Estrogen Receptor diffusion. The results obtained with this method are in keeping with those obtained with the slow scan implementation, showing the same ability in discriminating between the array and the nucleoplasm, and in retrieving diffusion coefficients and protein concentrations in the two regions. In addition, the Line Scan implementation of Intensity Sorted FCS was used to study if, and how, the triggering of the ER with a different hormone affects its nuclear mobility. The results showed that the retrieved values of diffusion coefficients, as also the slow moving fraction of the protein on the array, were the same. This could mean that ICI, being an ER antagonist, does not act on the ER gene targeting and mobility, but maybe on its transcriptional activity. More experiments are needed in order to confirm this theory, and additional data analysis, such as the fit with the FM model, can shed light on the modalities ICI uses to stall ER activity. In addition, the effect of other hormones on ER mobility can be tested and efficiently studied with this new technique.

5. Super-resolution

In this chapter, the concept of super-resolution, and in particular of Stimulated Emission Depletion (STED) technique, will be introduced. Then, the application of STED in FCS in living cells, as well as its combination with the intensity-sorting method presented before, will be illustrated.

5.1 STimulated Emission Depletion microscopy

As said before, any optical microscope is limited in its resolution by the diffraction of light. The resolution limitations are often referred to as the "diffraction barrier" or "diffraction limit" (88), which restricts the ability of optical instruments to distinguish between two objects separated on the lateral plane by a distance less than approximately half the wavelength of the light used to image the specimen (Eq. 3). This limit was majestically crumbled by the so-called **super resolution techniques**, whose inventors were granted with the 2014 Nobel Prize in Chemistry. Super-resolution techniques can be divided in three principal categories: **single molecule localization microscopy** (SMLM), **structured illumination techniques** and RESOLFT (**REversible Saturable Optical Linear Fluorescence Transitions**) like techniques (89). Among the latter, the most known and used is the **Stimulated Emission Depletion**, or **STED**, firstly introduced by the Nobel Prize Prof. Stefan Hell in 1994 (90).

STED microscopy can be considered an update of confocal scanning microscopy. In a scanning confocal microscope, as introduced before, the lateral resolution is determined by the spatial extent of the fluorescing area, which in turn is equal to the excitation area. The idea at the basis of STED microscopy is that any process that inhibits the fluorescence in the periphery and confines the fluorescence to the inner region of the excitation PSF leads to a smaller fluorescing area and therefore enhances the resolution. In a typical STED optical setup, an additional beam is superimposed to the excitation one (usually both pulsed): this **STED beam** is doughnut-shaped thanks to a vortex phase plate, an optical element having a phase singularity at his center creating destructive interference.

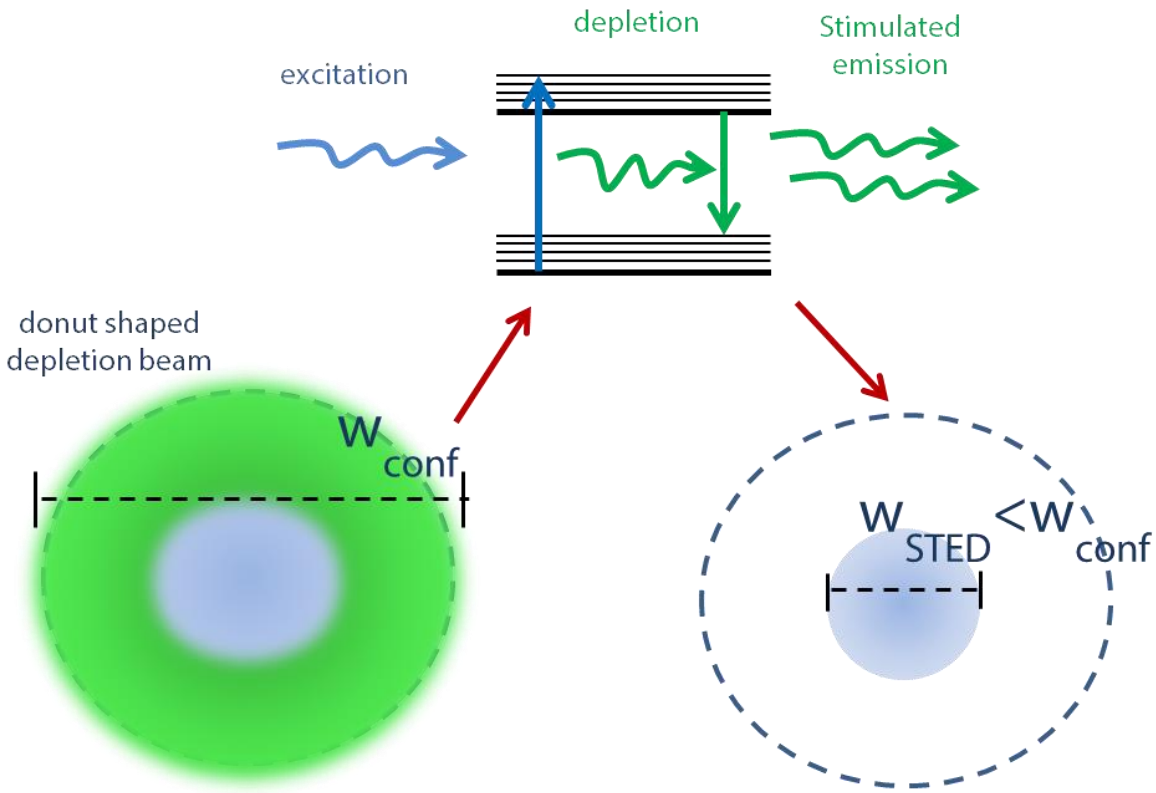

Fig. 5.1.1 Schematic representation of the STED concept. The schematic shows how the doughnut-shaped STED beam is superimposed to a confocal excitation spot: in the periphery of the spot, where the STED beam has its maximum intensity, the phenomenon of stimulated emission occurs, leading to a reduction in the observation volume due to the undetected different wavelength emission of the molecules undergoing stimulated emission.

This technique, as its name suggests, is based on the process of stimulated emission: an incoming photon of a specific wavelength can interact with an excited atomic electron (in this context, belonging to the fluorescent molecule), causing it to drop to a lower energy level (Fig. 5.1.1). The liberated energy transfers to the electromagnetic field, creating a new photon with a phase, frequency and polarization that are all identical to the photons of the incident wave.

In STED microscopy, the additional STED beam is superimposed to the excitation beam in order to force excited molecules to emit *via* stimulated emission, before they can fluoresce. The emitted photon is not detected as fluorescence signal, since depletion wavelength is chosen on the red part of the emission spectrum (longer wavelengths). The resolution achieved by STED is strongly dependent on the intensity of the STED beam, through the formula:

$$d_{STED} = \frac{\lambda}{2NA} \frac{1}{\sqrt{1+\frac{I}{I_{SAT}}}} \qquad \textbf{Eq. 13}$$

where I is the intensity of the stimulated emission laser and I_{SAT} is the **saturation intensity**, or the intensity at which the resolution is improved by a factor $\sqrt{2}$.

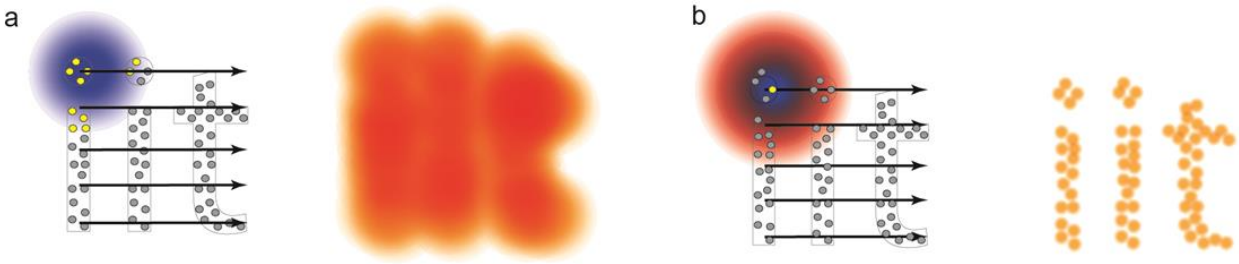

Fig. 5.1.2 Graphical representation of the principle of operation of STED microscopy. In conventional confocal scanning microscopy (a) all the fluorescent molecules excited by the light probe (excitation beam) are allowed to fluoresce and contribute to the signal recorded by the detector. Conversely, in STED microscopy (b), the additional doughnut-shaped beam can inhibit fluorescence at the periphery of the excitation beam, narrowing the effective PSF and subsequently increasing the resolution achieved.

Three practical conditions are necessary to achieve a consistent resolution improvement: the **spatial condition** (the excitation and STED beams need to be accurately co-aligned, in order to have the maximum of the excitation beams coinciding with the zero-intensity point of the depletion beam); the **temporal condition** (the depletion can occur only if the molecules the STED beam interact with are in the excited state S1: thus, the two beams should be carefully synchronized in a way that the STED pulse should be sent a few picoseconds after the excitation beam pulse); the **spectral condition** (the STED beam should only induce the stimulated emission and not excite the fluorophores. Since the absorption and emission spectra of fluorophores are partially superimposed, to fulfill this condition the STED beam wavelength is shifted toward the red tail of the emission spectrum, reducing also the emission cross-section, and consequently the STED beam efficiency: high STED power are thus required for achieving a significant improvement in resolution). Anyway, there are limitations imposed by the photobleaching and the subsequent photodamage of the sample for higher irradiated energy. On the other hand, an important property of STED microscopy is its compatibility with "conventional" fluorescence microscopy either in terms of instrumentation (a STED microscope is a confocal laser scanning microscope with an additional laser line) or in terms of dyes (fluorescent tags). An advantage of STED microscopy,

with respect to the stochastic super resolution techniques, is that this increase of resolution (Fig. 5.1.2) can be completely obtained with optics without the need of additional image processing (91).

Recently, several strategies based on the use of temporal information, have been exploited to implement STED at reduced peak powers. In these techniques, the STED architecture is the same of a canonical STED setup, apart from two important differences: the depletion laser works in a continuous mode, and for having a time-resolved experiment, a Time Correlated Single Photon Counting (TCSPC) module is connected to the detector. The techniques thus exploit the fact that the lifetime of the fluorophores is changed by the depletion beam, i.e. the average time they stay in the excited state is shortened, reaching a minimum in correspondence of the peaks of the doughnut-shaped STED beam, i.e. in the periphery of the observation volume. In this way, the STED laser imposes a spatial signature for the excited-state lifetime of the fluorophores within the excitation spot (Fig. 5.1.4): it is thus possible to map the lifetime of the fluorophores in space, and by recording the arrival time of each photons, arbitrarily decide which one to keep and which one to discard in order to shrink the observation volume. Two techniques have been described so far that use this time information to improve spatial resolution: they are the gated-STED (g-STED) and Separation of Photons by LIfetime Tuning (SPLIT-STED). The difference between them is the way they exploit the time information in order to reduce the effective excitation volume, with respective advantages and disadvantages that leads to the choice of the SPLIT-STED method in further super-resolved FCS experiments.

In **g-STED**, the early photons (most probably coming from the periphery of the observation volume), are discarded thanks to a temporal window set in recording (time gating, or T_g). In this way, only photons arriving after the temporal gate T_g will be selected to produce the final image (92, 93).

SPLIT-STED is based on the explicit separation of the position-dependent fluorophore dynamics (Fig. 5.1.4) generated in a continuous-wave (CW)-STED microscope (94).

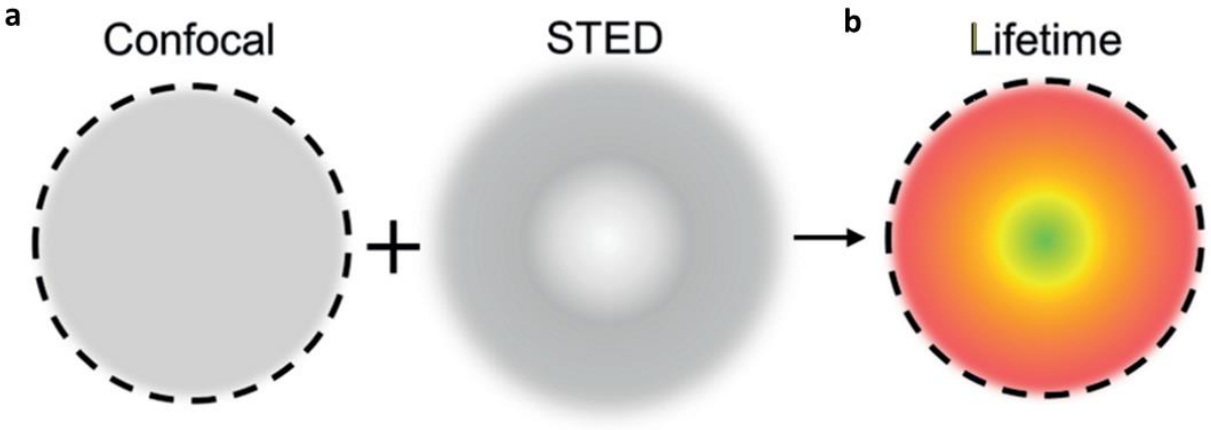

Fig. 5.1.4 Schematic representation of the spatial signature of excited-state lifetime imposed by the STED beam. The time-resolved STED methods are based on the change in lifetime of the fluorophores under the STED beam influence: in a confocal observation volume, the lifetime is the same at each position of the excited area (a). By superimposing a CW-STED beam, the lifetime inside the observation volume will change (b): there will be fluorophores with a faster decay (red) induced by the STED beam, and fluorophores with a slower/unaffected decay (green), belonging to the center of the observation volume. In this way, excited-state lifetime of a fluorophore changes according to its position (spatial signature).

The doughnut-shaped, CW-STED beam affects the fluorescence decay rate of each fluorophore in a measure proportional to the STED beam intensity. As a result, the fluorescence lifetime τ is a function of the position of the fluorophore within the observation volume, being maximum at the center, and decreasing towards the periphery (Fig. 5.1.4 a). The spatial variation of the lifetime can be described by:

$$\frac{1}{\tau} = \frac{1}{\tau_0}\left(1 + k_S \frac{r^2}{w_0^2}\right) \qquad \textbf{Eq. 14}$$

where τ_0 is the unperturbed excited-state lifetime of the fluorophore, r is the radial distance from the optical axis, w_0 is the waist of the Gaussian observation volume, or point spread function (PSF), of the confocal microscope, and k_S is a parameter that quantifies the relative variation of decay rate values within the observation volume. The parameter $k_S = \frac{I_{STED}(w_0)}{I_{SAT}}$ is the ratio between the value of the STED intensity at radial position $r = w_0$ and the saturation value I_{SAT} for which the probability of decay due to stimulated and spontaneous emission are equal. The precise

value of k_S depends on the optical configuration, i.e., the intensity distributions, and on the properties of the sample. The decay of the fluorescence intensity $J_{STED}(t)$ in the presence of the STED beam (STED decay) can be described by

$$J_{STED}(t) = I_0 e^{-\frac{1}{\tau_0}} \frac{1}{1+\frac{k_S}{2}\frac{t}{\tau_0}} + I_0 b \qquad \textbf{Eq. 15}$$

where b represents the fraction of uncorrelated background and I_0 the amplitude of the decay. It is possible to calculate the value of k_S for a given fluorophore, and a given STED intensity, by fitting the experimental decay curve with Eq. 15.

A distinctive feature of the SPLIT method, with respect to other time-resolved STED methods like g-STED, is the isolation of uncorrelated background (Fig. 5.1.5 c).

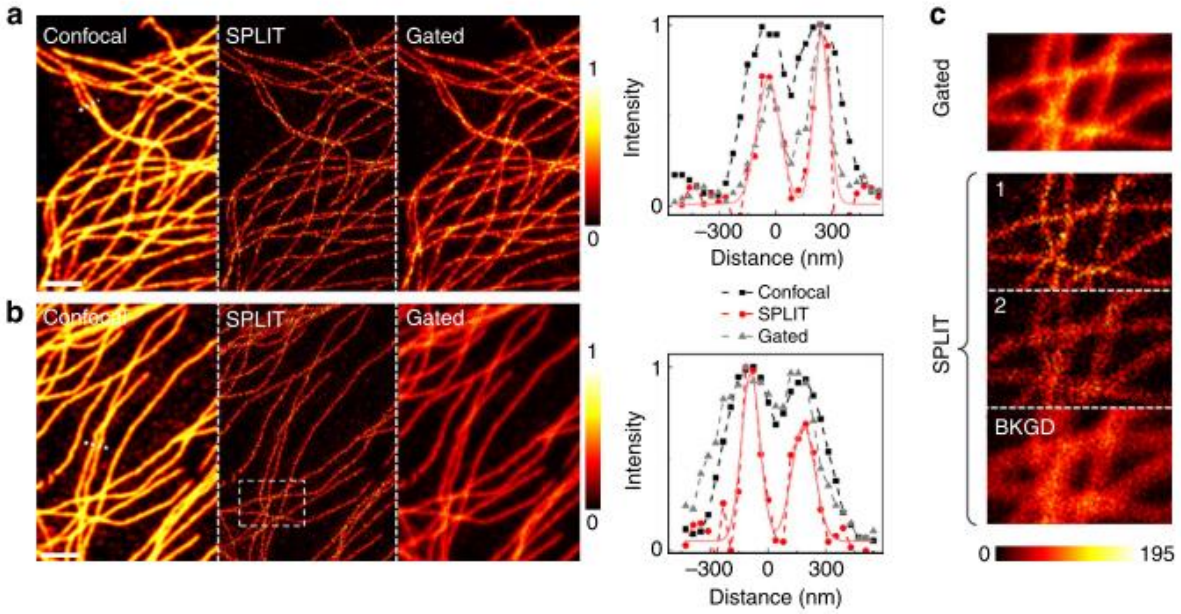

Fig. 5.1.5 Example of the application of the SPLIT method. Microtubules in fixed HeLa cells labelled with the organic dyes Alexa Fluor 488 (a) and Oregon Green 488 (b). The confocal image, the SPLIT image, the time-gated STED image (obtained with a STED beam power of 40mW) and the intensity profile along the dashed line are shown. The colourmap represents the fluorescence intensity normalized to the maximum value of each image. (c) The time-gated image is compared with the SPLIT for the region highlighted in b. In the SPLIT series, the image 1 represents the photons coming from the center of the excitation volume, while the image 2 is constructed using the photons belonging to the periphery of the observation volume. It is clear how the technique is able to effectively separate these two populations of

photons, as well as the uncorrelated background (BKGD in the figure). The colourmap represents the fluorescence intensity expressed in counts per 0.1 ms. Scale bars, 2μm. (94)

5.2 Toward STED-FCS in the nucleus

Recently the STED technique has been coupled to FCS, in order to study diffusion of molecules at a spatial scale well below the limit imposed by the diffraction of light (95, 96). In addition, thanks to the change of the intensity of the STED beam or to the analysis of fluorescence dynamics (gated STED-FCS) (97), the coupling of STED with FCS allows the probing of molecular mobility at a decreasing scale. By plotting the transit time t_D of a molecule through the observation volume as a function of the observation area it is possible to obtain an **FCS diffusion law**, useful for discriminating between different types of motion, for example free diffusion or diffusion confined by microdomains (24). However, STED-FCS has been mainly used for studies on membranes and to a much lower extent to study three-dimensional motion of particles in the interior of living cells. In fact, the main problem encountered when performing STED-FCS in 3D is a significant increase in unspecific background signal (i.e. signal that doesn't produce correlation) that damps the correlation amplitude and precludes accurate FCS measurements. The expected outcome of a STED-FCS experiment is that both the average transit time t_D of the molecules through the observation volume and the average number N of molecules in the observation volume decrease with an increasing STED beam intensity. However, for fluorophores diffusing freely in 3D in solution, only the expected decrease of t_D is observed, whereas N does not decrease accordingly. This issue has been ascribed to a reduced signal-to-background ratio caused by non-depleted, low-brightness fluorescence signal from out-of-focus volume shells.

Due to its intrinsic ability of discarding the non-correlated background (in the nanosecond temporal scale) from the analysis, SPLIT can be used in association with FCS, in order to reduce the observation volume in 3D, and attempt to overcome the above-mentioned specific issues. In order to do that, the technique has been upgraded thanks to the efficient filtering algorithm proposed for FLCS by the group of Enderlein.

FLCS is a method that uses time-resolved detection for separating the FCS contributions associated with different fluorescence lifetime components (81). FLCS is based on the application of weighting functions to the detected photon counts before calculation of the ACF. Assuming the presence of two different lifetime population (i.e. the slow decaying one, belonging to the center of the observation volume, not affected by the STED beam, and the fast decaying population,

whose lifetime is shortened by the interaction with the depletion beam), a filtered ACF associated with the slowest component, and thus to a smaller effective observation volume, can be obtained by properly weighting the photons based on their arrival time on the nanosecond temporal scale (Fig. 5.2.1 c, d). The uncorrelated background is included in the FLCS analysis as an additional decay pattern: in each experiment, the relative fraction of uncorrelated background with respect to the decaying fluorescence signal is quantified by the parameter b in Eq. 15, which can be determined experimentally. By considering the uncorrelated background as an additional fluorescence intensity decay, it is thus possible to isolate the uncorrelated background from the total signal.

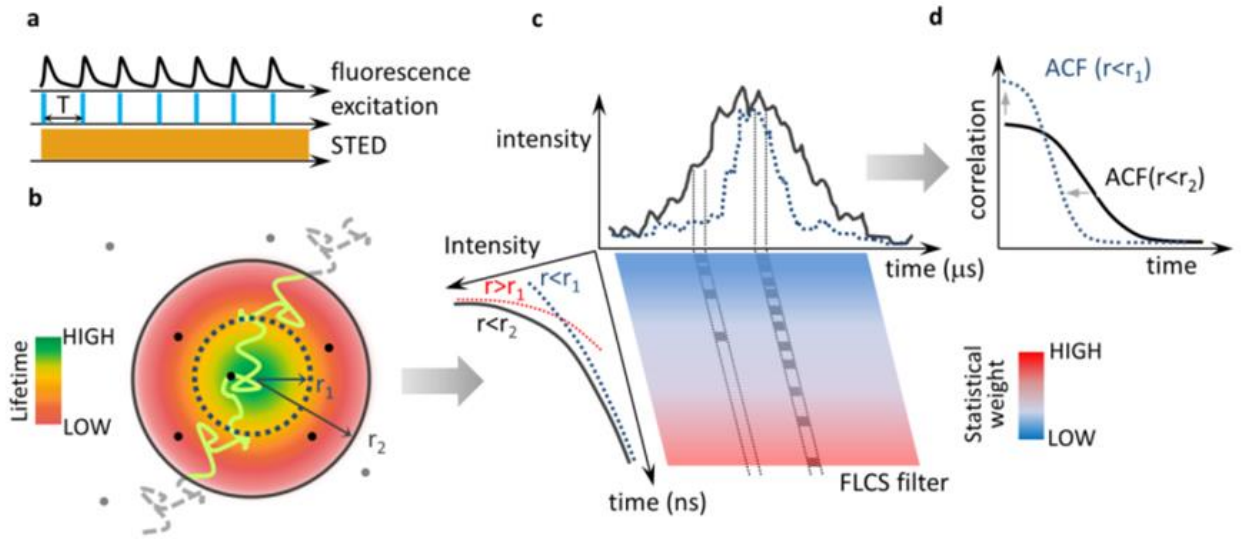

Fig. 5.2.1 Schematic representation of the SPLIT-FLCS concept. (a) While the STED beam is generated by a Continuous Wave laser line, the excitation is provided by a pulsed laser source to exploit the variations in the fluorescence dynamics observed in the nanosecond time scale (t < T). (b) The spatial variations of fluorescence lifetime within the effective observation volume of the microscope can be modeled as a gradient in the radial direction, with the lifetime value being the highest at the center and decreasing towards the periphery. A molecule transiting within the observation volume will emit photons with different fluorescence lifetime according to the radial position. (c) The temporal fingerprints associated to different spatial positions can be used to weight the photons based on their time of arrival in the nanosecond time scale. For instance, the decay associated to the region defined by the radial position $r < r_1$ can be used to generate a statistical filter that, by over-weighting the late-arriving photons, sort out only the intensity emitted from a smaller effective observation volume. (d) Correlation of the weighted photons on the time scale relevant for molecular diffusion (t > 1 µs >> T) results in a filtered ACF associated to fluctuations on

a smaller effective observation volume, namely an ACF which is narrower and has larger amplitude ($r < r_1$) (98).

5.3 Single-point STED-FCS: results

The SPLIT method is implemented on a STED microscopy configuration that uses pulsed excitation and a CW-STED beam (Fig. 3.3.1). The STED beam was generated by a CW optical pumped semiconductor laser (OPSL) emitting at 577 nm (Genesis CX STM-2000, Coherent, Santa Clara, CA, US), while the nanosecond temporal information was collected in a TCSPS file. The data were analyzed using a custom Matlab routine, while the fit was performed in Origin as previously described (Chapter 3.3).

A careful calibration of the effective observation volume is necessary before performing the measurements inside a living cell. This was done using EGFP in solution, whose diffusion coefficient is known (90 $\mu m^2/s$). Point-FCS was performed, using an additional STED beam at 50mW. The spatial variation of the lifetime was thus assessed by fitting the STED decay with Eq. 15, giving a variation of w_0 ranging from 139nm to 85nm (Fig. 5.3.1 a, b).

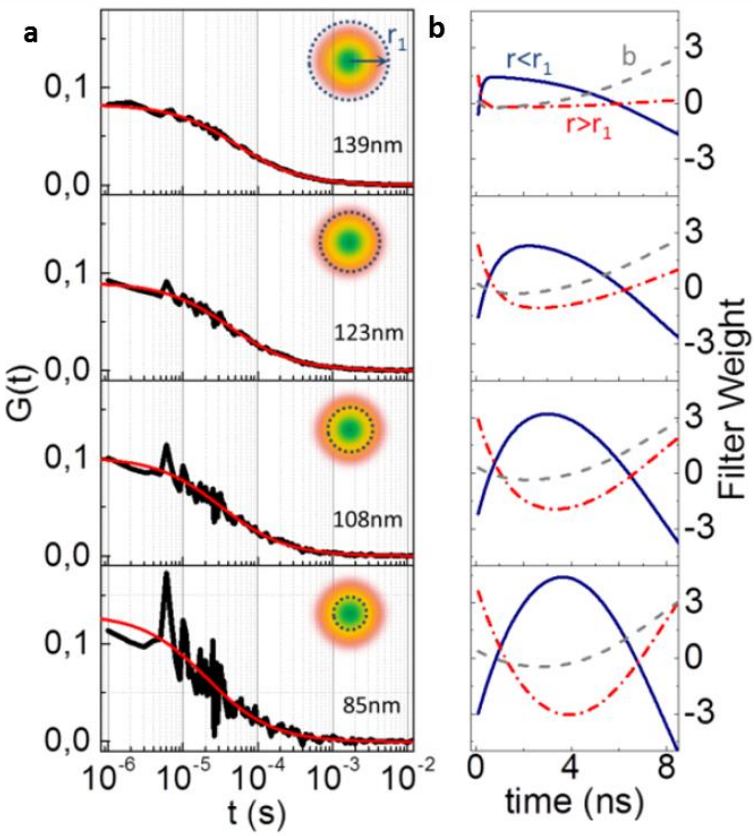

Fig. 5.3.1 SPLIT-FLCS performed on an EGFP solution. (a) Filtered ACFs of EGFP in PBS obtained at a STED power of 50mW for different values of the parameter r_1 (r_1 = $11\,w_0$, $2\,w_0$, w_0, $0.5\,w_0$, respectively, from top to bottom). Each of the ACFs is obtained from a FLCS-based separation into three components (b) and is associated to the calculated decay corresponding to the radial region $r < r_1$. Solid red lines are a fit of the data to Eq. 8 and the numbers indicate the recovered lateral size w of the effective observation volume. (b) Filter weighting functions corresponding to the temporal signatures of the fluorophores located at distance $r < r_1$ (solid blue line), the fluorophores located at distance $r > r_1$ (red dash-dot line), and the fraction b of uncorrelated background (gray dashed line), respectively.

Since the effective volume depends on the parameter r (Eq. 14) used in the post-processing, and not on a modulation in laser intensity, it is thus possible, using this method, to define different observation volumes in the same measurement. It is worthy to note that the effective resolution obtained using this technique depends uniquely on the signal-to-noise ratio, as it is clear by the increasing noise in the ACFs if going to smaller volumes. Thus, using brighter and more stable fluorophores, will lead to a significant enhancement in resolution, while keeping a lower STED laser intensity, that renders the method suitable to live cell measurements. After volume calibration in solution, the method was applied to measure untagged EGFP diffusion in the cytoplasm of living cells at different spatial scales. The filtered ACFs, obtained by decreasing the value of r, are characterized qualitatively by the same behavior observed for EGFP in solution, namely smaller width, larger amplitude, and lower signal-to-noise ratio (Fig. 5.3.2 a). Using the values of w obtained from the calibration with EGFP in solution one can retrieve the transit time t_D at different spatial scales (different area w^2) (Fig. 5.3.2 b).

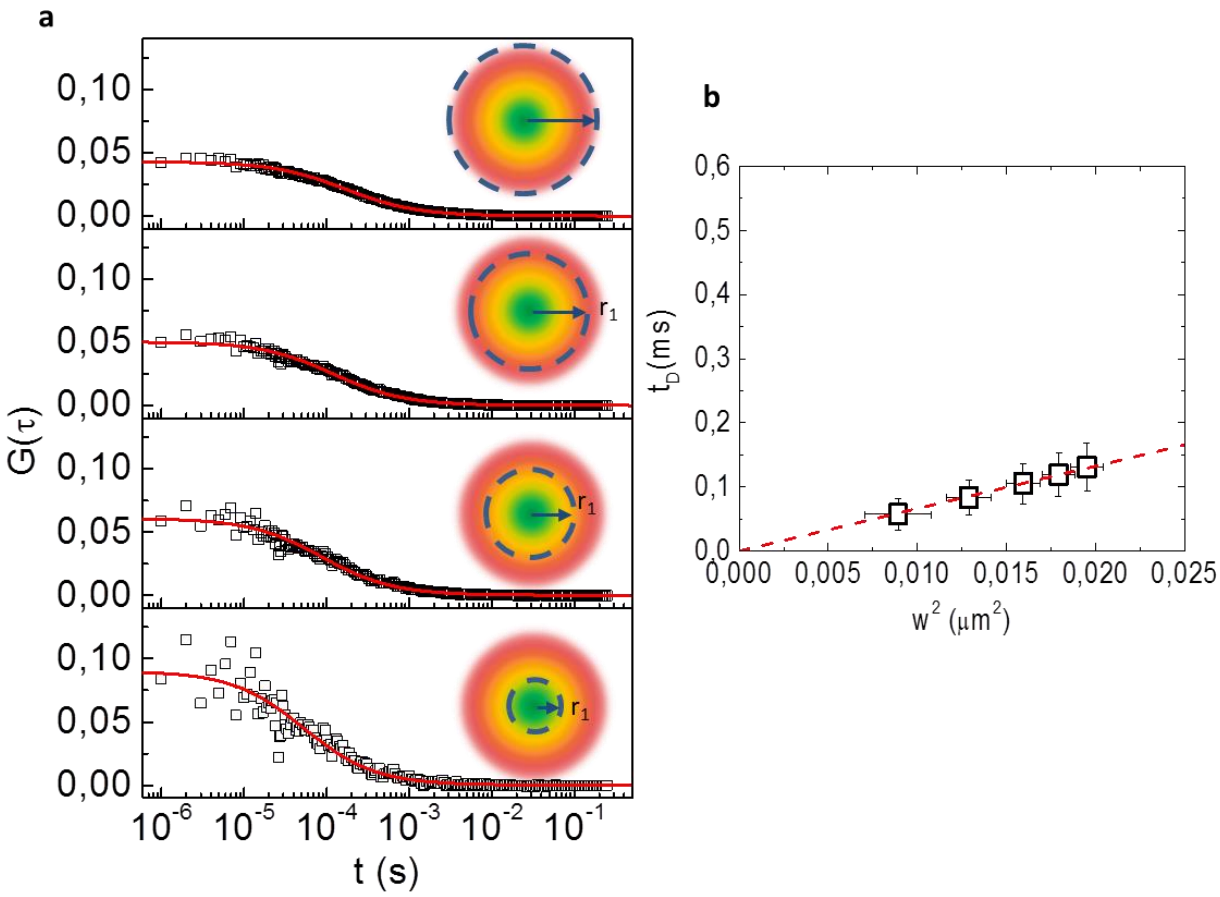

Fig. 5.3.2 Application of the SPLIT-FLCS method in the cytoplasm of living cells. (a) Representative filtered ACFs of EGFP in the cytoplasm of a HeLa cell at a STED power of 50mW for different values of the parameter r_1. Solid lines are a fit of the data to Eq. 8. (b) Transit time t_D for different spatial scales, (ranging from ≈140 to ≈80nm), obtained as the average of single-point measurements in the cytoplasm of n = 12 different HeLa cells (mean ± s.d.). The dashed line is a fit to Eq. 6 (D = 25 μm^2/s). (98)

The same measurement was also performed on a different cytoplasmic protein, namely tubulin, fused to EGFP. By plotting the diffusion law obtained from these measurements, it is possible to discriminate between free Brownian motion (EGFP in cytoplasm), and trapped motion (tubulin-EGFP), characterized by a positive intercept of the fit to Eq. 6 (Fig. 5.3.3).

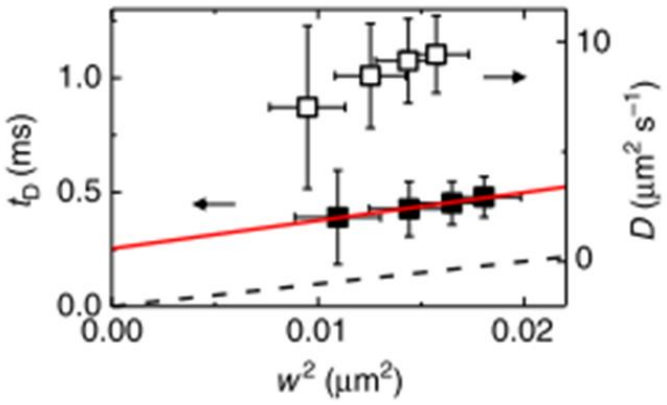

Fig. 5.3.3 Diffusion law retrieved for tubulin-EGFP in the cytoplasm of living cells. Transit time t_D (solid squares) and apparent diffusion coefficient D (open squares) for different spatial scales, obtained as the average of single-point measurements in the cytoplasm of HeLa cells (n = 32, mean ± s.d.). The solid red line is a linear fit to the data. The dashed line represents a Brownian motion with D = 25 μm^2/s. (98)

Single point SPLIT-FLCS was also performed on the nucleus of living HeLa cells, retrieving different diffusion laws for the two GFP-tagged proteins probed, namely HP1-α and PCNA (Proliferating Cell Nuclear Antigen), a protein deeply involved in DNA replication and repair.

HeLa WT cells were transfected with PCNA (AddGene, plasmid # 14822) and HP1-α fused to EGFP, and analyzed 24hours after transfection. Firstly, a calibration of the effective volumes was performed in a solution of EGFP in PBS. Then the STED measurement was performed on the nucleus of living transfected cells, with an excitation power of 7.5 μW and a STED power of 50mW.

For PCNA (Fig. 5.3.4 c), the volumes retrieved ranged from 132 to 91nm, while the filtered ACFs showed the same behavior of untagged-GFP ACFs (Fig. 5.3.4 a). The diffusion law calculated with the average transit time seem to deviate from Brownian diffusion (Fig. 5.3.4 b). This could mean that the PCNA dynamic is dominated by the binding, that is nearly unrelated to the waist size, rather than by Brownian diffusion through the observation volume. It is worthy to note that the error bars are large, maybe indicating a high heterogeneity in the measurements due to the different spatial points in which the data were acquired. In addition, it is possible that the bleaching of the immobile structures affected our results in a significant way: more measurements are necessary in order to confirm this diffusion law.

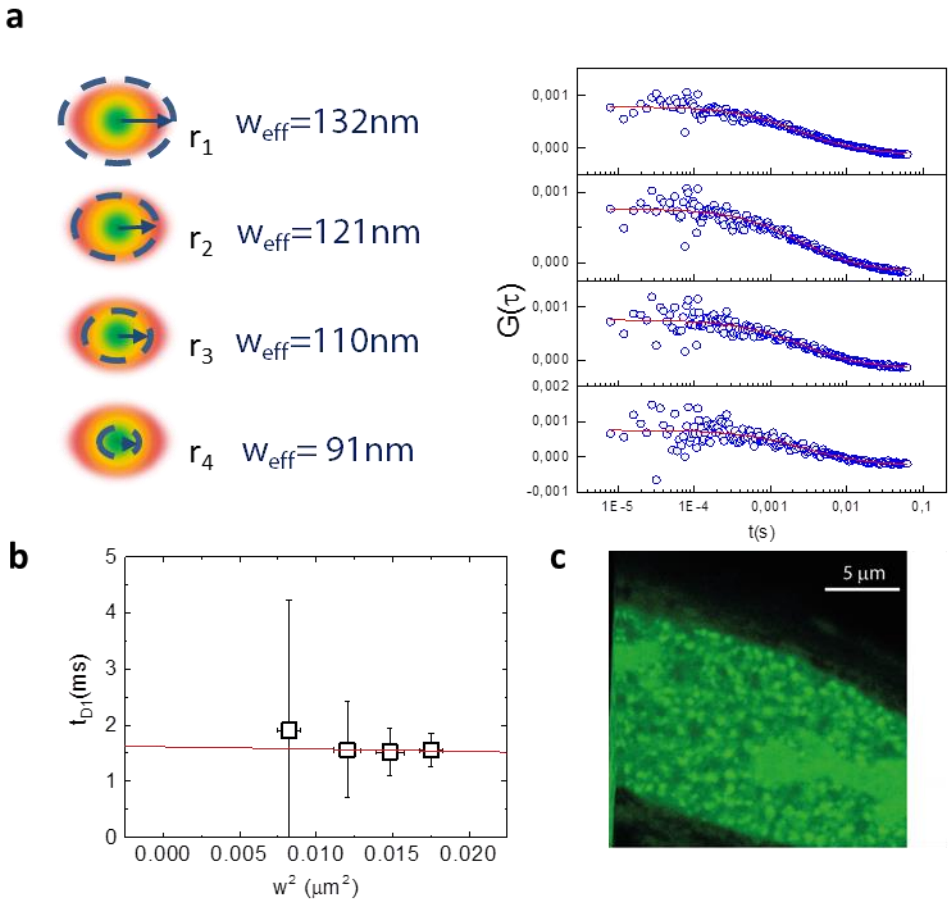

Fig. 5.3.4 Single-point SPLIT-FLCS in the nucleus of living HeLa cells transfected with PCNA-GFP. (a) Representative filtered ACFs of PCNA-GFP in the nucleus of a HeLa cell (c) at a STED power of 50mW for different values of the parameter r_1, leading to spatial scales ranging from 132 to 91nm. Solid lines are a fit of the data to Eq. 8. (b) Transit time t_D for different spatial scales, obtained as the average of single-point measurements in the cytoplasm of n = 15 different HeLa cells (mean ± s.d.). The solid line is a linear fit to the data.

For HP1-α (Fig. 5.3.5 c), the volumes retrieved ranged from 132 to 91nm, while the filtered ACFs showed the same behavior of untagged-GFP ACFs (Fig. 5.3.5 a). The diffusion law calculated with the average transit time also in this case suggests a deviation from a Brownian motion of the protein, suggesting a significant binding component (Fig. 5.3.5 b). As for PCNA measurements, the error bars showed the high heterogeneity in the data.

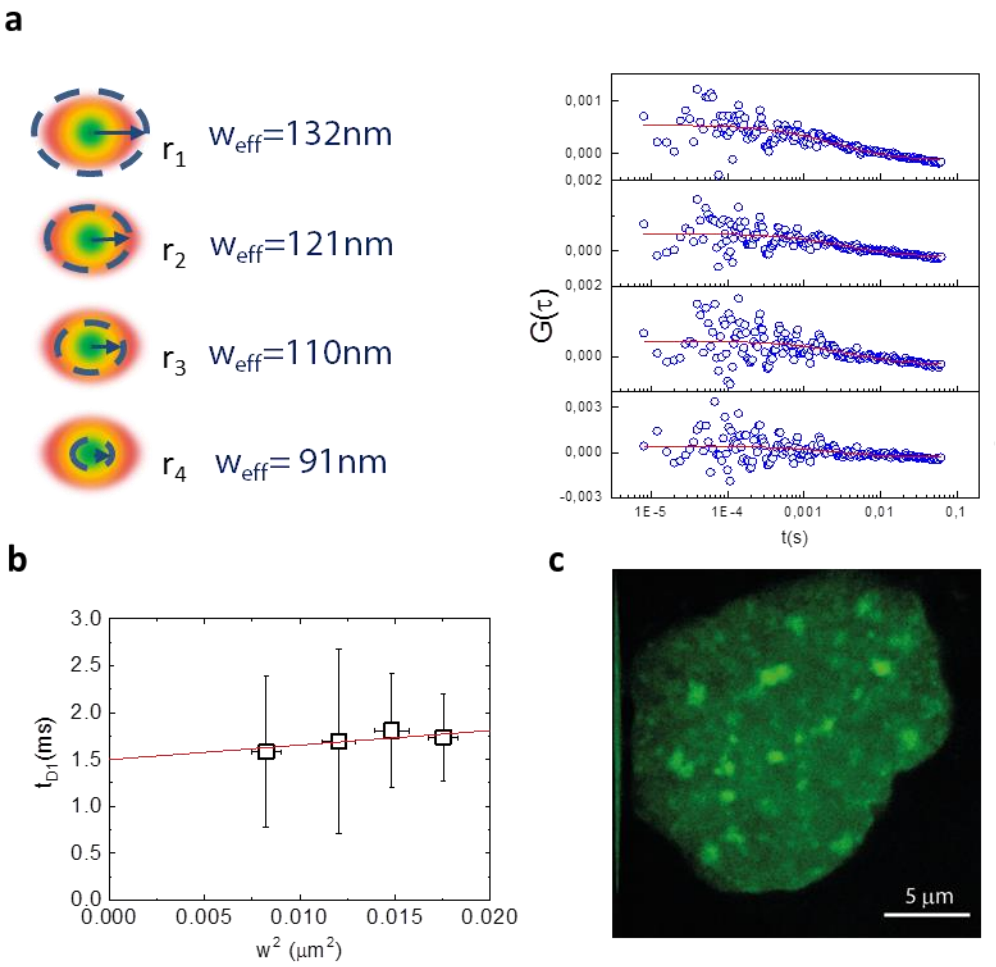

Fig. 5.3.5 Single-point SPLIT-FLCS in the nucleus of living HeLa cells transfected with HP1α-GFP. (a) Representative filtered ACFs of HP1-α fused to GFP in the nucleus of a HeLa cell (c) at a STED power of 50mW for different values of the parameter r_1, leading to spatial scales ranging from 132 to 91nm. Solid lines are a fit of the data to Eq. 8. (b) Transit time t_D for different spatial scales, obtained as the average of single-point measurements in the cytoplasm of n = 9 different HeLa cells (mean ± s.d.). The solid red line is a linear fit to the data.

To overcome the limitation deriving from the heterogeneity of the nuclear environment, Intensity Sorted FCS can be useful: upgrading it with the SPLIT technique, it will be possible to obtain different diffusion laws in different compartments, probably reducing the scatter of the data, and thus the errors associated to the average transit times.

5.4 Intensity Sorted STED-FCS

The innovative STED-FCS method reported above was thus combined with the Intensity Sorted technique described in Chapter 3, in order to collect diffusion laws in different nuclear

compartments. In order to test the ability of this method to efficiently retrieve diffusion laws in different nuclear compartments, within the same measurement, the data were acquired on simpler model, i.e. inert monomeric GFP diffusion in the nucleolus compared to the nucleoplasm.

For these measurements, the 488nm laser power was set to 15µW, while the STED beam intensity (577nm) was kept at 50mW: the measurements were performed with an orbit diameter of 3µm and a scan period of 16.7sec, while the whole measurement lasted 264s. For calibration of the effective detection volume, single-point STED-FCS was performed on a solution of purified AcGFP1 (Clontech, Mountain View, CA, US) in PBS (Fig. 5.4.1). The measurements on solution were performed at an excitation power of 22.5µW for a total acquisition time of 100s.

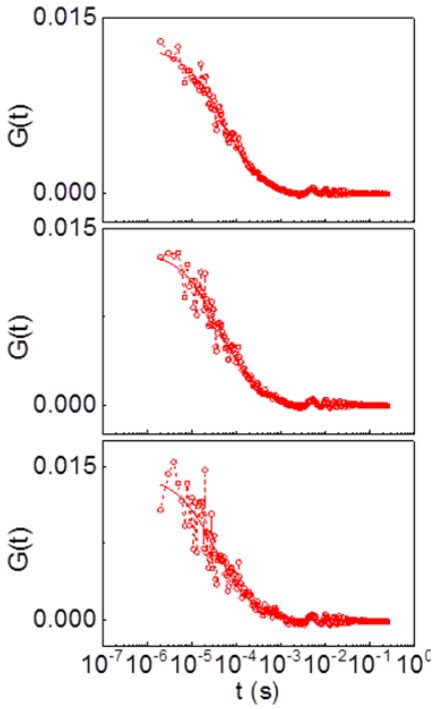

Fig. 5.4.1 Calibration of the detection volume in a GFP solution. The diffusion coefficient of GFP in solution is fixed to 90 $\mu m^2/s$, and the fit is performed in order to retrieve the effective volumes for each mathematical filter used in the analysis. The ACFs are calculated using, from top to bottom, increasingly smaller number of photons: the fit gives a value of the effective volume size of 137, 126 and 114 nm, from top to bottom.

The experiments were done in HeLa cells, orbiting across the nucleolus and using as a reference the GFP intensity level (Fig. 5.4.2 a, b). The GFP lifetime variations induced by the STED laser beam were used to filter the detected photons, identifying in this way three different effective volumes in the same measurement. The sorting of the data generated, for each cell, two sets of

ACFs, corresponding to the nucleoplasm (Fig, 5.4.2 c) and the nucleolus (Fig, 5.4.2 d). This corresponds to a separate spot-variation analysis for each compartment, shown as the average diffusion coefficient versus the square size of the effective observation volume (Fig. 5.4.2 e). At smaller spatial scales, we observed a slight increase of the diffusion coefficient, especially in the nucleolus, but also a much larger error bar.

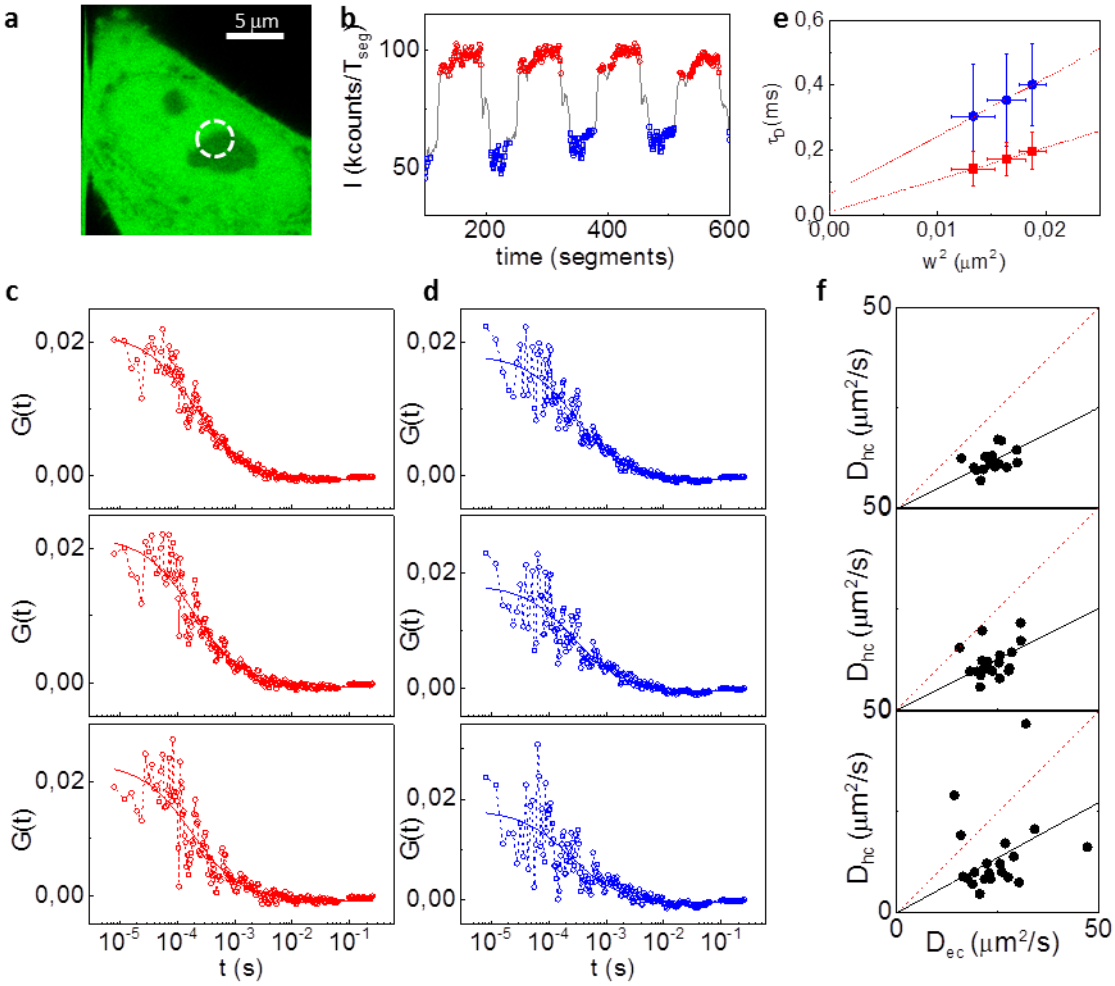

Fig. 5.4.2 Intensity-sorted STED-FCS in the nucleus. Each measurement is performed on an individual cell, scanning the beams across the nucleoli (a). (b) GFP intensity trace used for sorting the ACFs between the nucleolus (in blue) and the nucleoplasm (red). Three different volumes are selected in the post-processing, with size w=137, 126 and 114 nm respectively. (c, d) ACFs corresponding to detection volumes of decreasing size (from top to bottom) along with the fit, for the nucleoplasm (D_{np}=30; 32; 35 µm²/s from top to bottom) (c) and the nucleolus (D_{nl}=22; 23; 26 µm²/s from top to bottom) (d). (e) Average diffusion coefficient versus the square size of effective volume, for GFP in the nucleoplasm (red) and in the nucleolus (blue) (data represent mean ± s.d. of n=20 measurements on different cells). (f) Scatter plot of the diffusion coefficients measured in the two regions for each effective detection volume, together with the corresponding linear fit (slopes=0.48; 0.5; 0.55 from top to bottom).

This is probably due not only to cell-to-cell variability but also to the fact that reducing the size of the effective detection volume (w_{eff} = 137, 126 and 114 nm, from top to bottom) results in ACFs with a poorer signal-to-noise ratio (Fig, 5.4.2 c, d). We tested if the ratio between the diffusion coefficient in the nucleolus versus nucleoplasm was also preserved at different subdiffraction spatial scales, on a cell-by-cell basis (Fig. 5.4.2 f). The results are in keeping with those obtained with confocal intensity-sorted FCS (Fig.3.4.1.1), despite a higher scattering of the diffusion coefficients values that are probably ascribed to the SNR reduction of the ACFs at the smallest effective observation volumes.

Taken together, these results show the compatibility of our approach with STED and that, in principle, intensity-sorted STED-FCS could be a useful tool to measure mobility in different nuclear regions at multiple sub-diffraction spatial scales. Note that the high temporal resolution allows an optimal temporal sampling of the ACF even if the average transit time measured in the nucleoplasm at the smaller effective observation volume is in the order of 100 μs. The major limitation we encountered was related to the poor quality of the ACFs at smaller observation volumes. This aspect could be improved by using probes which are brighter and/or more photostable than GFP, for example using the genetically-encoded Halo- or SNAP- tags, that allow the use of brighter, more stable organic dyes. The increase in the number of photons collected could facilitate pushing the spot-variation analysis towards smaller spatial scales.

Finally, it is worth noting that STED, by providing intensity features that are better resolved spatially, should also improve the sorting of the data. In our test system, i.e. nucleolus vs nucleoplasm, we did not exploit this advantage as the two regions extend over several micrometers and are easily distinguished with normal resolution.

6. Conclusions

The aim of this thesis work was to establish an FCS method able to discriminate between nuclear regions and to retrieve diffusion information relative to these nuclear compartments.

The nuclear environment is highly heterogeneous and dynamic, and the principal issue about dynamic measurements in this organelle is due to the relatively rapid movement of its spatial features, for example the chromatin itself.

To overcome this issue, a novel FCS method was presented, namely Intensity Sorted FCS. This method is based on a slow scanning of the excitation volume, and on the division of the whole measurement into segments. Each segment, which corresponds to a short single point FCS acquisition, is then sorted into different populations basing on the intensity of a reference channel, which provides the spatial information. This intensity is thus a fingerprint of each segment, and allows to track the spatial features of the nucleus, even if they are moving during the measurement. In addition, given an intensity threshold that define the two populations (each corresponding to a region of high or low intensity), the ACFs calculated on each sorted segment, and thus corresponding to a given nuclear region, are averaged, assuring a proper statistical robustness.

The advantages of this method are, apart from the high temporal resolution, which allows to appreciate differences in diffusion even of a small inert probe, the single-cell sensitivity and the intrinsic intensity fingerprint of the probed compartments.

The application of the method on monomeric untagged GFP showed its applicability to measurements done on such small inert probes, being able to highlight differences in its mobility due to chromatin different compaction. In fact, by using Intensity Sorted FCS on the nucleus of HeLa cells expressing free monomeric GFP, it was possible to see a difference in its diffusion coefficient in euchromatin and heterochromatin. These two regions were differentiated based on the intensity of a Hoechst stain: the higher the Hoechst intensity, the higher the DNA content, thus defining the heterochromatin compartment. Moreover, the method showed its sensitivity in measuring differences in diffusion coefficients calculated in cells treated with solutions known to change chromatin compaction.

To extend the application possibilities, Intensity Sorted FCS was used to study nuclear mobility of different proteins known to interact with chromatin or nuclear structures. Also in this case, the results showed the ability of the method to discriminate between different nuclear regions (for example between protein foci and the nucleoplasm), even if not all the proteins behave in the same way in the compartments studied. An interesting application of the method was on the Estrogen Receptor, in cells expressing a prolactin gene array, where the ER proteins accumulate under hormone treatment. In this case, the results opened several possibilities in the study of this nuclear receptor dynamic and function, as highlighted by the use of different fit models.

All the Intensity Sorted FCS measurements were performed on a custom setup. The next step was to render this method available, at least in part, on commercial setups. For this reason, Intensity Sorted FCS was extended also to data acquired on a commercial LSM. This second approach is based on the scanning of the beams in a single line, repeated over time. The differences from a classical line-scan

FCS experiment are only in the analysis: as for the Intensity Sorted FCS, the whole measurement is divided into segments. Each segment (the column of a small pseudo-image) is used to calculate the ACFs and then, from the total photon counting of each segment, to create an Intensity Image on which two Intensity Selection Masks are built, basing on an user-defined threshold value. Each ACF is then sorted into the population corresponding to the high or low intensity mask. The method maintains the characteristics of the Intensity Sorted FCS technique, apart from the temporal resolution, that is limited in the range of milliseconds due to the mechanical scanning of the beams.

Intensity Sorted FCS on a commercial Leica Sp5 LSM was successfully applied to the ER mobility study, giving results comparable to the ones obtained by Intensity Sorted FCS. In addition, in a project in collaboration with the Baylor College of Medicine in Houston, ER diffusion was studied under different hormonal treatments, showing the versatility of the method.

Finally, in order to perform nuclear measurements at different sub-diffraction spatial scales, the concept of super-resolution measurements was introduced. STED is a super-resolution technique indicated for dynamic measurements. The exploitation of the novel method that couples STED with FLCS gave important results in the study of cytoplasmic diffusion and in the retrieval of cytoplasmic diffusion laws. In this thesis, the STED-FCS method was applied first in single point measurements, to demonstrate its ability to calculate diffusion laws in the nuclear environment. Then, this super-resolution technique was added to the Intensity Sorted FCS method, showing the ability to retrieve diffusion laws associate to different nuclear compartments in the same measurement.

Overall, each technique shown in this work aims to get precise dynamic information in a highly heterogeneous system, such as the eukaryotic cell nucleus. In addition, both of these methods, especially if coupled with super-resolution, would be useful to study the dynamics of chromatin at the nanoscale, eventually leading to interesting insights into nuclear structure-function relationships.

List of publications

Di Bona M., Mancini M.A., Mazza D., Vicidomini G., Diaspro A., Lanzanò L., "Measuring mobility in chromatin by intensity sorted FCS", Biophysical Journal 2019, *in press*

Scipioni L., **Di Bona M.**, Vicidomini G., Diaspro A., Lanzanò L., "Local raster image correlation spectroscopy generates high-resolution intracellular diffusion maps", Communications Biology 2018; 1:10.

Lanzanò L., Scipioni L., **Di Bona M.**, Bianchini P., Bizzarri R., Cardarelli F., Diaspro A., Vicidomini G., "Measurement of nanoscale three-dimensional diffusion in the interior of living cells by STED-FCS", Nature Communications 2017; 8: 65.

Di Bona M., Pelicci S., Vicidomini G., Cammarota E., Mazza D., Diaspro A., Lanzanò L., "Probing Chromatin Organization by Sorting of Short Sequence Fluorescence Correlation Spectroscopy", Biophys J., Volume 114, Issue 3, Supplement 1, p563a, 2 February 2018

Di Bona M., Scipioni L., Sarmento M.J., Vicidomini G., Diaspro A., Lanzanò L., "Chromatin accessibility studied by slow scan FCS in the eukaryotic nucleus". Biophys J., Volume 112, Issue 3, Supplement 1, p216a, 3 February 2017

Bibliography

1. Jablonski, A. 1933. Efficiency of Anti-Stokes Fluorescence in Dyes. Nature. : 839–940.
2. Lichtman, J.W., and J.-A. Conchello. 2005. Fluorescence Microscopy. Nat. Methods. 2: 910–919.
3. Kubin, R.F., and A.N. Fletcher. 1982. Fluorescence Quantum Yields of Some Rhodamine Dyes. J. Lumin. 27: 455–462.
4. Strickler, S.J., and R.A. Berg. 1962. Relationship between absorption intensity and fluorescence lifetime of molecules. J. Chem. Phys. 37: 814–822.
5. Gadella, T.W.J., T.M. Jovin, and R.M. Clegg. 1993. Fluorescence lifetime imaging microscopy (FLIM): Spatial resolution of microstructures on the nanosecond time scale. Biophys. Chem. 48: 221–239.
6. Born, M., and E. Wolf. 1959. Principles of Optics. .
7. Zernike, F. 1942. Phase contrast, a new method for the microscopic observation of transparent objects. Phys. IX. : 686–698.
8. Chalfie, M., Y. Tu, G. Euskirchen, W.W. Ward, and D.C. Prasher. 1994. Green fluorescent protein as a marker for gene expression. Science (80-.). 263: 802–805.
9. Sheppard, C.J.R., and A. Choudhury. 1977. Image formation in the scanning microscope. Opt. Acta (Lond). 24: 1051–1073.
10. Minsky, M. 1961. Microscopy Apparatus. .
11. Abbe, E. 1873. Beitrage zur Theorie des Mikroskops und der mikroskopischen Wahrnehmung. Arch. für mikroskopische Anat. .
12. Reits, E.A.J., and J.J. Neefjes. 2001. From fixed to FRAP : measuring protein mobility and activity in living cells. Nat. Cell Biol. 3: 145–147.
13. Wüstner, D., L.M. Solanko, F.W. Lund, D. Sage, H.J. Schroll, and M.A. Lomholt. 2012. Quantitative fluorescence loss in photobleaching for analysis of protein transport and aggregation. BMC Bioinformatics. : 1–21.
14. Wachsmuth, M., T. Weidemann, G. Muller, U.W. Hoffmann-Rohrer, T.A. Knoch, W. Waldeck, and J. Langowski. 2003. Analyzing Intracellular Binding and Diffusion with Continuous Fluorescence Photobleaching. Biophys. J. 84: 3353–3363.
15. Schmidt, T., G.J. Schutz, W. Baumgartner, H.J. Gruber, and H. Schindler. 1996. Imaging of single molecule diffusion. Proc. Natl. Acad. Sci. 93: 2926–2929.
16. Lanzanò, L., and E. Gratton. 2014. Orbital Single Particle Tracking on a commercial confocal microscope using piezoelectric stage feedback. Methods Appl. Fluoresc. 2: 1–19.
17. Levi, V., Q. Ruan, and E. Gratton. 2005. 3-D Particle Tracking in a Two-Photon Microscope : Application to the Study of Molecular Dynamics in Cells. Biophys. J. 88: 2919–2928.

18. Annibale, P., A. Dvornikov, and E. Gratton. 2015. Electrically tunable lens speeds up 3D orbital tracking. Biomed. Opt. Express. 6: 2181–2190.

19. Magde, D., E. Elson, and W.W. Webb. 1972. Thermodynamic fluctuations in a reacting system measurement by fluorescence correlation spectroscopy. Phys. Rev. Lett. 29: 705–708.

20. Lanzano, L. 2018. Back to the Future : Fluorescence Correlation Spectroscopy Moves Back in the Cuvette. Biophys. J. : 427–428.

21. Koppel, D.E., D. Axelrod, J. Schlessinger, E.L. Elson, and W.W. Webb. 1976. Dynamics of Fluorescence Marker Concentration as a Probe of Mobility. Biophys. J. 16: 1315–1329.

22. Lakowicz, J.R. 2002. Topics in Fluorescence Spectroscopy. .

23. Saffarian, S., and E.L. Elson. 2003. Statistical analysis of fluorescence correlation spectroscopy: The standard deviation and bias. Biophys. J. 84: 2030–2042.

24. Wawrezinieck, L., H. Rigneault, D. Marguet, and P.-F. Lenne. 2005. Fluorescence Correlation Spectroscopy Diffusion Laws to Probe the Submicron Cell Membrane Organization. Biophys. J. 89: 4029–4042.

25. Humpolickova, J., E. Gielen, A. Benda, V. Fagulova, J. Vercammen, M. VandeVen, M. Hof, M. Ameloot, and Y. Engelborghs. 2006. Probing Diffusion Laws within Cellular Membranes by Z-Scan Fluorescence Correlation Spectroscopy. Biophys. J. : 23–25.

26. Denk, W., J.H. Strickler, and W.W. Webb. 1990. Two-Photon Laser Scanning Fluorescence Microscopy. Science (80-.). 248: 73–76.

27. Berland, K.M., P.T.C. So, and E. Gratton. 1995. Two-Photon Fluorescence Correlation Spectroscopy : Method and Application to the Intracellular Environment. Biophys. J. 68: 694–701.

28. Dertinger, T., V. Pacheco, I. Von Der Hocht, R. Hartmann, I. Gregor, and J. Enderlein. 2007. Two-Focus Fluorescence Correlation Spectroscopy : A New Tool for Accurate and Absolute Diffusion Measurements. ChemPhysChem. : 433–443.

29. Wiseman, P.W. 2015. Image Correlation Spectroscopy : Principles and Applications. Cold Spring Harb. Protoc. : 336–349.

30. Ohsugi, Y., K. Saito, M. Tamura, and M. Kinjo. 2006. Lateral Mobility of Membrane-Binding Proteins in Living Cells Measured by Total Internal Reflection Fluorescence Correlation Spectroscopy. Biophys. J. 91: 3456–3464.

31. Capoulade, J., M. Wachsmuth, L. Hufnagel, and M. Knop. 2011. Quantitative fluorescence imaging of protein diffusion and interaction in living cells. Nat. Biotechnol. 29: 835–839.

32. Petersen, N.O., P.L. Höddelius, P.W. Wiseman, O. Seger, and K.E. Magnusson. 1993. Quantitation of membrane receptor distributions by image correlation spectroscopy: concept and application. Biophys. J. 65: 1135–1146.

33. Digman, M.A., C.M. Brown, P. Sengupta, P.W. Wiseman, A.R. Horwitz, and E. Gratton. 2005. Measuring fast dynamics in solutions and cells with a laser scanning microscope. Biophys. J. 89: 1317–1327.

34. Scipioni, L., M. Di Bona, G. Vicidomini, A. Diaspro, and L. Lanzanò. 2018. Local raster

image correlation spectroscopy generates high-resolution intracellular diffusion maps. Commun. Biol. 1: 1–10.

35. Ries, J., S. Chiantia, and P. Schwille. 2009. Accurate Determination of Membrane Dynamics with Line-Scan FCS. Biophys. J. 96: 1999–2008.

36. Ruan, Q., M.A. Cheng, M. Levi, E. Gratton, and W.W. Mantulin. 2004. Spatial-temporal studies of membrane dynamics: Scanning fluorescence correlation spectroscopy (SFCS). Biophys. J. 87: 1260–1267.

37. Kis-Petikova, K., and E. Gratton. 2004. Distance Measurement by Circular Scanning of the Excitation Beam in the Two-Photon Microscope. Microsc. Res. Tech. 63: 34–49.

38. Horiike, T., K. Hamada, S. Kanaya, and T. Shinozawa. 2001. Origin of eukaryotic cell nuclei by symbiosis of Archaea in Bacteria is revealed by homology-hit analysis. Nat. Cell Biol. 3: 210–214.

39. Rowley, M.J., and V.G. Corces. 2018. Organizational principles of 3D genome architecture. Nat. Rev. Genet. 13: 1.

40. Kornberg, R.D., and Y. Lorch. 1999. Twenty-five years of the nucleosome, fundamental particle of the eukaryote chromosome. Cell. 98: 285–294.

41. Almassalha, L.M., A. Tiwari, P.T. Ruhoff, Y. Stypula-Cyrus, L. Cherkezyan, H. Matsuda, M.A. Dela Cruz, J.E. Chandler, C. White, C. Maneval, H. Subramanian, I. Szleifer, H.K. Roy, and V. Backman. 2017. The Global Relationship between Chromatin Physical Topology, Fractal Structure, and Gene Expression. Sci. Rep. 7: 41061.

42. Di Micco, R., G. Sulli, M. Dobreva, M. Liontos, O.A. Botrugno, G. Gargiulo, R. dal Zuffo, V. Matti, G. d'Ario, E. Montani, C. Mercurio, W.C. Hahn, V. Gorgoulis, S. Minucci, and F. d'Adda di Fagagna. 2011. Interplay between oncogene-induced DNA damage response and heterochromatin in senescence and cancer. Nat. Cell Biol. 13: 292–302.

43. Sulli, G., R. Di Micco, and F. d'Adda di Fagagna. 2012. Crosstalk between chromatin state and DNA damage response in cellular senescence and cancer. Nat. Rev. Cancer. 12: 709–720.

44. Kaiser, V.B., and C.A. Semple. 2017. When TADs go bad: chromatin structure and nuclear organisation in human disease. F1000Research. 6: 314.

45. Golkaram, M., S. Hellander, B. Drawert, and L.R. Petzold. 2016. Macromolecular Crowding Regulates the Gene Expression Profile by Limiting Diffusion. PLOS Comput. Biol. 12: e1005122.

46. Sawyer, I.A., J. Bartek, and M. Dundr. 2018. Phase separated microenvironments inside the cell nucleus are linked to disease and regulate epigenetic state, transcription and RNA processing. Semin. Cell Dev. Biol. : 1–10.

47. Misteli, T. 2009. Self-organization in the genome. Proc. Natl. Acad. Sci. U. S. A. 106: 6885–6886.

48. Strom, A.R., A. V. Emelyanov, M. Mir, D. V. Fyodorov, X. Darzacq, and G.H. Karpen. 2017. Phase separation drives heterochromatin domain formation. Nature. : 1–10.

49. Boija, A., I.A. Klein, B.R. Sabari, T.I. Lee, D.J. Taatjes, R.A. Young, A. Boija, I.A. Klein, B.R. Sabari, A. Dall'Agnese, E.L. Coffey, A. V Zamudio, C.H. Li, K. Shrinivas, J.C. Manteiga, N.M. Hannett, B.J. Abraham, L.K. Afeyan, Y.E. Guo, J.K. Rimel, C.B. Fant, J. Schuijers, T.I. Lee, D.J. Taatjes, and R.A. Young. 2018. Transcription Factors Activate Genes through the Phase-Separation Capacity of Their Activation. Cell. : 1–14.

50. Sabari, B.R., A. Dall'Agnese, A. Boija, I.A. Klein, E.L. Coffey, K. Shrinivas, B.J. Abraham, N.M. Hannett, A. V Zamudio, J.C. Manteiga, C.H. Li, Y.E. Guo, D.S. Day, J. Schuijers, E. Vasile, S. Malik, D. Hnisz, T.I. Lee, I.I. Cisse, R.G. Roeder, P.A. Sharp, A.K. Chakraborty, and R.A. Young. 2018. Coactivator condensation at super-enhancers links phase separation and gene control. Science (80-.). 3958: 1–17.

51. Nozaki, T., R. Imai, M. Tanbo, R. Nagashima, S. Tamura, T. Tani, Y. Joti, M. Tomita, K. Hibino, M.T. Kanemaki, K.S. Wendt, Y. Okada, T. Nagai, and K. Maeshima. 2017. Dynamic Organization of Chromatin Domains Revealed by Super-Resolution Live-Cell Imaging. Mol. Cell. : 1–12.

52. Phair, R.D., and T. Misteli. 2000. High mobility of proteins in the mammalian cell nucleus. Nature. 404: 604–609.

53. Misteli, T. 2001. Protein dynamics: Implications for nuclear architecture and gene expression. Science (80-.). 291: 843–847.

54. Cuvier, O., and B. Fierz. 2017. Dynamic chromatin technologies: from individual molecules to epigenomic regulation in cells. Nat. Rev. Genet. : 1–16.

55. Annibale, P., and E. Gratton. 2014. Advanced fluorescence microscopy methods for the real-time study of transcription and chromatin dynamics. Transcription. 5: e28425.

56. Germier, T., S. Kocanova, N. Walther, A. Bancaud, H.A. Shaban, H. Sellou, A.Z. Politi, J. Ellenberg, F. Gallardo, and K. Bystricky. 2017. Real-Time Imaging of a Single Gene Reveals Transcription-Initiated Local Confinement. Biophys. J. : 1383–1394.

57. Wachsmuth, M., T.A. Knoch, and K. Rippe. 2016. Dynamic properties of independent chromatin domains measured by correlation spectroscopy in living cells. Epigenetics Chromatin. : 1–20.

58. Hinde, E., F. Cardarelli, and E. Gratton. 2015. Spatiotemporal regulation of Heterochromatin Protein 1- alpha oligomerization and dynamics in live cells. Nat. Publ. Gr. : 1–11.

59. Muller, K.P., F. Erdel, M. Caudron-Herger, C. Marth, B.D. Fodor, M. Richter, M. Scaranaro, J. Beaudouin, M. Wachsmuth, and K. Rippe. 2009. Multiscale analysis of dynamics and interactions of heterochromatin protein 1 by fluorescence fluctuation microscopy. Biophys. J. 97: 2876–2885.

60. Erdel, F., K. Müller-Ott, M. Baum, M. Wachsmuth, and K. Rippe. 2011. Dissecting chromatin interactions in living cells from protein mobility maps. Chromosom. Res. 19: 99–115.

61. Tsutsumi, M., H. Muto, S. Myoba, M. Kimoto, A. Kitamura, M. Kamiya, T. Kikukawa, S. Takiya, M. Demura, K. Kawano, M. Kinjo, and T. Aizawa. 2015. In vivo fluorescence-correlation spectroscopy analyses of FMBP-1, a silkworm transcription factor. FEBS Open Bio. .

62. Michelman-Ribeiro, A., D. Mazza, T. Rosales, T.J. Stasevich, H. Boukari, V. Rishi, C. Vinson, J.R. Knutson, and J.G. McNally. 2009. Direct measurement of association and dissociation rates of DNA binding in live cells by fluorescence correlation spectroscopy. Biophys. J. 97: 337–346.

63. Papadopoulos, D.K., A.J. Krmpot, S.N. Nikolić, R. Krautz, L. Terenius, P. Tomancak, R. Rigler, W.J. Gehring, and V. Vukojević. 2015. Probing the kinetic landscape of Hox transcription factor-DNA binding in live cells by massively parallel Fluorescence Correlation Spectroscopy. Mech. Dev. 138: 218–225.

64. Singh, A.P., R. Galland, M.L. Finch-Edmondson, G. Grenci, J.-B. Sibarita, V. Studer, V. Viasnoff, and T.E. Saunders. 2017. 3D Protein Dynamics in the Cell Nucleus. Biophys. J. 112: 133–142.

65. Wachsmuth, M., W. Waldeck, and J. Langowski. 2000. Anomalous diffusion of fluorescent probes inside living cell nuclei investigated by spatially-resolved fluorescence correlation spectroscopy. J. Mol. Biol. 298: 677–689.

66. Dross, N., C. Spriet, M. Zwerger, G. Müller, W. Waldeck, and J. Langowski. 2009. Mapping eGFP Oligomer Mobility in Living Cell Nuclei. PLoS One. 4: e5041.

67. Park, H., S.S. Han, Y. Sako, and C.G. Pack. 2015. Dynamic and unique nucleolar microenvironment revealed by fluorescence correlation spectroscopy. FASEB J. 29: 837–848.

68. Hinde, E., F. Cardarelli, M. a Digman, and E. Gratton. 2010. In vivo pair correlation analysis of EGFP intranuclear diffusion reveals DNA-dependent molecular flow. Proc. Natl. Acad. Sci. U. S. A. 107: 16560–16565.

69. Bancaud, A., S. Huet, N. Daigle, J. Mozziconacci, J. Beaudouin, and J. Ellenberg. 2009. Molecular crowding affects diffusion and binding of nuclear proteins in heterochromatin and reveals the fractal organization of chromatin. EMBO J. 28: 3785–3798.

70. Baum, M., F. Erdel, M. Wachsmuth, and K. Rippe. 2014. Retrieving the intracellular topology from multi-scale protein mobility mapping in living cells. Nat. Commun. 5: 1–12.

71. Hansen, J.C., M. Connolly, C.J. Mcdonald, A. Pan, A. Pryamkova, K. Ray, E. Seidel, S. Tamura, R. Rogge, and K. Maeshima. 2017. The 10-nm chromatin fiber and its relationship to interphase chromosome organization. Biochem. Soc. Trans. 0: 1–10.

72. Maeshima, K., R. Rogge, S. Tamura, Y. Joti, T. Hikima, H. Szerlong, C. Krause, J. Herman, E. Seidel, T. Ishikawa, and J.C. Hansen. 2016. Nucleosomal arrays self-assemble into hierarchical globular structures lacking 30nm fibers. EMBO J. : 1–18.

73. Hendrix, J., T. Dekens, W. Schrimpf, and D.C. Lamb. 2016. Arbitrary-Region Raster Image Correlation Spectroscopy. Biophys. J. 111: 1785–1796.

74. Mascetti, G., L. Vergani, A. Diaspro, S. Carrara, G. Radicchi, and C. Nicolini. 1996. Effect of fixatives on calf thymocytes chromatin as analyzed by 3D high-resolution fluorescence microscopy. Cytometry. 23: 110–119.

75. Ranjit, S., L. Lanzano, and E. Gratton. 2014. Mapping diffusion in a living cell via the phasor approach. Biophys. J. 107: 2775–2785.

76. Ries, J., and P. Schwille. 2012. Fluorescence correlation spectroscopy. BioEssays. : 361–368.

77. Vicidomini, G., I. Coto Hernández, M. d'Amora, F. Cella Zanacchi, P. Bianchini, and A. Diaspro. 2014. Gated CW-STED microscopy: A versatile tool for biological nanometer scale investigation. Methods. 66: 124–130.

78. Stossi, F., M.J. Bolt, F.J. Ashcroft, J.E. Lamerdin, J.S. Melnick, R.T. Powell, R.D. Dandekar, M.G. Mancini, C.L. Walker, J.K. Westwick, and M.A. Mancini. 2014. Defining Estrogenic Mechanisms of Bisphenol A Analogs through High Throughput Microscopy-Based Contextual Assays. Chem. Biol. 21: 743–753.

79. Llères, D., J. James, S. Swift, D.G. Norman, and A.I. Lamond. 2009. Quantitative analysis of chromatin compaction in living cells using FLIM–FRET. J. Cell Biol. 187: 481–496.

80. Albiez, H., M. Cremer, C. Tiberi, L. Vecchio, L. Schermelleh, S. Dittrich, K. Kupper, B. Joffe, T. Thormeyer, J. von Hase, S. Yang, K. Rohr, H. Leonhardt, I. Solovei, C. Cremer, S. Fakan, and T. Cremer. 2006. Chromatin domains and the interchromatin compartment form structurally defined and functionally interacting nuclear networks. Chromosom. Res. : 707–733.

81. Kapusta, P., M. Wahl, A. Benda, M. Hof, and J. Enderlein. 2007. Fluorescence Lifetime Correlation Spectroscopy. J. Fluoresc. 17: 43–48.

82. Gröner, N., J. Capoulade, C. Cremer, and M. Wachsmuth. 2010. Measuring and imaging diffusion with multiple scan speed image correlation spectroscopy. Opt. Express. 18: 21225–21237.

83. Stenoien, D.L., K. Patel, M.G. Mancini, M. Dutertre, C.L. Smith, B.W. O' Malley, and M.A. Mancini. 2001. FRAP reveals that mobility of oestrogen receptor- α is ligand- and proteasome-dependent. Nat. Cell Biol. 3: 15–23.

84. Lanzano, L., T. Lei, K. Okamura, H. Giral, Y. Caldas, O. Masihzadeh, E. Gratton, M. Levi, and J. Blaine. 2011. Differential modulation of the molecular dynamics of the type IIa and IIc sodium phosphate cotransporters by parathyroid hormone. Am. J. Cell Physiol. : 850–861.

85. Cardarelli, F., L. Lanzano, and E. Gratton. 2012. Capturing directed molecular motion in the nuclear pore complex of live cells. Proc. Natl. Acad. Sci. 109: 9863–9868.

86. Annibale, P., and E. Gratton. 2015. Single cell visualization of transcription kinetics variance of highly mobile identical genes using 3D nanoimaging. Sci. Rep. : 1–9.

87. Sharp, Z.D., M.G. Mancini, C.A. Hinojos, F. Dai, V. Berno, A.T. Szafran, K.P. Smith, T.P. Lele, D.E. Ingber, M.A. Mancini, Z.D. Sharp, M.G. Mancini, C.A. Hinojos, F. Dai, V. Berno, A.T. Szafran, K.P. Smith, T.T. Lele, D.E. Ingber, and M.A. Mancini. 2006. Estrogen-receptor- alfa exchange and chromatin dynamics are ligand- and domain-dependent. J. Cell Sci. 4365: 4101–4116.

88. Lord Rayleigh, J.W. 1879. XXXI. Investigations in optics, with special reference to the spectroscope. Philos. Mag. J. Sci. 8: 261–274.

89. Cremer, C., A. Szczurek, F. Schock, A. Gourram, and U. Birk. 2017. Super-resolution microscopy approaches to nuclear nanostructure imaging. Methods. 123: 11–32.

90. Hell, S.W., and J. Wichman. 1994. Breaking the diffraction resolution limit by stimulated

emission: stimulated-emission-depletion fluorescence microscopy. Opt. Lett. 19: 780–782.

91. Vicidomini, G., P. Bianchini, and A. Diaspro. 2018. STED super-resolved microscopy. Nat. Methods. 8: 1–10.

92. Vicidomini, G., A. Schönle, H. Ta, K.Y. Han, G. Moneron, C. Eggeling, and S.W. Hell. 2013. STED Nanoscopy with Time-Gated Detection: Theoretical and Experimental Aspects. PLoS One. 8: e54421.

93. Vicidomini, G., G. Moneron, K.Y. Han, V. Westphal, H. Ta, M. Reuss, J. Engelhardt, C. Eggeling, and S.W. Hell. 2011. Sharper low-power STED nanoscopy by time gating. Nat. Methods. 8: 571–573.

94. Lanzanò, L., I. Coto Hernández, M. Castello, E. Gratton, A. Diaspro, and G. Vicidomini. 2015. Encoding and decoding spatio-temporal information for super-resolution microscopy. Nat. Commun. 6.

95. Bianchini, P., F. Cardarelli, M. Di Luca, A. Diaspro, and R. Bizzarri. 2014. Nanoscale protein diffusion by STED-based pair correlation analysis. PLoS One. 9: e99619.

96. Eggeling, C., C. Ringemann, R. Medda, G. Schwarzmann, K. Sandhoff, S. Polyakova, V.N. Belov, B. Hein, C. Von Middendorff, A. Schonle, and S.W. Hell. 2009. Direct observation of the nanoscale dynamics of membrane lipids in a living cell. Nature. 457: 1159–1163.

97. Clausen, M.P., E. Sezgin, J. Bernardino de la Serna, D. Waithe, B.C. Lagerholm, and C. Eggeling. 2015. A straightforward approach for gated STED-FCS to investigate lipid membrane dynamics. Methods. 88: 67–75.

98. Lanzanò, L., L. Scipioni, M. Di Bona, P. Bianchini, F. Cardarelli, A. Diaspro, and G. Vicidomini. 2017. Measurement of nanoscale three-dimensional diffusion in the interior of living cells by STED-FCS. Nat. Commun. : 1–9.